**Ph. D. Dissertation**
博士論文

# Glacial meltwater distribution and its variability in the northwestern Greenlandic fjord

（グリーンランド北西フィヨルドにおける
氷河流出水の分布とその変動特性）

**Graduate School of Environmental Science**
**Hokkaido University**
北海道大学大学院環境科学院

**Yoshihiko Ohashi**
大橋　良彦

**February 2018**

## Contents

## Abstract

## Abstract

In recent years, glacial meltwater discharge from Greenland into the surrounding ocean has increased, affecting recent rapid ice mass loss. Meltwater discharge significantly affects fjord water circulation, material transport and biological productivity. Despite its importance in the understanding of impact of glacial meltwater on the fjord environment, the three dimensional distribution of turbid glacial meltwater and its variability are incompletely understood. This study focuses on the northwestern part of Greenland that ice mass loss is increasing and aims to investigate the horizontal and vertical distributions of turbid glacial meltwater in the fjord and the controlling factor of their variability, based on remote sensing data analyses, in-situ observations and numerical model experiments.

First, to quantify the spatial and temporal variations in high turbidity surface water off the Thule region, we analyzed the remote sensing reflectance data at a wavelength of 555 nm. The high turbidity area, identified on the basis of high reflectivity ($Rrs555 \geq 0.0070\ sr^{-1}$), was generally distributed near the coast, where many outlet glaciers terminate in the ocean and on land. The extent of the high turbidity area exhibited substantial seasonal and interannual variability, and its annual maximum extent was significantly correlated with summer air temperature. Thus, the source of the turbid water observed is most likely the discharge of glacial meltwater. This relationship between the turbidity area and discharge is likely applicable to not only off the Thule region but also the other regions that consist of the relatively large shelf area and glaciers located near the open ocean/fjord off the western Greenland coast.

Second, to better understand the vertical distribution of glacial meltwater, we focuses on the behavior of subglacial meltwater in the Bowdoin Fjord and aims to reveal

controlling factors of its interannual variability. The fraction of subglacial meltwater in fjord water was analyzed by using observed temperature and salinity, and numerical model experiments were performed to investigate the oceanic influence on freshwater behavior. The most turbid water was found at the subsurface layer (15–40 m). The maximum subglacial meltwater fractions in this layer near the ice front were estimated to be ~6.0% in 2014 and ~4.0% in 2016, respectively. Numerical model experiment with changing initial stratifications suggests that the difference in the subglacial meltwater fraction at this layer is due to the stratification difference. Near the surface (5–15 m), turbidity was higher in 2016, consistent with the stronger influence of turbid subglacial meltwater. This difference near the surface can be primarily attributed to around 20% increase in the subglacial discharge based on the numerical modeling forced by changing amount of discharge. This study on Bowdoin Fjord indicates that the interannual difference in ambient fjord stratification can control the subglacial meltwater distribution, together with the difference in buoyancy forcing associated with the amount of subglacial discharge.

Third, to understand the broader behavior of turbid glacial meltwater and link the Bowdoin Fjord with a broader fjord system, we conducted satellite data analyses and numerical model experiments in the whole Inglefield Bredning in 2016 as the case study. In the Inglefield Bredning fjord system, high turbidity area increased from mid-July to the end of July (2140 $km^2$) and then decreased until mid-August (260 $km^2$). The maximum extent of high turbidity area at the end of July occurred about 10 days later after the timing of the highest air temperature. This time lag suggests that the whole sequence of processes, from ice surface melt and subglacial meltwater discharge to spreading of turbid subglacial meltwater over the fjord surface, takes about 10 days. The observed high turbidity water

can reflect the anticlockwise drift patterns of turbid glacial meltwater, possibly overlaid by the pattern that meltwater discharges from the glacier that located nearer the mouth of Inglefield Bredning blocked the northward spread of subglacial meltwater from the other glaciers.

Based on the relationship between the distribution of turbid glacial meltwater and the amount of meltwater discharge, turbid glacial meltwater spreads broader at the surface with higher concentration under the influence of increasing turbid glacial meltwater discharge, as can be inferred from present and predicted future warming trends. This study quantified the variability in turbid glacial meltwater distribution in the northwestern Greenlandic fjord, which is influenced by the amount of glacial meltwater and the strength of fjord stratification. Results of this study can contribute to the understanding of impacts of the increase in meltwater discharge from Greenland ice sheet to ocean that is the current important issue.

# Chapter 1

# Introduction

## 1.1. Ice mass loss and freshwater discharge from the Greenland ice sheet

In recent years, ice mass loss from the Greenland ice sheet is accelerating. The rate of mass loss increased from 51 ± 65 Gt $a^{-1}$ in 1992–2000 to 211 ± 37 Gt $a^{-1}$ in 2000–2011 (Shepherd et al., 2012). The acceleration of ice mass loss occurs mainly due to increases in meltwater discharge and ice discharge from marine-terminating outlet glaciers (e.g., Sasgen et al., 2012; Andersen et al., 2015). Meltwater discharge is caused by the surface melting of ice. On the other hand, ice discharge from marine-terminating outlet glaciers consists of breakaway of iceberg (calving) and submarine melting of the glacier front. In particular, meltwater discharge has increased in response to warming air temperature in recent years (Bamber et al., 2012; Schrama et al., 2014; Hanna et al., 2008; Fettweis et al., 2013a; Fettweis et al., 2013b). From the recent estimate, meltwater discharge accounts for 84% of the increase in ice mass loss after 2009 (Enderlin et al., 2014). Despite its importance in the understanding of ice mass loss, meltwater discharge was estimated with climate models and thus difficult to validate (Smith et al., 2017), and its amount remain highly uncertain.

These changes in ice mass are non-uniformly distributed over Greenland. Rapid mass loss has been observed particularly in the coastal regions where many outlet glaciers are located (Pritchard et al., 2009; Khan et al., 2015). Furthermore, change in ice mass loss is spatially heterogeneous (e.g., Sasgen et al., 2012; Enderlin et al., 2014). In recent years, ice mass loss is increasing in the northwestern part of Greenland (Khan et al., 2010; Kjær

et al., 2012) (Fig. 1.1). Therefore, the fjords surrounding northwestern Greenland can be strongly impacted by glacial melting and monitoring the impact of glacial meltwater on fjord environment has become increasingly important.

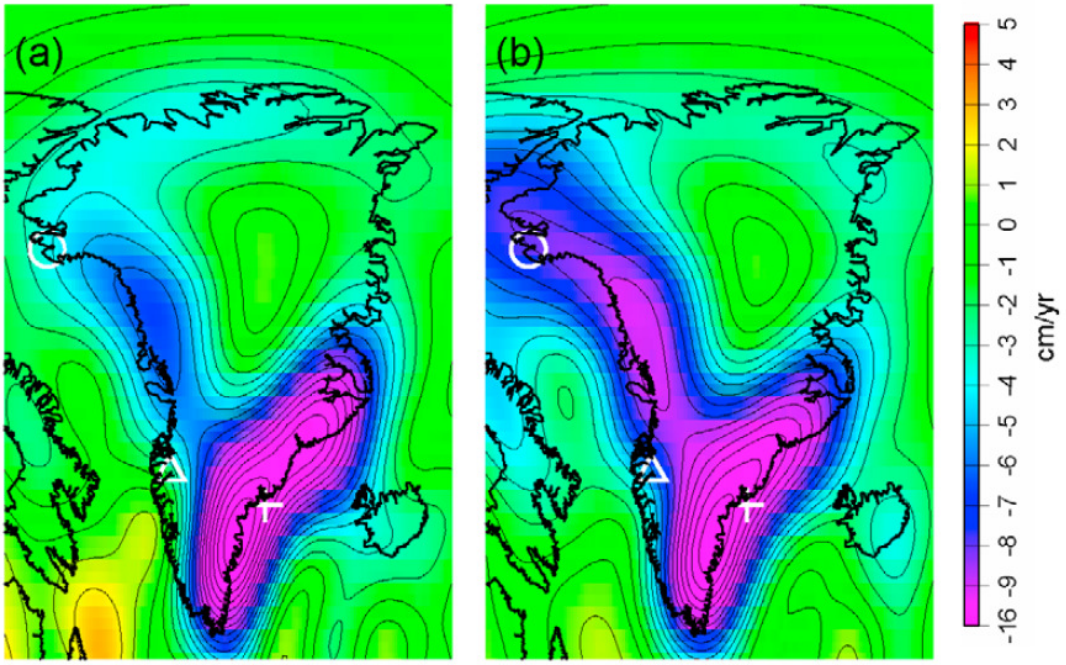


Fig. 1.1. The rate of mass loss of Greenland ice sheet, in cm/yr water equivalent thickness, determined from monthly GRACE gravity field solutions (Khan et al., 2010). The rate averaged between (a) February 2003 and February 2007, and (b) February 2003 and June 2009.

## 1.2. Impacts of meltwater discharge on the fjord environment

Meltwater discharge significantly affects fjord water circulation, material transport and biological productivity (e.g., Chu, 2014; Carroll et al., 2015; Lydersen et al., 2014; Carroll et al., 2017). In the land-terminating glaciers, meltwater transports sediments through proglacial rivers and spreads as high turbidity water area at the ocean surface

(Chu et al., 2012; Hopwood et al., 2015). On the other hand, in the ocean-terminating glaciers, meltwater produced on the ice surface drains through a crevasse to the base of a glacier. The submerged meltwater entrains sediments from a subglacial drainage system before it discharges into the fjord. The turbid subglacial meltwater gains buoyancy and forms an upwelling plume with entraining the ambient fjord water (Jenkins, 1999; 2011, Sciascia et al., 2013; Xu et al., 2013).

After upwelling, a substantial fraction of subglacial meltwater plume submerges and extends offshore at the lower part of the low density Surface Water (SW; Mortensen et al., 2011; Chauché et al., 2014; see section 1.5) layer (Xu et al., 2013; Chauché et al., 2014). Because the plume transports sediment from the land and deep layer of fjord (Chu, 2014), a turbid water layer is observed at the subsurface where the plume spreads (Chauché et al., 2014; Stevens et al., 2016). Because the ambient ocean water delivered by the plume contain macro and micro nutrients, subglacial plume formation can have a potential impact on marine biological productivity (Arendt et al., 2011; Lydersen et al., 2014; Meire et al., 2017). On the other hand, high concentrations of suspended sediment near the fjord surface might reduce light availability (Retamal et al., 2008). It is thus important to capture the realistic behavior of glacial meltwater and associated water properties. However, only a few studies have been reported on interannual variabilities in the distributions of glacial meltwater and the variables such as suspended sediment in the Greenlandic glacial fjords.

## 1.3. Detection of turbid surface water based on satellite remote sensing

The distribution of glacial meltwater can be visualized by turbidity because meltwater transports sediments from land and spreads as high turbidity water adjacent to the ice

sheet (e.g., Hopwood et al., 2015) (Fig. 1.2). Therefore, turbidity measurements in the proglacial fjord can help to assess the impact of glacial meltwater. Previous studies have used MODIS visible satellite images to measure spatial variations in sediment concentrations and the extent of high turbidity water, in particular in Kangerlussuaq Fjord off southwestern Greenland (Chu et al., 2009; McGrath et al., 2010). Kangerlussuaq Fjord is located at the margin of a narrow, confined proglacial river and its environment is therefore significantly different from that of the coastal ocean. However, there is little quantitative information regarding the extent and variability of high turbidity water in open coastal ocean off the Greenland ice sheet.

In mid-latitude open coastal regions, where oceans are affected by river runoff, normalized water-leaving radiance at a wavelength of 555 nm (nLw555 : mW $cm^{-2}$ $\mu m^{-1}$ $sr^{-1}$) is commonly used to analyze the distribution of turbid water (e.g., Caballero et al., 2011, 2014; Saldías et al., 2012). Caballero et al. (2014) showed that the development of turbid plumes off southwestern Spain was influenced by discharges from the Guadalquivir river and by precipitation. Saldías et al. (2012) revealed that turbid plumes with an extent > 1000 $km^2$ occur off central Chile following large-scale river runoff events associated with strong southward winds. However, this method has not been applied to the proglacial ocean off Greenland thus far.

From the above, an understanding of the extent of high turbidity surface area and its variability based on the remote sensing data analyses is thus important to assess the distribution of glacial meltwater. Although remote sensing data analyses are suitable for understanding the horizontal distribution at the ocean surface in the broader area, this method cannot capture the vertical distributed structure. Because the marine-terminating glacier discharges subglacial meltwater into the ocean at several hundred meters below

sea level, turbid subglacial meltwater plume doesn't necessarily reach the fjord surface (Fig. 1.3). Therefore, to understand the whole picture of the three dimensional distribution of glacial meltwater, we need to investigate not only the horizontal distribution of glacial meltwater at the surface but also the vertical distribution.


Fig. 1.2. MODIS true color image of the Greenland coastline taken on 12 August 2012 (Nuuk; Hopwood et al., 2015).

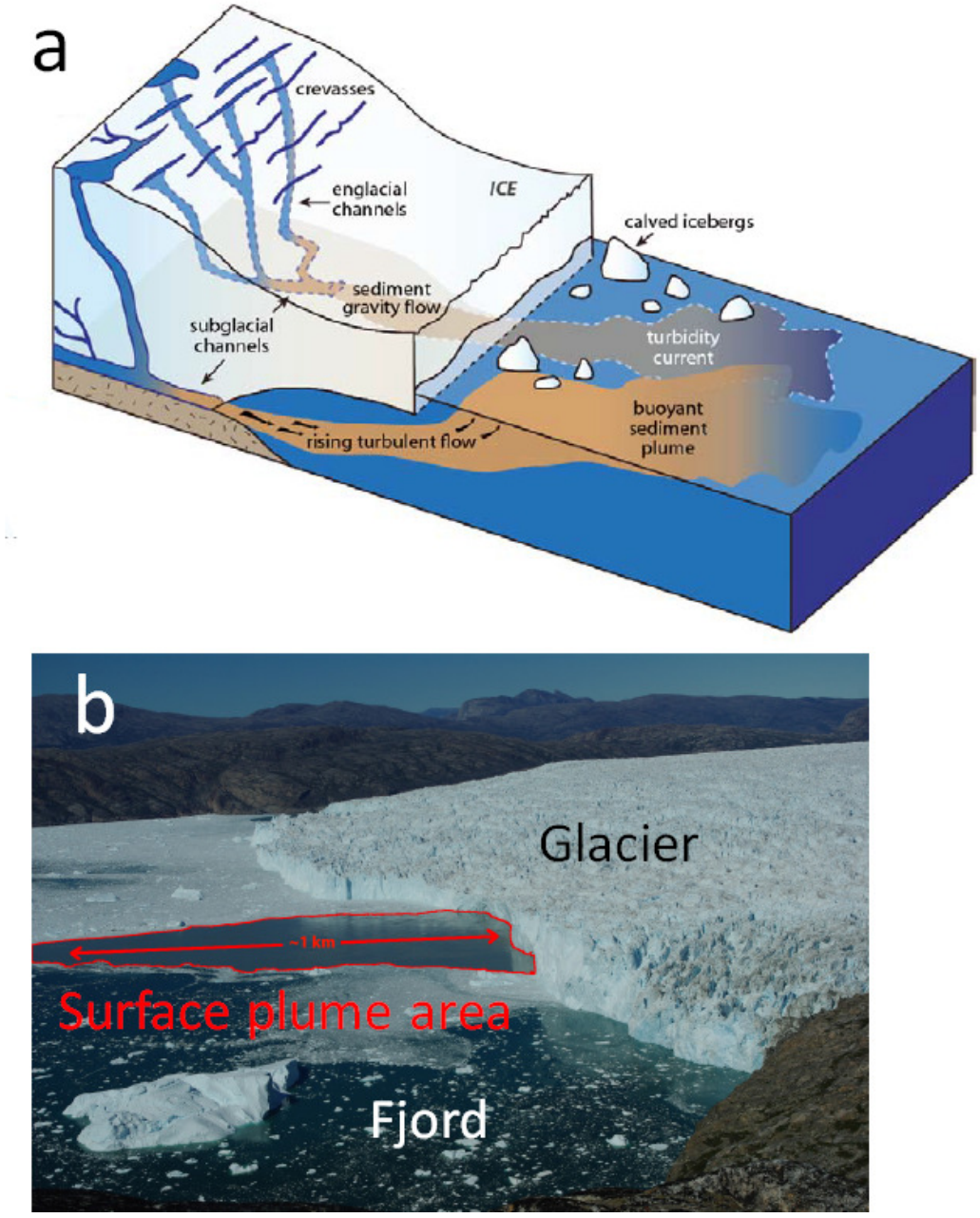


Fig. 1.3. (a) Schematic diagram of turbid glacial meltwater discharge from glacier to the ocean in marine-terminating glacier (Chu, 2014; modified from Cuffey and Paterson, 2009). (b) Photo on marine-terminating glacier in 2012 (Store Glacier in western Greenland; Chauché et al., 2014). The red line shows the boundary of the turbid surface plume.

## 1.4. Understanding of subglacial meltwater distribution based on the in-situ observations

The vertical distribution of subglacial meltwater has been estimated by using the observed temperature and salinity. Subglacial meltwater discharge mixes with the ambient ocean water to form upwelling plume driven by its buoyancy. Assuming the conservation of heat and salt, mixed two different water masses are characterized by the straight line connecting the two points on the potential temperature–salinity ($\theta$–$S$) diagram. Thus, due to the mixing caused by subglacial meltwater discharge, $\theta$–$S$ properties align along the line connecting the subglacial meltwater and ambient ocean water (Runoff-slope; e.g., Mortensen et al., 2013; Straneo et al., 2011, 2012; see section 3.2.3). This analysis by using the $\theta$–$S$ diagram estimated the behavior of subglacial meltwater that it spreads offshore at the subsurface of fjord (e.g., Chauché et al., 2014; Stevens et al., 2016). Furthermore, in recent years, observations in front of Greenlandic glaciers revealed that plume surface waters consist of ~7–10% subglacial meltwater and ~90% entrained fjord waters (Bendtsen et al., 2015; Mankoff et al., 2016). To summarize, the vertical distribution of subglacial meltwater that transports significant amount of ambient ocean water to the fjord surface and then spreads offshore at the subsurface has been estimated from observed temperature and salinity.

## 1.5. Water mass properties in Greenlandic fjords

Ambient water mass properties regulate and reflect the distribution of glacial meltwater. In recent years, in-situ observations have been carried out to investigate the water mass structure in proglacial fjord. Water mass properties in the deep layer reflect

those of surrounding outer ocean. In the Greenlandic fjord, warm-salty water of Atlantic origin (Atlantic Water: AW; e.g., Straneo et al., 2012; Chauché et al., 2014) occupies the deepest part of fjord (Figs 1.4 and 1.5). Cold and relatively fresh water of Arctic origin (Polar Water: PW; e.g., Myers et al., 2007; Sutherland and Pickart, 2008; Ribergaard, 2007; Chauché et al., 2014) carried by the East and West Greenland Currents overlies the AW layer. The properties of the AW and PW vary around Greenland depending on the distance from their source regions (Straneo et al. 2012). Thus, ambient water properties are highly dependent on the relative influence between warm AW and cold PW. Furthermore, in the proglacial fjord, sea water is influenced by freshwaters from subglacial meltwater discharge (subglacial meltwater) and from submarine ice front melting (submarine meltwater). As shown in sections 1.2 and 1.4, subglacial meltwater discharge mixes with the ambient water to form upwelling plume due to its buoyancy. On the other hand, ocean heat can induce the melt of submerged part of glacier ice, resulting in submarine meltwater (e.g., Straneo and Heimbach, 2013). However, the actual impact of interannual variability in ambient ocean water properties, whose core properties can also vary temporarily depending on the subglacial meltwater distribution are still poorly understood. In addition, near the surface of proglacial fjord, significantly warm, fresh and hence low density SW is occupied by, whose property is strongly affected by solar insolation, iceberg and sea ice melts as well as the subglacial discharge.

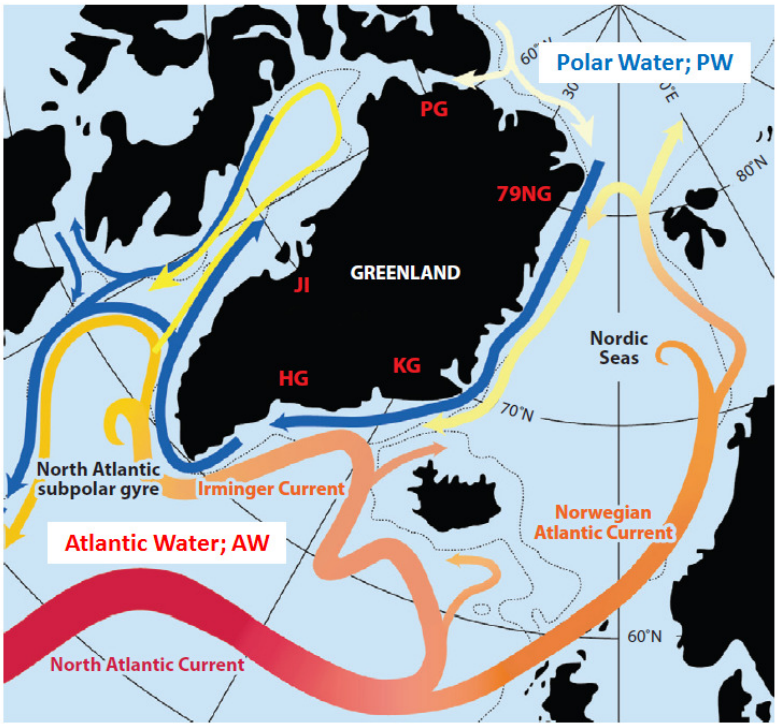


Fig. 1.4. Schematic circulation of warm salty Atlantic Water (AW) and cold fresh Polar Water (PW) (modified from Straneo and Cenedesse, 2015).

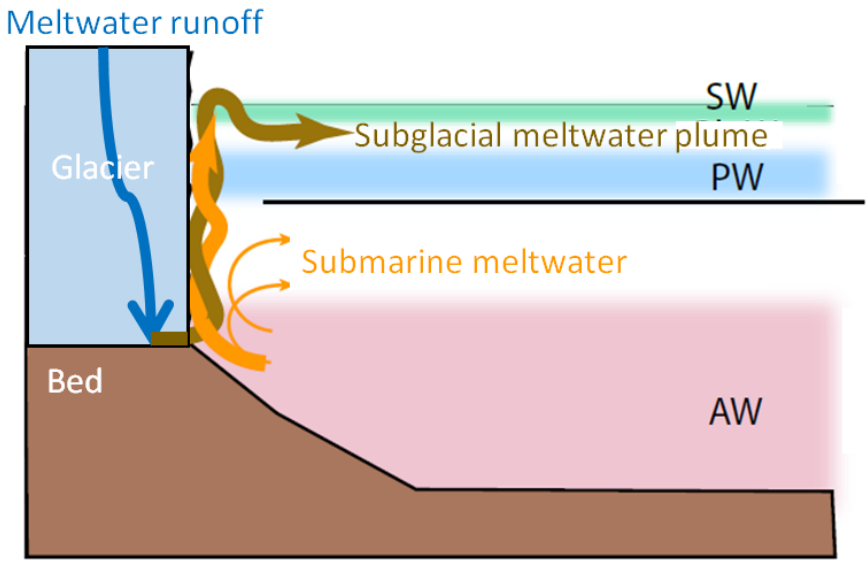


Fig. 1.5. Schematic diagram of water mass structure in the proglacial Greenlandic fjord with marine-terminating glacier (modified from Chauché et al., 2014). Surface and Polar, Atlantic Waters are indicated as SW, PW and AW, respectively.

## 1.6. Understanding of impacts on subglacial meltwater distribution based on the numerical model experiments

Changes in glacial and fjord conditions (the amount of subglacial discharge and the fjord stratification) can affect subglacial meltwater distribution. However, the amount of subglacial discharge is not observable and estimates of subglacial discharge are not well constrained and depend on unknown parameters such as ablation rate and catchment surface area (Chu, 2014). Recent advent of numerical experiment has made it feasible to replicate a realistic behavior of highly turbulent and nonlinear process of glacial discharge (e.g., Carroll et al., 2015). Therefore, sensitivity experiments of subglacial meltwater plume have been carried out by changing subglacial meltwater discharge and oceanic stratification to assess the impacts of these differences on subglacial meltwater distribution. Previous model study showed that subglacial meltwater extended at relatively shallower depth during a large amount of discharge (e.g., Xu et al., 2013; Carroll et al., 2015). Furthermore, strong stratification in the fjord prohibits upwelling of subglacial meltwater plume (Carroll et al., 2015). However, the factor controlling the observed subglacial meltwater distribution are still poorly understood. To understand the controlling factor, it is essential to combine in-situ observations and the realistic numerical model experiments.

## 1.7. Objectives of this study

This study aims to reveal the three dimensional distribution of turbid glacial meltwater and its variability in the northwestern Greenlandic fjords. The details are as follows;

1. (In Chapter 2) To quantify the extent and variability of high turbidity surface water in open coastal ocean off the Thule region, we analyzed variations in the spatial extent of high turbidity water and investigated the variation mechanisms based on remote sensing data. Furthermore, to understand the characteristics in spatio-temporal variabilities of the extent of high turbidity surface area, we also focused on the broader open fjords/ocean off the western Greenland coast.

2. (In Chapter 3) To understand the vertical distribution of subglacial meltwater, we conducted in-situ observations of fjord water properties in Bowdoin Fjord and analyzed the fraction of subglacial meltwater in fjord water. Furthermore, numerical fjord model experiments are carried out with non-hydrostatic settings, which is able to reproduce the distribution of subglacial meltwater into the fjord after discharge. The numerical experiments are conducted by changing freshwater discharge and oceanic stratification to assess the impacts of these differences on subglacial meltwater distribution. In the last analysis, we compare the observed results with the numerical model results to distinguish the mechanism controlling the interannual difference in the fjord water properties.

3. (In Chapter 4) To understand the broader behavior of turbid glacial meltwater, we analyzed the satellite datasets and performed a numerical model experiment of subglacial meltwater for a larger-scale domain. Targeting at the whole Inglefield Bredning fjord system off the Thule region, we investigated the temporal development of turbid glacial meltwater in 2016.

# Chapter 2

# Spatial and temporal variations in high turbidity surface water off the northwestern Greenland

## 2.1. Study area off the Thule region

This study focuses on an area consisting of relatively open fjords/ocean off the Thule region in northwestern Greenland (76–78°N, 65–75°W) (Fig. 2.1). Several studies of glacier dynamics around Inglefield Bredning (IB), in the northern area of Steensby Land, have recently been conducted (Dawes and van As, 2010; Porter et al., 2014; Sugiyama et al., 2015). IB is a 10–15 km wide and 100 km long fjord with maximum depth > 900 m (Fig. 2.1b). Seven outlet glaciers (about 1–7 km wide) terminate in this fjord from the northern flank of IB. Heilprin and Tracy Glaciers are the largest marine-terminating glaciers in the region (about 5–7 km wide), discharging into the eastern margin of the fjord at rates > 1000 m $a^{-1}$ (Porter et al., 2014). Bowdoin Glacier (BG) flows into Bowdoin Fjord (BF), a part of the IB fjord system, at a rate of ~500 m $a^{-1}$ (Sugiyama et al., 2015). Four outlet glaciers (about 2–7 km wide) discharge into Wolstenholme Fjord, in the southern area of Steensby Land, but relatively little is known about the dynamics of these glaciers. Moreover, a number of land-terminating glaciers and ice caps are located near the coastline of the fjord systems. Meltwater and sediment discharge from these glaciers and ice caps is affecting fjords/ocean in the study area. Furthermore, between autumn and spring, sea ice covers nearly the entire ocean surface in this region; however, in summer, a large portion of sea ice melts and open ocean appears (see section 2.2.3). The ocean environment in this area is thus significantly affected by glacial meltwater discharge in summer, when both continental ice and sea ice melt.

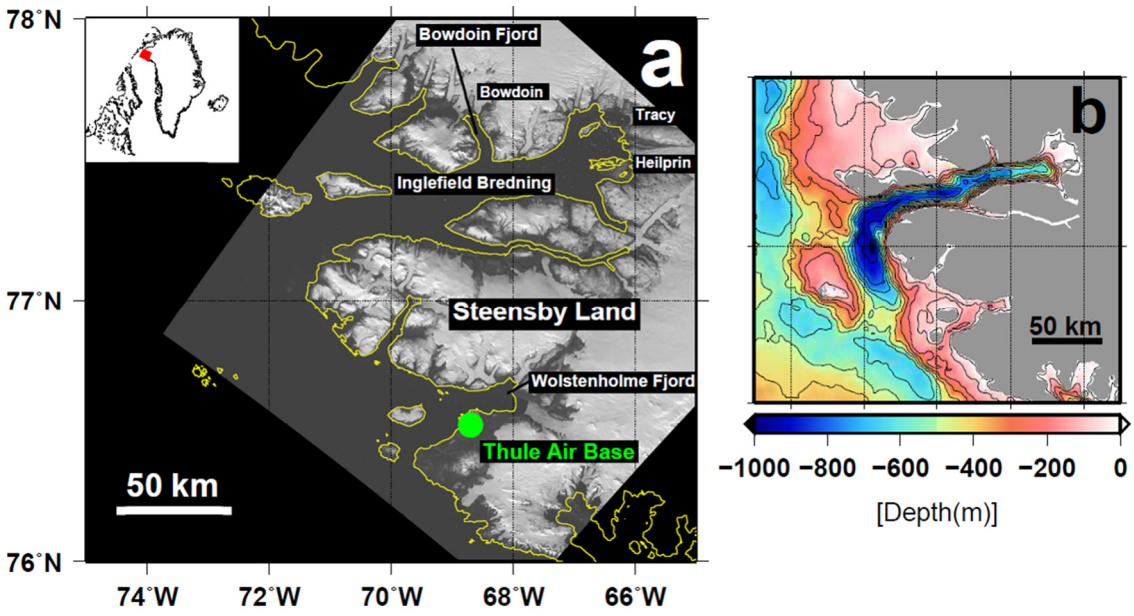


Fig. 2.1. (a) Landsat image taken on 6 September 2014, showing the study area. The location of Thule Air Base and the coastline are indicated by the green dot and yellow line, respectively. The inset shows the location of the study area in Greenland; (b) Ocean bathymetry in the study area (ETOPO1 developed by NOAA NGDC); contour intervals are 100 m.

## 2.2. Data and methods

### 2.2.1. Satellite data of surface turbidity

Satellite remote sensing of seawater optical properties is the most efficient technique to detect high turbidity water over a broad area. As described below, turbidity of near-surface water is well represented by remote sensing reflectance at a wavelength of 555 nm (Rrs555 : $sr^{-1}$). Rrs555 data used for this study were obtained from the NASA Moderate Resolution Imaging Spectroradiometer (MODIS) on the Aqua multispectral platform. We used the level three data with a spatial resolution of about 0.0417° and temporal resolution of eight days. The period of analysis was from July to August (the

period corresponding to open water in summer; see section 2.2.3) during 2002–2014. These data products were downloaded from NASA's Ocean Color Web (http://oceancolor.gsfc.nasa.gov).

### 2.2.2. Detection of high turbidity water

Coastal ocean waters with high sediment concentrations have a spectral peak in remote sensing reflectance at wavelengths of 550–600 nm (IOCCG, 2000). Caballero et al. (2011, 2014) measured the extent of high turbidity water in a marine region that was influenced by the Guadalquivir estuary using the following relationship;

$$\mathrm{nLw555} = F_0 \times \mathrm{Rrs555} \quad (\mathrm{mW\ cm^{-2}\ \mu m^{-1}\ sr^{-1}}) \qquad (2.1),$$

where $F_0$ is annual spectral mean extraterrestrial solar irradiance. In the 545–565 nm band on Aqua, the $F_0$ value corresponds to 186.09 mW $\mathrm{cm^{-2}}$ $\mu\mathrm{m^{-1}}$ (Neckel and Labs, 1984). The value of nLw555 defined by Equation 2.1 correlates better with the concentration of suspended sediments in near-surface waters than other wavelengths and has been frequently used as tracer to detect high turbidity river plume (Lahet and Stramski, 2010; Nezlin and DiGiacomo, 2005; Nezlin et al., 2005, 2008; Otero and Siegel, 2004; Thomas and Weatherbee, 2006; Valente and da Silva, 2009). Previous studies adopted nLw555 = 1.3 mW $\mathrm{cm^{-2}}$ $\mu\mathrm{m^{-1}}$ $\mathrm{sr^{-1}}$ as a threshold to detect a high turbidity plume boundary (Caballero et al., 2011, 2014; Nezlin and DiGiacomo, 2005; Nezlin et al., 2005; Otero and Siegel, 2004; Valente and da Silva, 2009). We thus identified the ocean area covered with high

turbidity water (high turbidity area) based on the condition of Rrs555 ≥ 0.0070 $sr^{-1}$, as per the previously-used criterion of nLw555 and Equation 2.1.

As an example of detected high turbidity water, Fig. 2.2 shows a MODIS true color image taken on 16 July 2012, with magnitude of Rrs555, and with a high turbidity area defined by the Rrs555 criterion. In the true color image, high turbidity water is visible at the mouths of several fjords off the ice sheet (Fig. 2.2a). These areas correspond to the extent of high turbidity water represented by Rrs555 (Fig. 2.2b), and this criterion delineates the central part of high turbidity water (Fig. 2.2c). This example confirms the ability of this technique to quantify the spatial extent of high turbidity water under the influence of glacial discharge, similar to the case of mid-latitude coastal areas affected by turbid river plumes. Using this method, the extent of the high turbidity area ($A$: $km^2$) was calculated from the number and area of image pixels (4.5–5.2 $km^2$);

$$A = \sum_{i=1}^{N_{\mathrm{Rrs555} \geq 0.0070\ \mathrm{sr}^{-1}}} A_i \quad (\mathrm{km}^2) \qquad (2.2),$$

where $N_{\mathrm{Rrs555} \geq 0.0070\ \mathrm{sr}^{-1}}$ is the number of pixels with Rrs555 values above the threshold and $A_i$ is the area of the image pixel. The Rrs555 dataset loses ~25% of information due to the presence of ice and cloud cover. Major icebergs are eliminated by the ice mask, which uses the Rayleigh-corrected near-infrared (NIR) reflectance threshold of 0.027 at the wavelength of 869 nm for MODIS (Patt et al., 2003; Wang and Shi, 2009). We replaced the Rrs555 value with 0 $sr^{-1}$ in the sea ice region (sea ice concentration of more than 15%; see section 2.2.3). For regions for which no data were available, where sea ice concentration was less than 15%, we assumed that there was cloud cover and Rrs555 was interpolated linearly from values before and after eight days.

### 2.2.3. Sea ice concentration, air temperature, and wind data

Glacial discharge and the extent of the high turbidity area are influenced by atmospheric and sea ice conditions. We thus analyzed sea ice concentrations, air temperature, and wind stress intensity to examine the basic environment in the study area and the mechanisms driving spatial and temporal variations in the extent of turbid water.

In this study, sea ice information was essential to define the extent and period of open water. The presence of sea ice leads to loss of the value of Rrs555. Sea ice concentration data were derived from the Advanced Microwave Scanning Radiometer for EOS (AMSR-E) on the Aqua multispectral platform and from the Advanced Microwave Scanning Radiometer2 (AMSR-2) on the Global Change Observation Mission-Water1 (GCOM-W1) satellite. We used a dataset developed by the universities of Hamburg and Bremen, with spatial and temporal resolutions of 6.25 km and 1 day (Spreen et al., 2008), respectively. We obtained the data from the website of the Integrated Climate Data Center, University of Hamburg (ftp://ftp.icdc.zmaw.de/asi_amsre_iceconc/) and from the Institute of Environmental Physics, University of Bremen (http://www.iup.uni-bremen.de:8084/amsr2data/asi_daygrid_swath/n6250/), Germany. The dataset for 2002–2014 showed that sea ice rapidly decreased from mid-June and reached its annual minimum between early July and mid-October. The selected period for our analysis was thus the summer months of July and August, corresponding to the period of sea ice retreat.

Air temperature affects melt on glacial surfaces. We used air temperature records from the Pituffik/Thule Air Base, located in the south of the study area (76°32′ N, 68°42′ W, 76.5 m a.s.l.) (Fig. 2.1a). Three-hourly air temperature data are distributed by the US National Oceanic and Atmospheric Administration (NOAA) National Climatic Data Center (NCDC) (http://www.ncdc.noaa.gov/cdo-web/). The data used span June to

August, 1975–2014. To be consistent with the Rrs555 dataset interval, an eight-day mean temperature was calculated from the three-hourly air temperatures. We also analyzed summer (June–August) mean temperatures each year.

Wind is potentially responsible for oceanic upwelling in front of glaciers and hence for vertical transport of high turbidity water. We used wind speed data to calculate the magnitude of wind stress. Wind speed data were Cross-Calibrated Multi-Platform Ocean Surface Wind Vector L3.0 First-Look Analyses (Atlas et al., 2011). This dataset contains zonal and meridional wind speeds referenced to a height of 10 m, with spatial resolution of 0.25° and temporal resolution of six hours. We analyzed data from July to August during 2002–2011. Wind data were downloaded from the Physical Oceanography Distributed Active Archive Center (PO.DAAC) (http://podaac.jpl.nasa.gov/). Zonal and meridional wind speeds were transformed to absolute wind stress values. The absolute value ($\tau$: kg m$^{-1}$ s$^{-2}$) was calculated as follows (Nezlin and DiGiacomo, 2005);

$$\tau = \rho_{air} C_D U^2 \qquad (\text{kg m}^{-1}\ \text{s}^{-2}) \qquad (2.3),$$

where $\rho_{air}$ is air density (1.22 kg m$^{-3}$), $C_D$ is a dimensionless drag coefficient (0.0013), and $U$ is wind speed at 10 m above the surface (m s$^{-1}$). We calculated domain-averaged wind stress during expansion phase of the high turbidity area (from 1 July to the timing of annual maximum extent) to confirm the relationship between annual maximum extent of high turbidity water and quantity of hoisting sediments. The unit vector mean of wind stress direction was also computed. Direction is described moving clockwise through 360°, with 0° pointing northward.

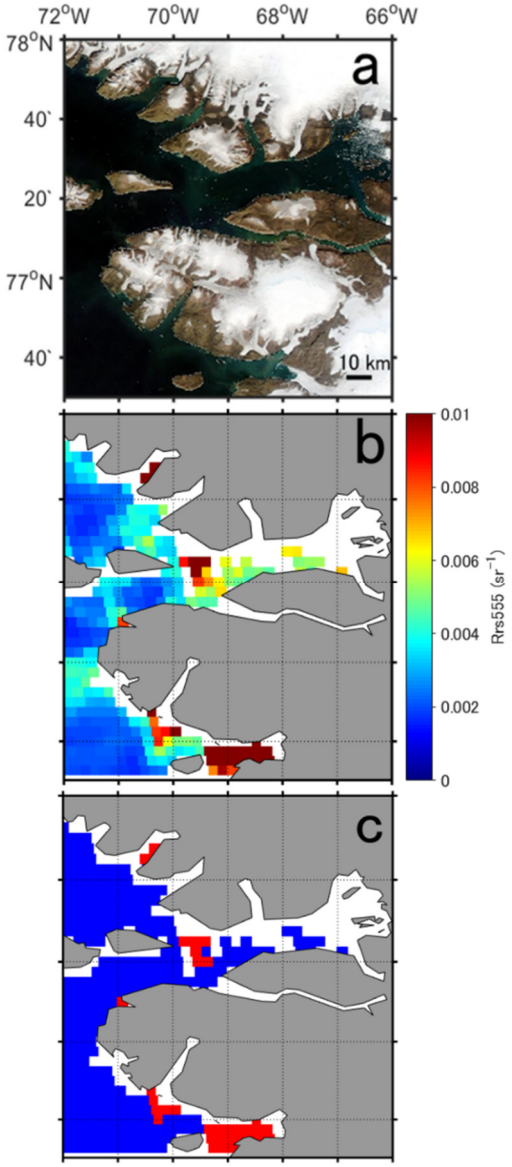


Fig. 2.2. (a) MODIS true color image (obtained from NASA Earthdata), (b) Rrs555 values, and (c) high turbidity area (Rrs555 ≥ 0.0070 $sr^{-1}$) indicated by red pixels on 16 July 2012. No data are available for the white region; land and ice sheet areas are indicated in grey in b and c.

## 2.3. Results on the Thule region

### 2.3.1. Distribution of high turbidity water

Temporal mean Rrs555 for the whole analysis period revealed distinct regional distributions within the study area (Fig. 2.3). High Rrs555 values were localized near the front of outlet glaciers terminating in the ocean and on land. Particularly in Wolstenholme Fjord, Rrs555 values were notably high (0.007–0.01 $sr^{-1}$) near the coast, but were relatively low (less than 0.004 $sr^{-1}$) in the offshore region away from the ice sheet.

Fig. 2.4 illustrates the number of years during 2002–2014 during which pixels were covered by the high turbidity area during its maximum extent in summer. Occurrence of more than one year was observed only in the proglacial ocean off the ice sheet. This result suggests that high turbidity water originates from discharge from the ice sheet and ice caps. In particular, Wolstenholme Fjord was more frequently (9–12 years) covered by high turbidity areas than other regions. The relatively small fjords on the northern flank of IB were also frequently affected by high turbidity conditions. On the other hand, occurrence of high turbidity events was lower (3–5 years) in the open coastal area adjacent to the ice sheet and ice caps. Similar results were obtained in IB. The frequency of high turbidity cover is therefore spatially heterogeneous and largely dependent on environmental characteristics, such as the size and depth of fjords.

### 2.3.2. Seasonal and interannual variations in high turbidity area

Fig. 2.5 shows the extent of eight-day composite high turbidity areas, shown from July to August for each year (2002–2014). During nine out of the studied 13 years, the high turbidity area began to increase in late June and its maximum extent was observed

between early July and early August. The turbid area then decreased between late August and early September. In the remaining four years, the high turbidity area continued to expand moderately until mid- and late August and then decreased.

To clarify the seasonal development of high turbidity areas, we calculated mean seasonal variations by stacking data from 2002 to 2014 (black line in Fig. 2.5). The high turbidity area increased from early July to mid-July, reaching 840 $km^2$. After mid-July, its extent decreased and reached 250 $km^2$ (about 29% of maximum extent) in late August. Seasonal changes in high turbidity areas were significantly correlated with air temperature ($R = 0.80$, $p < 0.01$) (black lines in Figs 2.5 and 2.6). This correlation suggests that the timing of maximum glacier surface melt, associated with highest air temperature, corresponds to the timing of the greatest extent of high turbidity water. In addition, surface melt seasons in northwestern Greenland during 2000–2006 extended from late June to early August, as indicated by remote sensing data analyses (Hall et al., 2008). The timing of the relatively large extent of high turbidity water in this study therefore roughly corresponds to the ice sheet melt season.

The annual maximum extent of the high turbidity area varied greatly from year to year (1340 ± 600 $km^2$) (Figs 2.5 and 2.7a). During the period of our analysis, maximum and minimum extents occurred in 2003 (2180 $km^2$) and in 2004 (430 $km^2$), respectively. The maximum areas in 2006–2008 and 2010–2012 (1590–2030 $km^2$) were greater than the mean over the study period, whereas those in 2002, 2005, 2013, and 2014 (670–820 $km^2$) were smaller than the mean. The timing of annual maximum extent also varied from year to year (Fig. 2.5). Annual maximum extents were reached before mid-July in 2003 and 2010–2012, corresponding to years of relatively large turbid water extent. By contrast, annual maximum extents occurred after late August in 2004–2005 and 2013–2014, when

the extents were relatively small. Our data thus shows that the maximum area was reached earlier in summer during years with relatively large turbid water expanses.

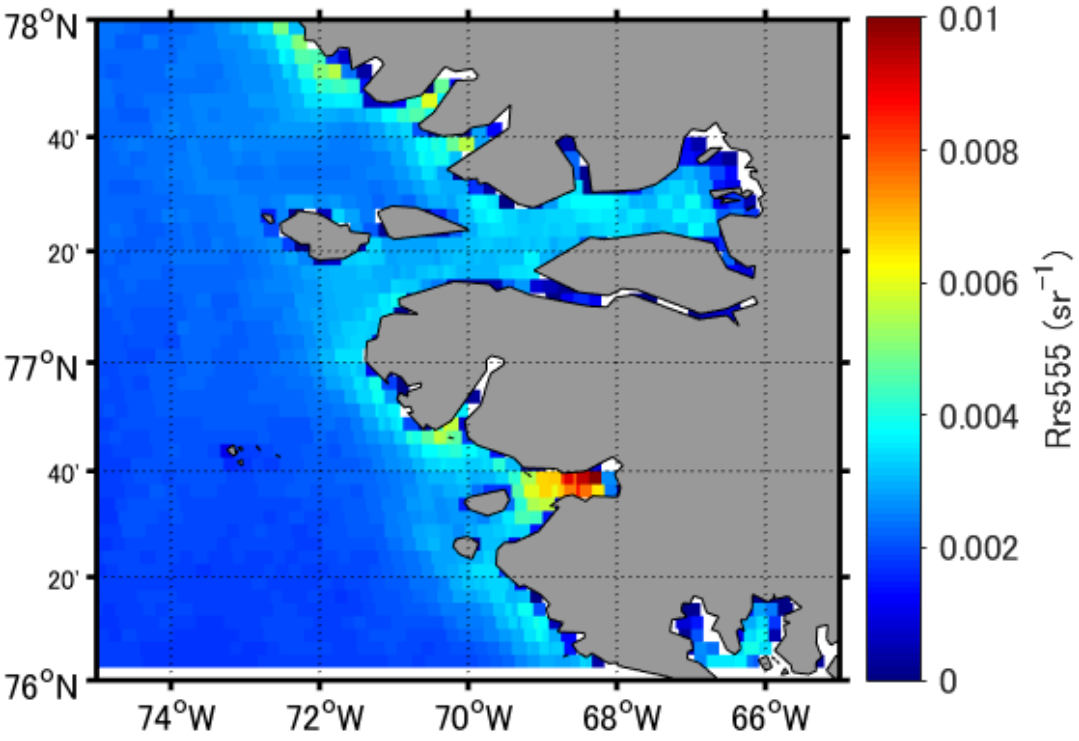


Fig. 2.3. Rrs555 values averaged from 2002 to 2014.

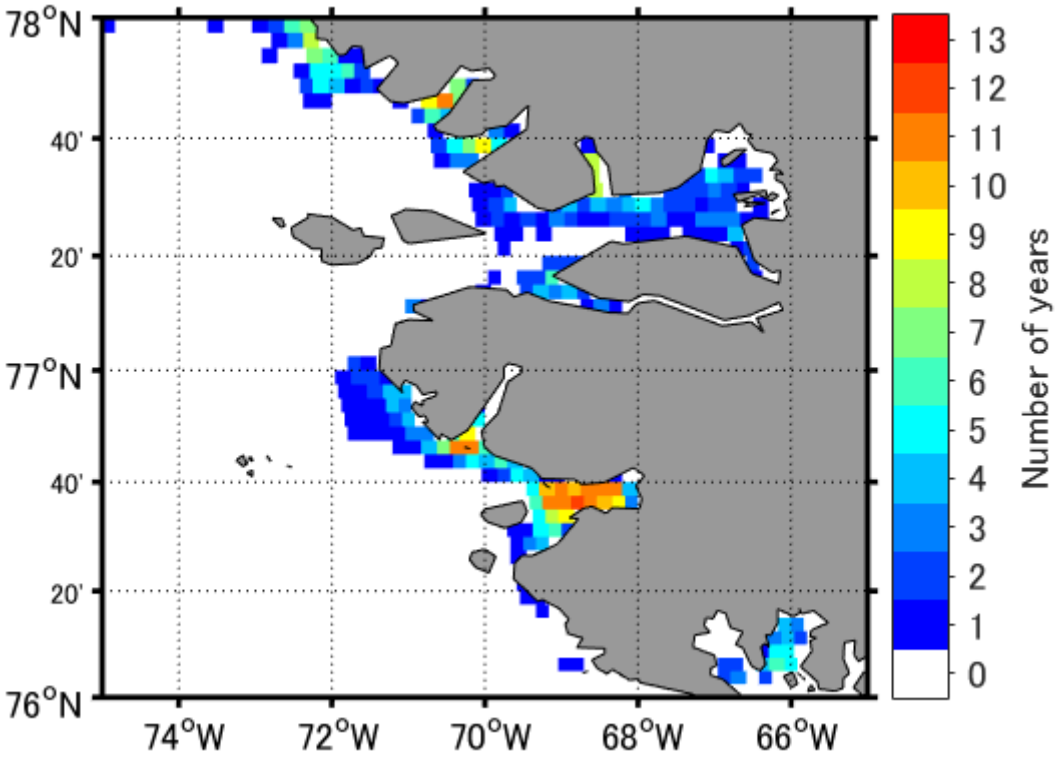


Fig. 2.4. Number of years over which each pixel was covered with the high turbidity area.

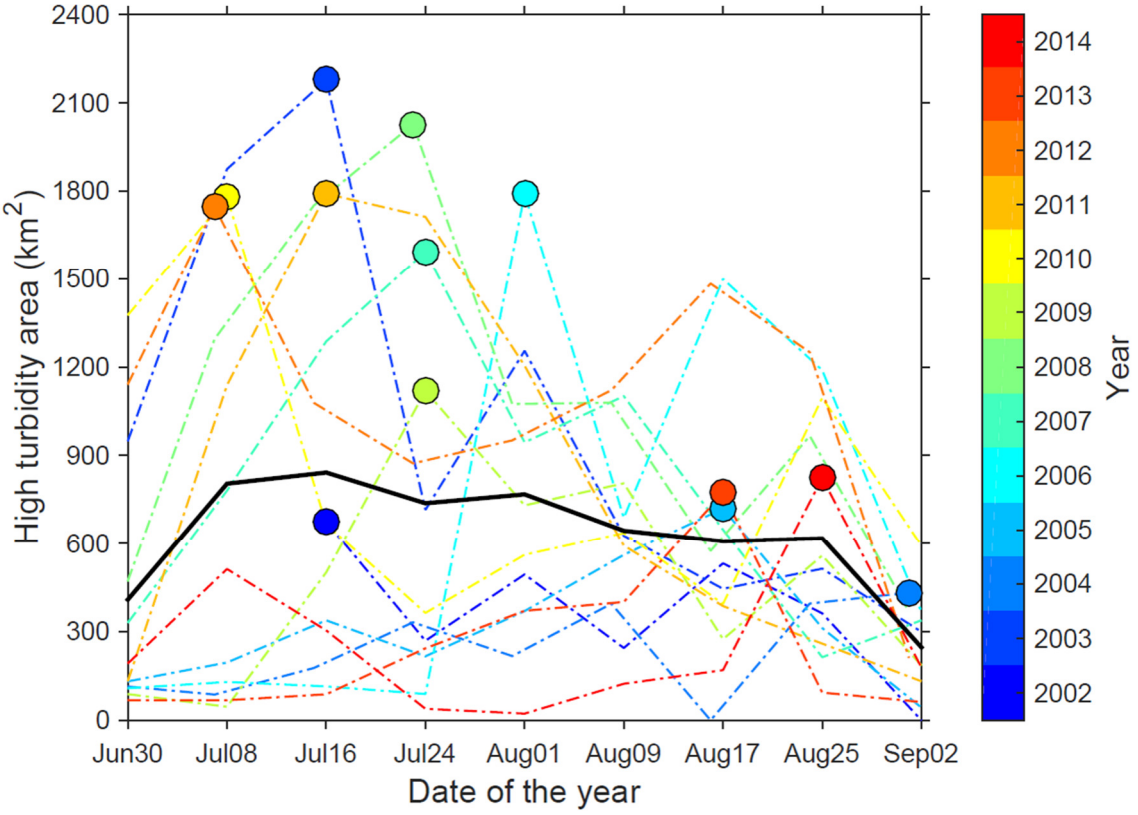


Fig. 2.5. Eight-day composite of total high turbidity area from July to August per year, with variations indicated by the color scale. The black line shows the mean over the period 2002–2014. Annual maximum extent in each year is indicated by the colored circle.

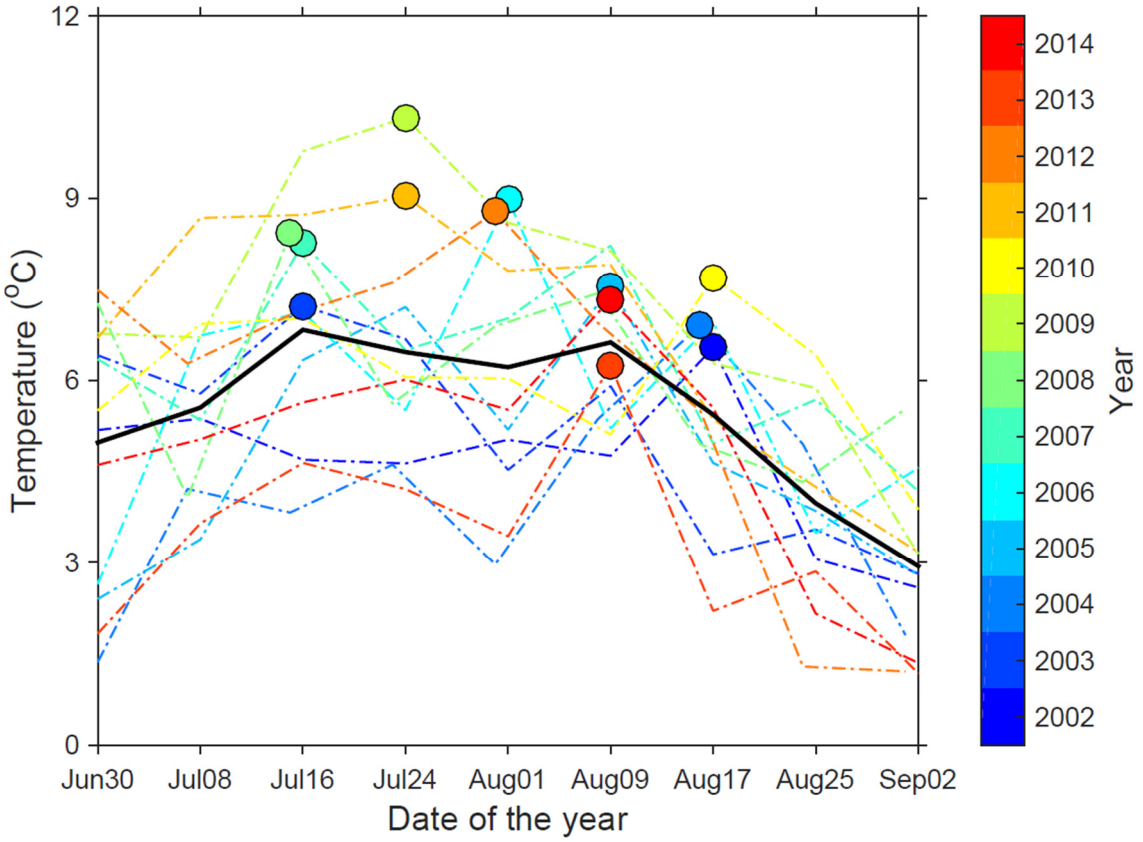


Fig. 2.6. Eight-day mean air temperature from July to August per year, with variations indicated by the color scale. The black line shows mean temperature over the period 2002–2014. Annual maximum temperatures are indicated by colored circles.

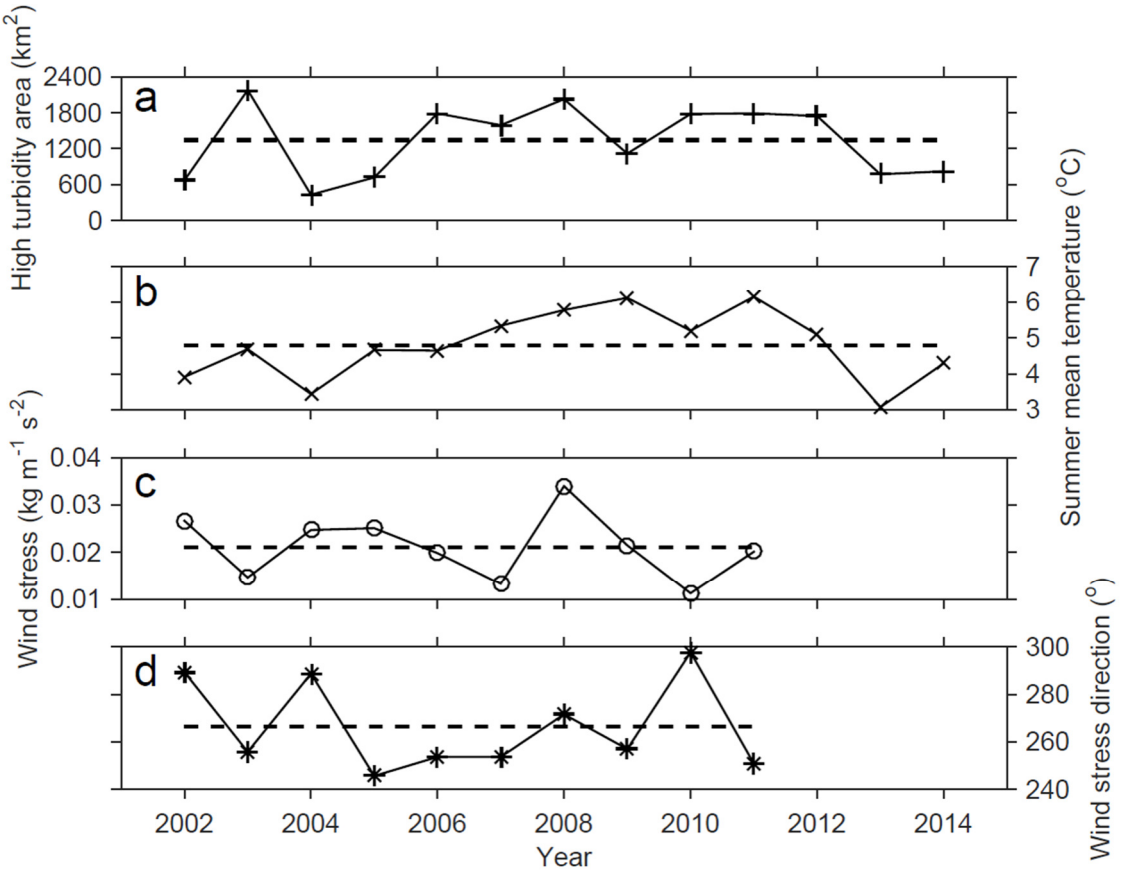


Fig. 2.7. (a) Annual maximum extent of high turbidity water, (b) summer (June–August) mean temperature at Thule Air Base, (c) wind stress averaged over the study area and (d) wind stress direction from 1 July to the timing of annual maximum extent. The dashed lines represent the mean over the study period.

## 2.4. Discussion on the Thule region

### 2.4.1. Mechanisms driving high turbidity water expansion

In this section, we discuss factors controlling annual variations in the extent of the high turbidity area (Fig. 2.7a). First, changes in the amount of turbid meltwater input from glaciers could be the main factor controlling variations in the high turbidity area. The high turbidity area off the ice sheet might extend larger in the years when the large quantities

of turbid glacial meltwater input, because of greater amounts of sediment transportation. The amount of meltwater input is controlled by the amount of surface melt, which is commonly assumed to be proportional to the sum of positive degree days (PDD) (e.g., Cuffey and Paterson, 2010). The extent of the high turbidity area therefore potentially reflects variations in air temperature. Second, the amount of sediment transport driven by wind should also be considered. Sea surface wind can induce Ekman drift of near surface water away, with upwelling of water from beneath the surface to replace the displaced surface water. Upwelled water carries sediments from lower and bottom layers and increases turbidity at the surface. Wind is therefore potentially important for expansion of the high turbidity area (Hetland, 2005; Walker et al., 2005).

To examine the importance of the above two mechanisms for turbid water distribution, we compared the high turbidity area with air temperature (as an indicator of glacial melt) and with wind stress (as an indicator of sediment re-suspension). We used the annual maximum extent of the high turbidity area, summer mean temperature, and wind stress and direction for the expansion phase of the high turbidity area. We defined the summer temperature as the mean from June to August, since air temperature at Thule reaches 0°C at the beginning of June suggesting the onset of glacier melt.

Summer mean temperature during 2002–2014 at Thule was 4.8 ± 1.0°C (Fig. 2.7b). Summer temperatures were relatively low in 2004 and 2013, and the anomalies during these years relative to the mean of 2002–2014 were −1.4°C and −1.7°C. In contrast to these two years, summer mean temperatures were above average during 2007–2012, and anomalies were 0.3–1.4°C. These summer temperature variations are consistent with interannual variations in the maximum extent of the high turbidity area (Figs 2.7a and b). The mean value of wind stress during the expansion phase of the high turbidity area was

0.021 ± 0.007 kg $m^{-1}$ $s^{-2}$ (Fig. 2.7c). Minimum and maximum wind stresses occurred in 2010 (0.012 kg $m^{-1}$ $s^{-2}$) and in 2008 (0.035 kg $m^{-1}$ $s^{-2}$), respectively. The anomaly relative to 2002–2014 mean was −0.009 kg $m^{-1}$ $s^{-2}$ in 2010 and 0.014 kg $m^{-1}$ $s^{-2}$ in 2008. The average direction of wind stress was roughly westward (266 ± 19°) (Fig. 2.7d). Mean wind stress direction shifted west-southwestward in 2005 (246°) and west-northwestward in 2002, 2004, and 2010 (289–298°). The correlations between wind parameters and the high turbidity area were unclear (Figs 2.7a, c, and d).

The annual maximum extent of the high turbidity area was significantly correlated with summer mean temperature at Thule (R = 0.64, p = 0.02) (Fig. 2.8a). This positive correlation suggests that the amount of turbid glacial meltwater input increases because of increasing amount of surface melting. On the other hand, no clear correlation was observed between the turbid area and the strength/direction of wind stress ($|R| < 0.4$, $p > 0.3$) (Figs 2.8b and c). There was no significant correlation with zonal or meridional components of wind stress. These results suggest that sediment transport resulting from wind-induced upwelling has only minor influence on high turbidity water near the ocean surface. To summarize, the source of the turbid water observed off the Thule region is most likely the discharge of glacial meltwater, rather than re-suspension of sediments.

From linear regression of the data (Fig. 2.8a), we found a relationship between summer mean temperature at Thule ($T_{\mathrm{Thule}}$ : °C) and the annual maximum extent of the high turbidity area ($A_{\mathrm{max}}$ : $km^2$);

$$A_{\mathrm{max}} = T_{\mathrm{Thule}} \times 400 - 580 \quad (\mathrm{km}^2) \qquad (2.4),$$

i.e., if summer mean temperature rises by 1°C, the extent of the high turbidity area will

increase by 400 $km^2$, equivalent to the area covered by about 150% of the Wolstenholme Fjord. In Kangerlussuaq Fjord, interannual variations in the extent of the sediment plume reflect ice sheet surface melt area in the drainage basin (Chu et al., 2009). Furthermore, the plume area in the same fjord is positively correlated with observed proglacial river discharge throughout the melt season (McGrath et al., 2010). Hudson et al. (2014) reported that a large amount of runoff causes high suspended sediment concentration (SSC) over an area where multiple river plumes were aggregated, although runoff is not correlated with SSC in each plume. Our result indicates the relationship between turbid water area and meltwater discharge that were previously reported for a relatively confined fjord are also applicable to the open ocean, as observed off the Thule region.

General annual variations trends can be explained by summer air temperatures, but our data suggest that the width and depth of fjords also affect distribution of the high turbidity area. For example, in the confined and shallow (< 200 m) Wolstenholme Fjord, a high turbidity area was observed even in the years when this had a relatively small extent (2004, 2005, 2013, and 2014) (Figs 2.1b, 2.4, and 2.5). In contrast, in the confined but deep fjord of IB (> 500 m), the high turbidity area was only observed during years when this had a relatively large extent. In a relatively confined and deep fjord such as IB, the turbidity density can decrease when simply averaged over the whole depth. Moreover, subglacial meltwater discharge can upwell and reach the fjord surface only given a large amount of discharge.

In addition to the above factors, advective dilution by ocean current can affect the high turbidity water extent. Although the detailed circulation pattern is not clear around Thule region, previous studies suggested that the ocean current on the shelf is weak (Hamilton and Wu, 2013; Münchow et al., 2015) and hence the effect of temporal

variability of ocean current is expected to be weak. With a lack of evidence, we conjecture the ocean current is not the primary factor in controlling the change in extent in this region but further assessment is needed.

Interannual variability in the timing of annual maximum extent is similar to the timing and magnitude variabilities of highest air temperatures (Figs 2.5 and 2.6). In the years when annual maximum extents were reached later and extents were relatively small (from mid-August to late August) (2004, 2005, 2013, and 2014), air temperatures reached their summer maximum relatively later (from early August to mid-August) and temperatures were low. On the contrary, in years when annual maximum extents were reached earlier and extents were relatively large, air temperatures reached their annual maximum earlier in summer and temperatures were relatively high. This relationship between the timing of the annual maximum extent high turbidity area and the highest air temperature implies that the whole sequence of processes, from ice surface melt and meltwater discharge to sediment settling, occurs within about two weeks.

### 2.4.2. Implications for large-scale and long-term variations in high turbidity area

As discussed in the previous section, the extent of high turbidity water off the Thule region is mainly controlled by the amount of glacial melt, influenced by air temperature changes. Greenland summer temperatures are inversely correlated with a summer North Atlantic Oscillation (NAO) index (Hanna et al., 2008; Hurrell, 1995). Previous studies have shown that annual temperature variations in Greenland correspond to changes in atmospheric circulation associated with NAO. Annual variations in the extent of high

turbidity water off Greenland are hence possibly associated with atmospheric circulation related to NAO. Because the influence of such climatic trends extends over large areas of Greenland, variations in the high turbidity area observed in this study are likely not limited to this geographical area but common to the entire area off Greenland.

Temperature rise in the Arctic region has been significant in recent years and a further warming trend is expected in future (IPCC, 2013). The summer mean temperature at Thule provides evidence of a warming trend at a rate of 0.05°C $a^{-1}$ over the last 40 years (1975–2014) ($R = 0.47$, $p < 0.01$) (Fig. 2.9). Assuming a linear relationship between annual maximum extent of the high turbidity area and summer temperature (Fig. 2.8a; Equation 2.4), annual maximum extent has increased by about 97% over the 30 years from 1975–1984 (730 $km^2$) to 2005–2014 (1440 $km^2$). It is hence likely that the high turbidity area has expanded under the influence of temperature rise and increasing amounts of glacial meltwater input.

The high turbidity area is expected to expand in future as a result of predicted warming of the Arctic region. It is estimated that summer mean temperature in Greenland will increase by 0.2–5.6°C from 1986–2005 to 2081–2100 in the Representative Concentration Pathway (RCP) 4.5 scenario (IPCC, 2013). Based on predicted temperature rise and on the correlation between the annual maximum extent of the high turbidity area and summer temperature, it is estimated that the high turbidity area will increase by 8–220% by the years 2081–2100, as compared with present conditions. The ocean along the Greenland coast will be more than what affected by turbid meltwater discharge from glaciers in future, and further study of related impacts on marine environments, such as on freshwater content, surface stratification, and biological productivity of coastal ecosystems, is thus urgently needed.

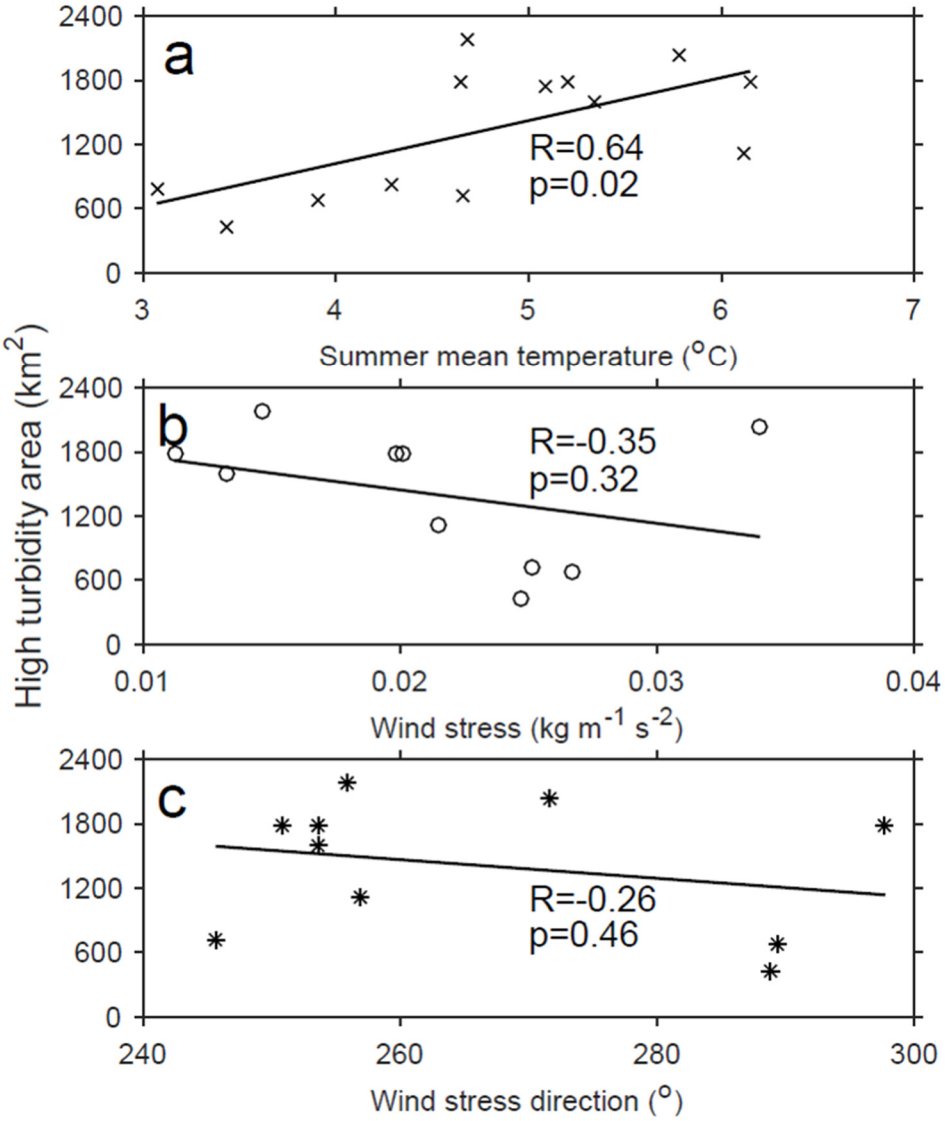


Fig. 2.8. Scatter plots of annual maximum extent of the high turbidity area and (a) summer mean temperature, (b) wind stress, and (c) wind stress direction from 1 July to the timing of annual maximum extent. Solid lines show linear regression of the data.

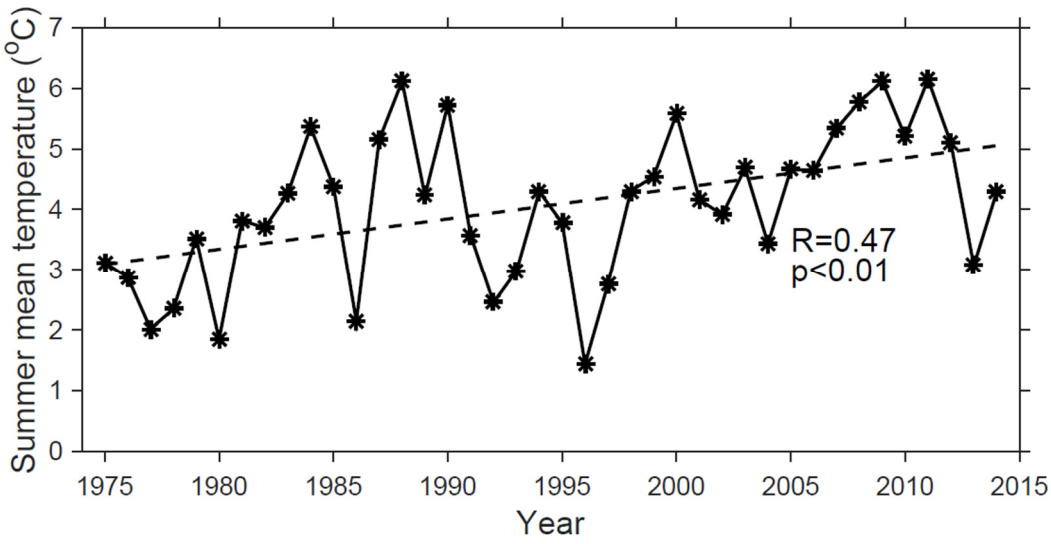


Fig. 2.9. Summer mean air temperature at Thule Air Base from 1975 to 2014. The dashed line shows linear regression of the data.

## 2.5. Regional characteristics of variability in the extent of high turbidity area off the western Greenland coast

### 2.5.1. Data and methods

To understand the characteristics in spatio-temporal variabilities of the extent of high turbidity surface area in more generally, this section focuses on a broader open fjords/ocean off the western Greenland (59–75°N, 43–61°W and 75–78.18°N, 43–75°W), including the Thule region. We divided the study area into 7 regions using the latitude at the boundary of each drainage based on the Greenland drainage divides, developed by the Goddard Ice Altimetry Group from ICESat data (Zwally et al., 2012; Fig. 2.10a). In each ocean area (A1–A7), the extent of high turbidity area (Rrs555 ≥ 0.0070 $sr^{-1}$) was calculated based on the same datasets and methods shown in section 2.2.

Distribution of continental ice and fjord structure are not homogeneous along the western Greenland coast. Continental ice extends close to the coast along the northern

half coast (A1–A4), while it ends far inland from the coast along the southern half (A5–A6). Due to the continental ice distribution, fjord system is almost directly connected to the open ocean in the northern half, while fine-scale fjord systems develop to the inland side in the southern half, especially in A5 and A6. Note that satellite images used here do not resolve these inland fjord systems adequately.

To investigate the factors controlling the extent of high turbidity area, we used air temperature data recorded at 17 weather stations in the western Greenland (blue circles in Fig. 2.10b). Air temperature data are distributed by the US NOAA NCDC (http://www.ncdc.noaa.gov/cdo-web/). The summer (June–August) mean temperature was analyzed from 2002 to 2014 in each region (A1–A7).

### 2.5.2. Distribution of high turbidity water

Fig. 2.11a shows Rrs555distribution averaged from 2002 to 2014 for the whole study area. Basically, Rrs555 was the highest (0.005–0.01 $sr^{-1}$) near the coast, rapidly decreasing to less than 0.003 $sr^{-1}$ to the offshore. Moreover, the distribution of high Rrs555 area varied largely along the coast as well. Particularly in A1 (off the Thule region corresponds approximately to the study area in previous sections) and in A3 (the northern Disko Bay where Jakobshavn Isbaræ, Greenland's largest outlet glacier, located; Fig. 2.11b), the high Rrs555 areas were broader than those in the other regions (e.g., A6 and A7 in Figs 2.11c and d).

Fig. 2.12 illustrates the number of years, during 2002–2014, that were covered by the high turbidity in summer for the three selected regions. Occurrence of more than one year was observed only in the proglacial ocean off the ice sheet in A3, roughly similar to the situation off the Thule region in A1 (Fig. 2.4). A3 (~11 years in Fig. 2.12a) was more

frequently covered by high turbidity areas than A6 and A7 (~4 years in Figs 2.12b and c).

Time series of annual mean and maximum extents of high turbidity area revealed regional characteristics (Figs 2.13 and 2.14) In A1, annual mean and maximum extents of high turbidity area averaged from 2002 to 2014 were the largest with the largest interannual variability (mean: 550 ± 290 $km^2$ in Figs 2.13a and 2.15a; maximum: 1160 ± 540 $km^2$ in Figs 2.14a and 2.15b). In A3, annual mean and maximum extents of high turbidity area averaged from 2002 to 2014 were the second largest (mean: 190 ± 80 $km^2$ in Figs 2.13c and 2.15a; maximum: 450 ± 180 $km^2$ in Figs 2.14c and 2.15b). On the other hand, in the southern half of A4–7, the annual maximum and mean extents of high turbidity area were small (mean: less than 50 $km^2$ in Figs 2.13d–g and 2.15a; maximum: less than 140 $km^2$ in Figs 2.14d–g and 2.15b), with small interannual variability. To summarize, the mean and variability of extent of high turbidity area were larger (280 ± 140 $km^2$) off the northwestern Greenland coast, while they were smaller (30 ± 20 $km^2$) off the southwestern Greenland coast.

### 2.5.3. Relationship between high turbidity water extent and air temperature

Off the Thule region, temporal change in the amount of turbid meltwater input from glaciers is likely to be the main factor controlling temporal variations in the high turbidity area (see section 2.4.1). Here, we likewise investigated the regional difference in relationship between the extent of high turbidity area and air temperature.

Air temperature variability was not homogeneous along the coast (Fig. 2.16). The southern regions was characterized with a shorter-interanual variability. For example, year-to-year variability was relatively small during 2005 and 2012 in A1, while high temperature was observed in 2003, 2005, 2010, and 2012 in A7. The mean variance of

summer mean temperature during 2002–2014 was larger (1.0ºC) in A1–3 (Figs 2.16a–c) while it was smaller (0.5ºC) in A5–7 (Figs 2.16e–g). The north-south contrast in temperature variance can lead to the larger variability in the amount of glacial discharge in the northern half region.

Relationship between the annual mean/maximum extent of the high turbidity area (Figs 2.13 and 2.14) and summer mean temperature revealed strong positive correlations in A1 and A3 ($R \geq 0.7$, $p \leq 0.01$; Fig. 2.17). Temperature had statistically significant correlations with the mean extent in A2, the maximum extent in A4, and the mean extent in A7 ($R > 0.5$, $p < 0.1$). The relationship suggests that the temperature variability is representative of glacial meltwater discharge and extent of observed turbid water is largely influenced by the turbid glacial meltwater. On the other hand, in A5 (the mean extent) and A6, the correlation was not significant ($|R| < 0.3$, $p > 0.4$). The poor correlation implies that the other factors control the high turbidity area, although the variabilities in turbid area are far smaller compared to the northern regions.

### 2.5.4. Factors controlling the regional characteristics

General correspondence between the turbidity area and summer air temperature was obtained. The relationship is in favor of the high glacial meltwater discharge and subsequent turbid area, which was described in previous subsection. However, the relationship was not applicable in the regions A5 and A6. In this section, we discuss the factors influencing the regional characteristics of variability in the extent of high turbidity area.

First, the extent of shallow continental shelf can affect the high turbidity water area,

possibly through the settings of oceanic current. Off the northwestern coast (A1–3), shallow water areas spread over a relatively large area (mean water depth of 60–140 m; Figs 2.18a and b), while in the southern coast (A6 and A7), deep water areas (> 500 m) come close the coast (mean water depth of 430–500 m; Figs 2.18a and b). Hence, the distribution of shallow continental shelf might be favorable in insulating the turbid meltwater against swift advection and diffusion.

Second, the glacier front position relative to the ocean can also affect the high turbidity water extent. In the northwestern region that glacier front reaches near the open ocean/fjord, turbid glacial meltwater inflows directly into open ocean, and thus high turbidity area is likely to extend larger and vary under the influence of glacial meltwater discharge. On the contrary, in the regions in A5 and A6 that glacier terminates in the inner narrow fjord and doesn't reach near the open ocean/fjord, the whole sequence of processes, from ice surface melt and meltwater discharge to sediment settling, can complete in the inner fjord. Moreover, the method adopted here don't resolve the inland fjord process. A previous study revealed the relationship between the extent of sediment plume and ice sheet surface melt area in Kangerlussuaq Fjord that is inland fjord (Chu et al., 2009), and hence the fine-scale analysis might support a similar relationship between turbid water area and air temperature. Thus, the regional difference in the glacier front positions can also affect the high turbidity water extent and its relationship with air temperature.

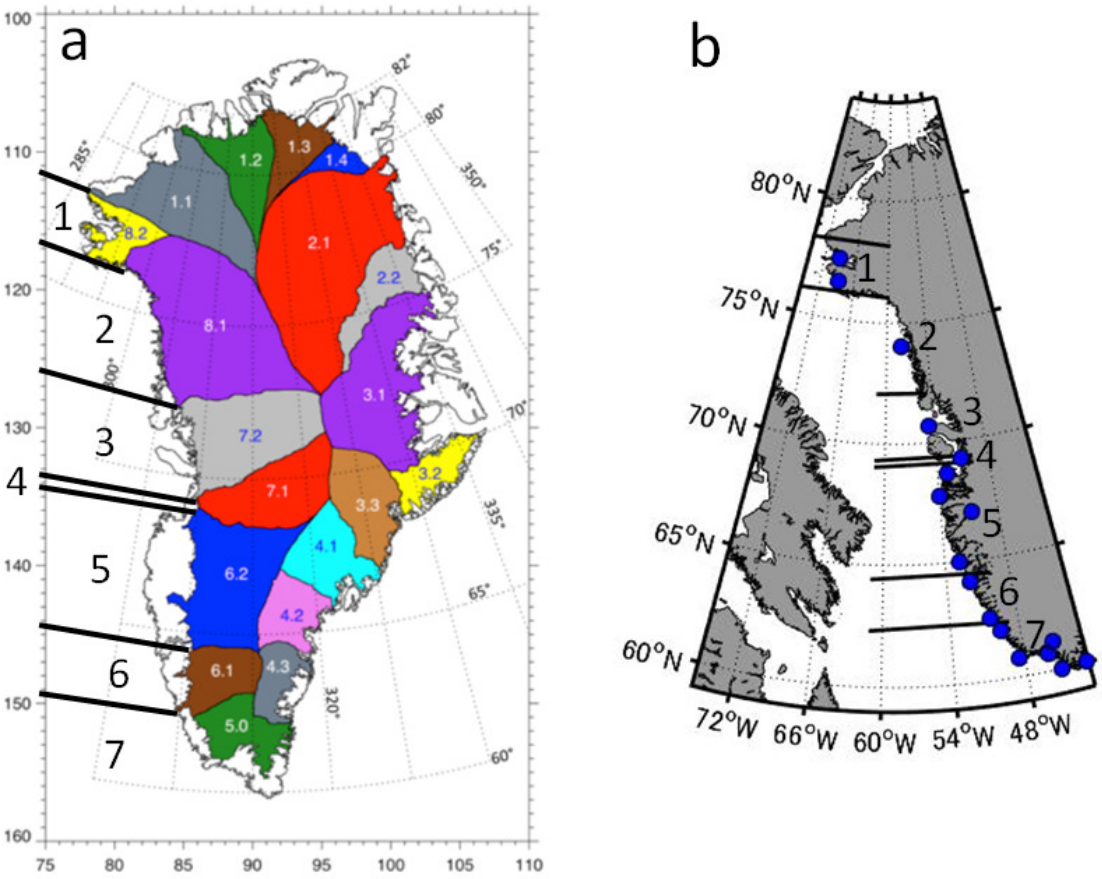


Fig. 2.10. (a) Greenland drainage divides and corresponding ocean areas divides. The drainage divides are based on Zwally et al. (2012). (b) The locations of weather station recorded at air temperature in this study area (indicated by blue circles).

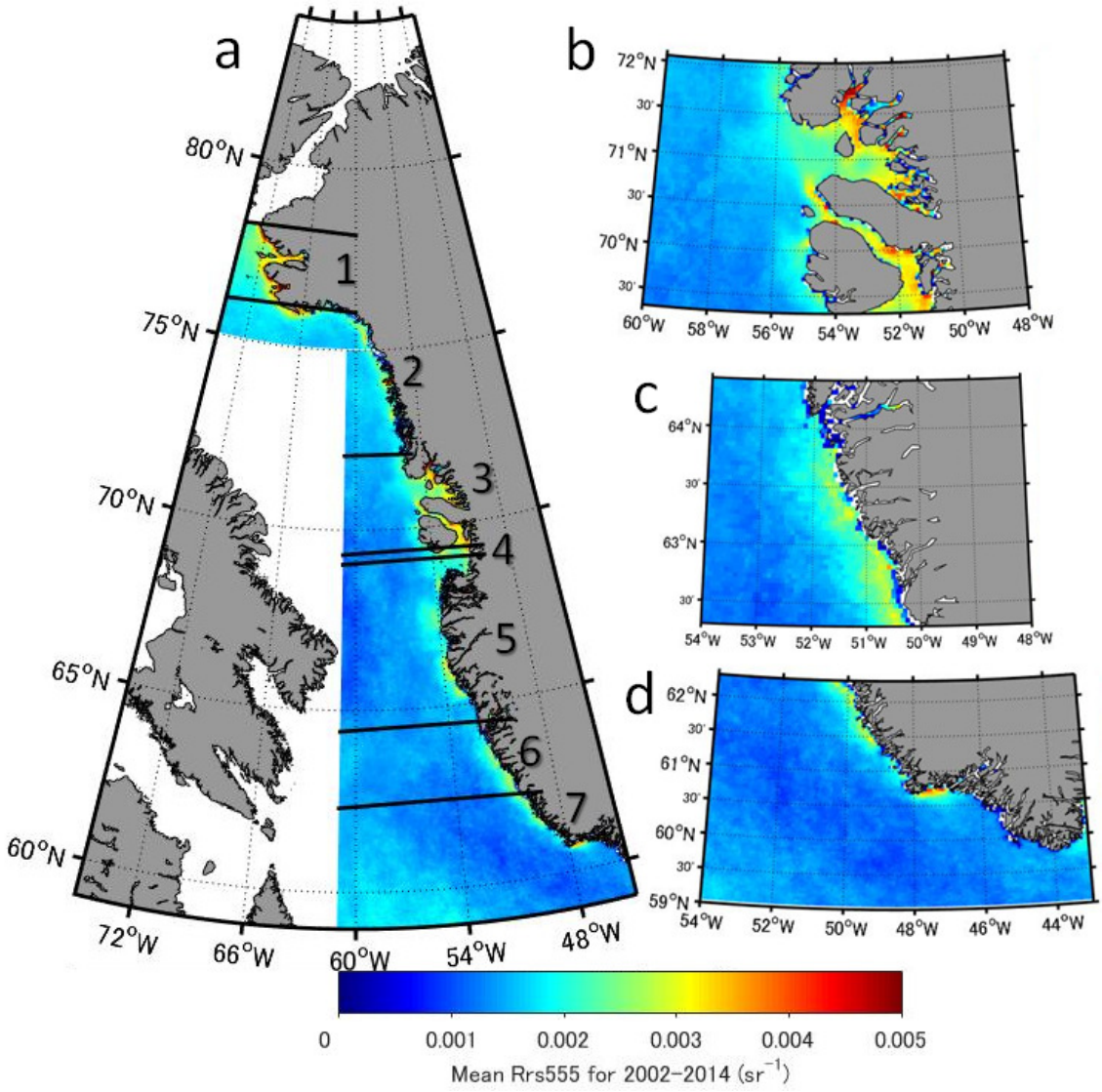


Fig. 2.11. Rrs555 values averaged from 2002 to 2014 (a) in the whole study area and in the coastal region of (b) A3 (48–60ºW), (c) A6 (48–54ºW) and (d) A7 (43–54ºW).

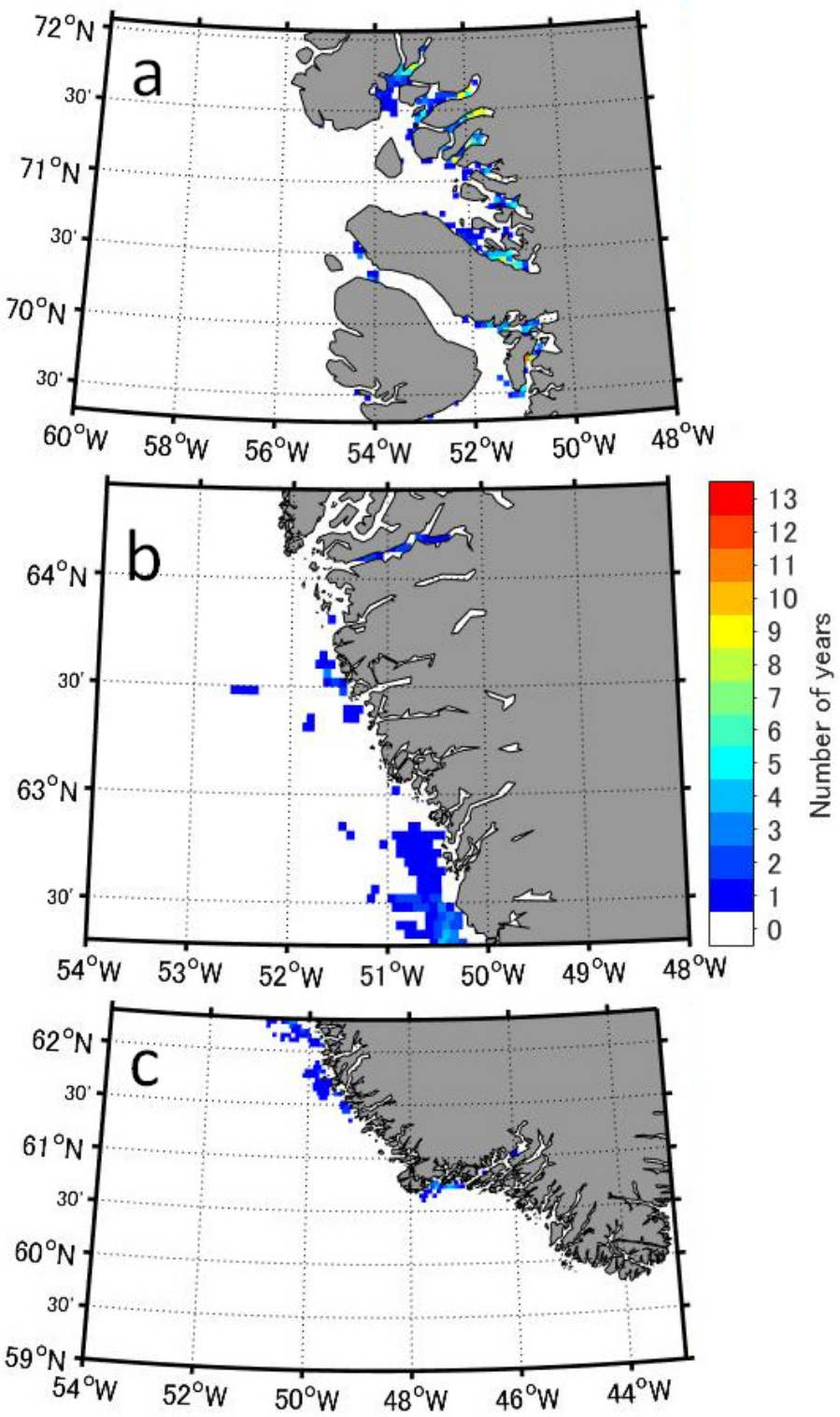


Fig. 2.12. Number of years over which pixels were covered by the high turbidity area during its maximum extent in summer in the coastal region of (a) A3 (48–60°W), (b) A6 (48–54°W) and (c) A7 (43–54°W).

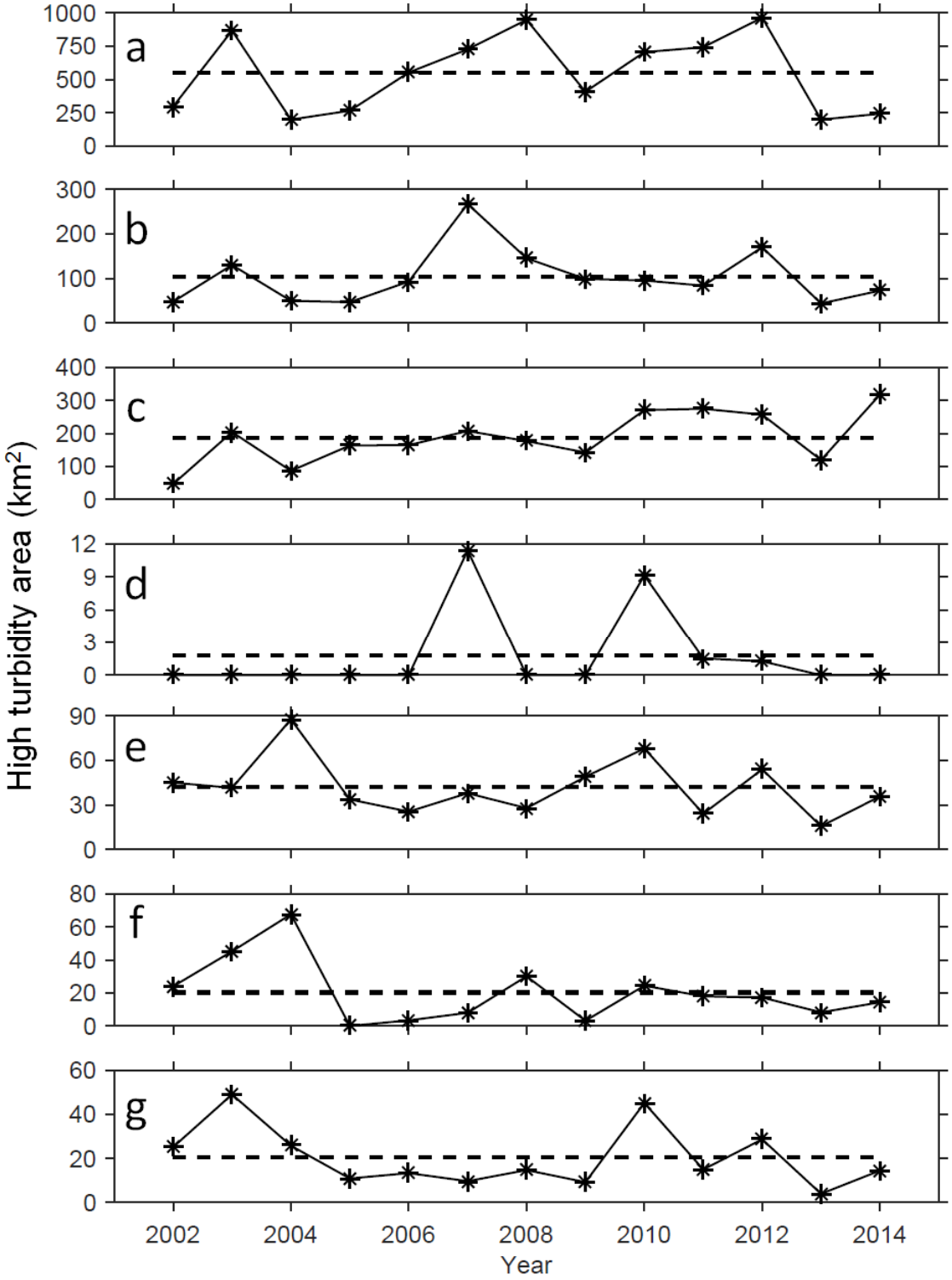


Fig. 2.13. Annual mean extent of high turbidity area in (a) A1, (b) A2, (c) A3, (d) A4, (e) A5, (f) A6 and (g) A7. The dashed lines represent the mean over the study period.

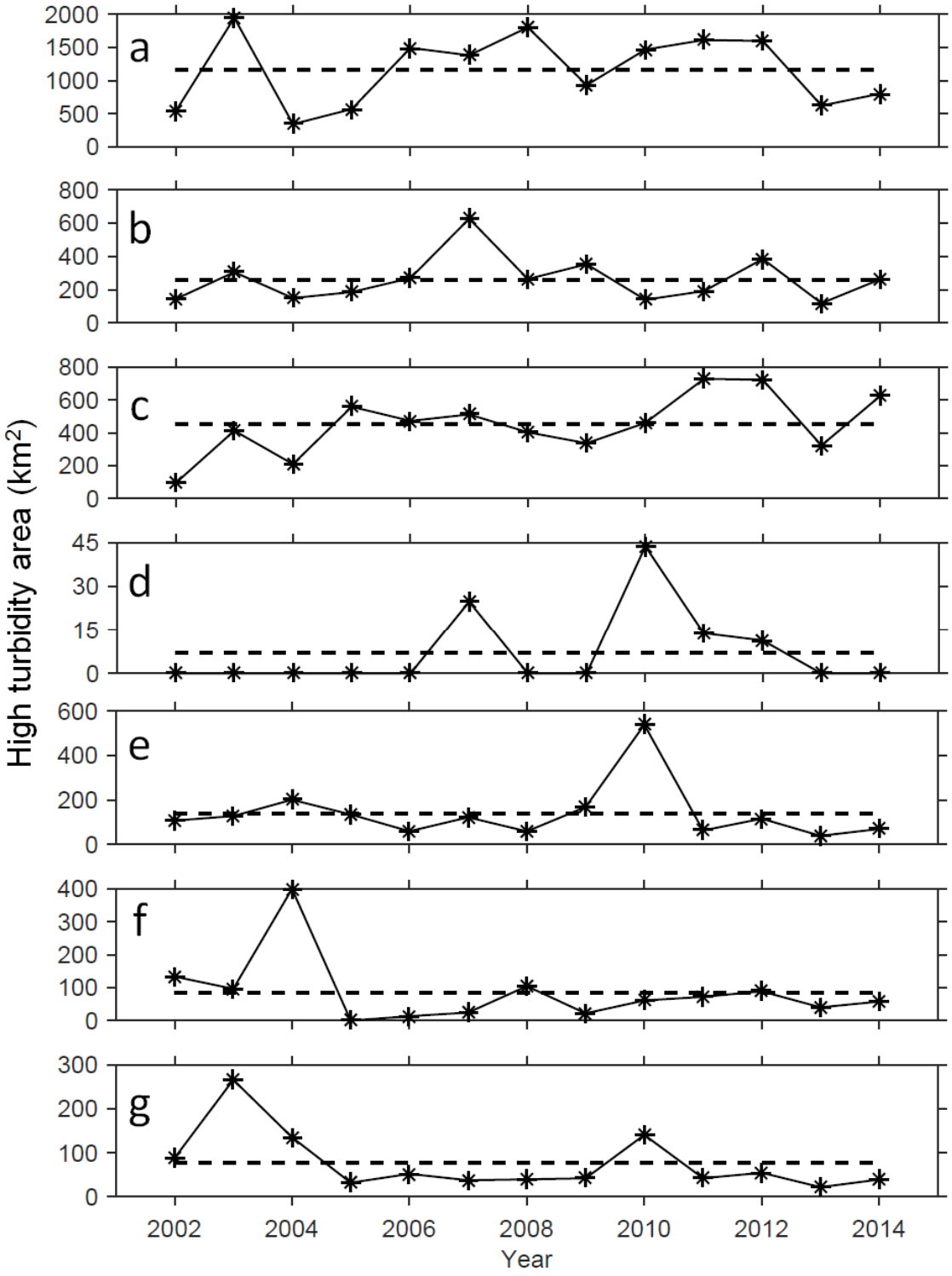


Fig. 2.14. Same as Fig. 2.13, but for annual maximum extent of high turbidity area.

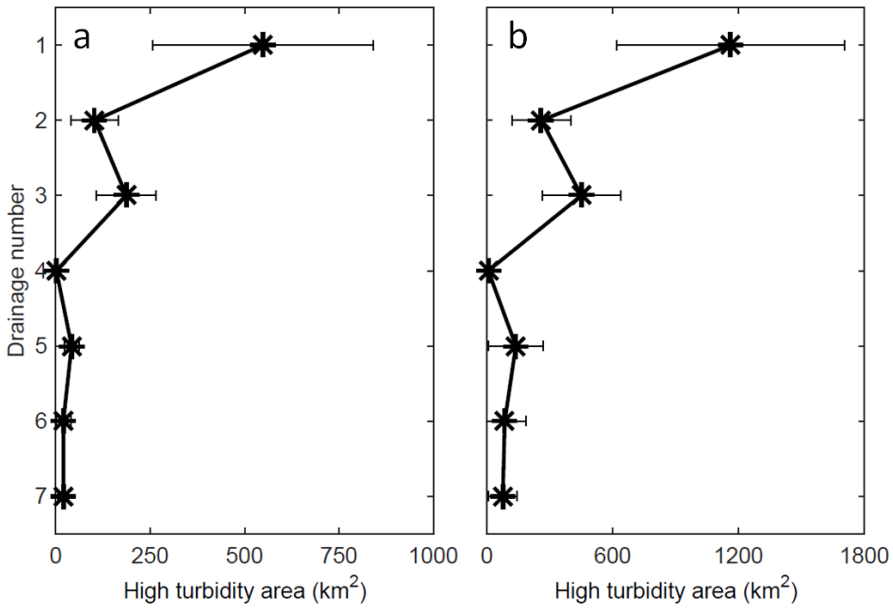


Fig. 2.15. Annual variations in the (a) mean (Fig. 2.13) and (b) maximum (Fig. 2.14) extent of high turbidity area in each region. Asterisk and error bar represent the extent averaged from 2002 to 2014 and its standard deviation, respectively.

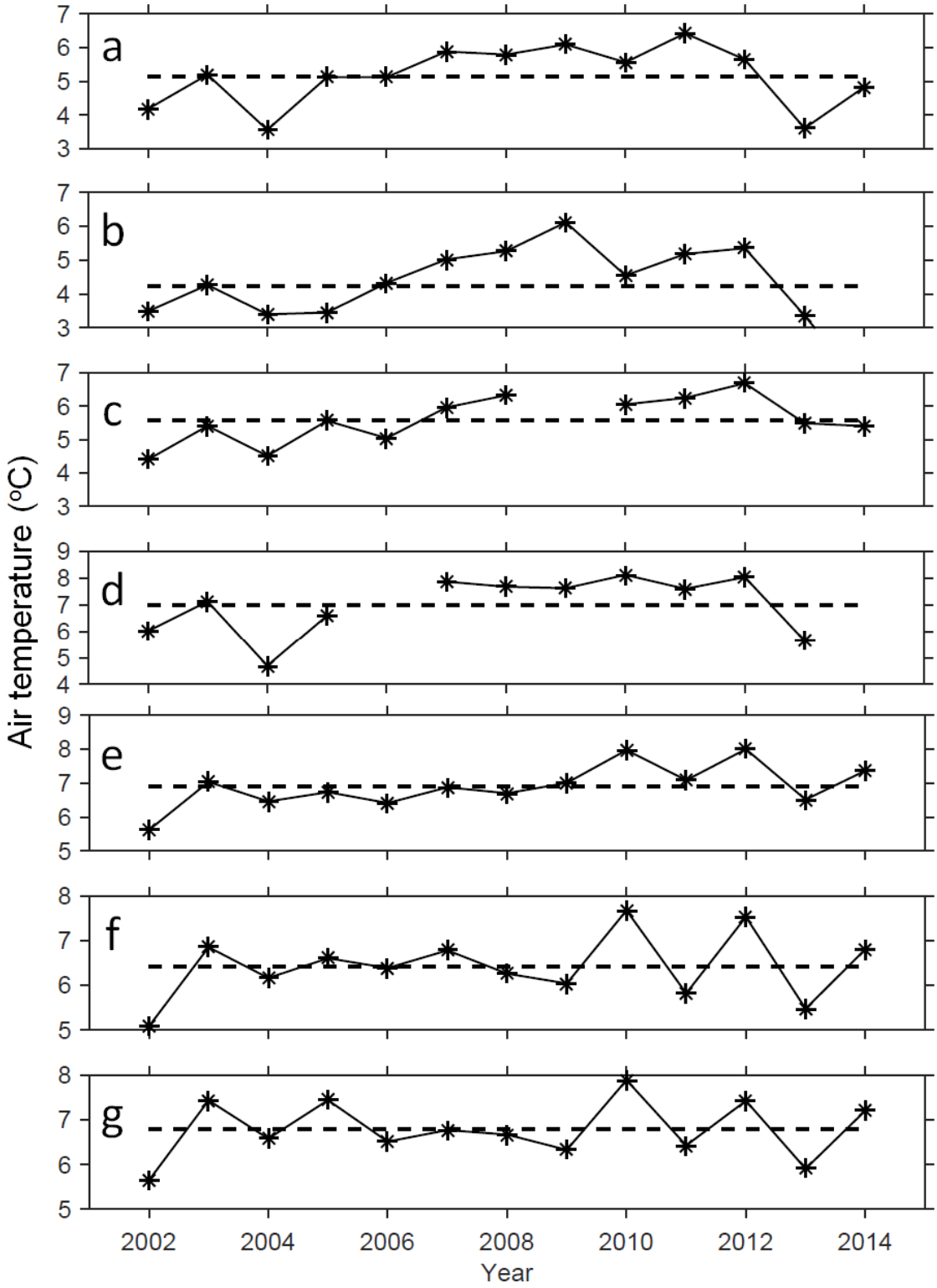


Fig. 2.16. Same as Fig. 2.13, but for summer (June–August) mean temperature.

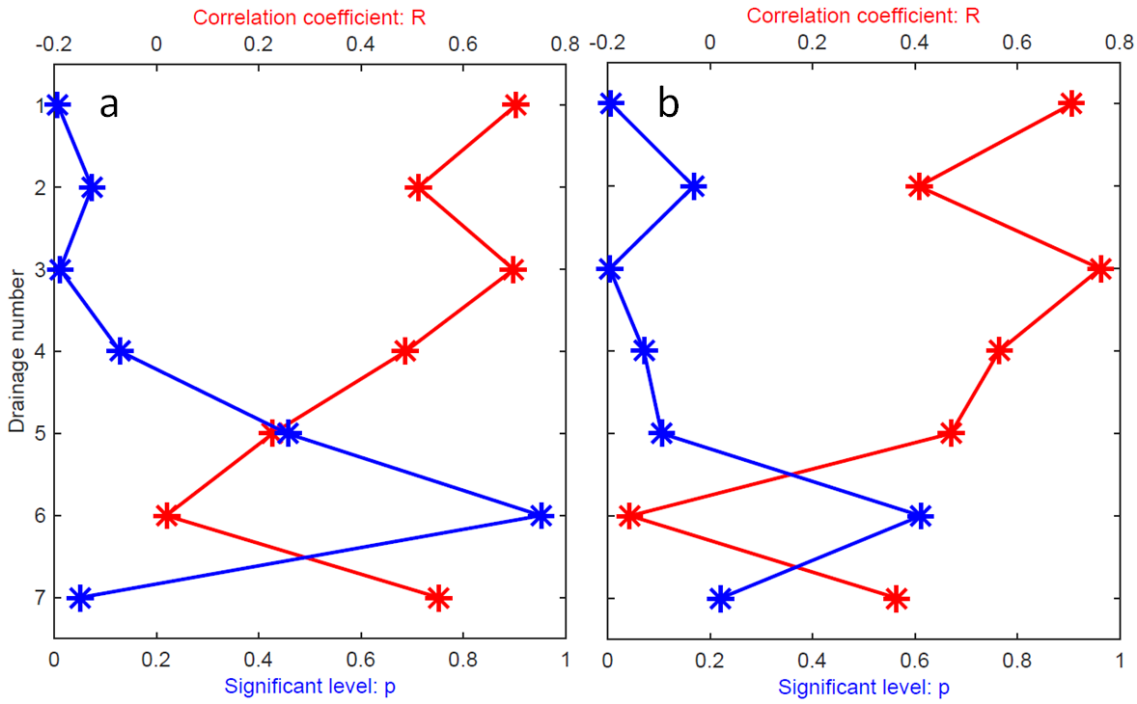


Fig. 2.17. The correlation between the annual (a) mean (Fig. 2.13) and (b) maximum (Fig. 2.14) extent of high turbidity area and summer mean temperature (Fig. 2.16). Correlation coefficient: R (red) and significance level: p (blue).

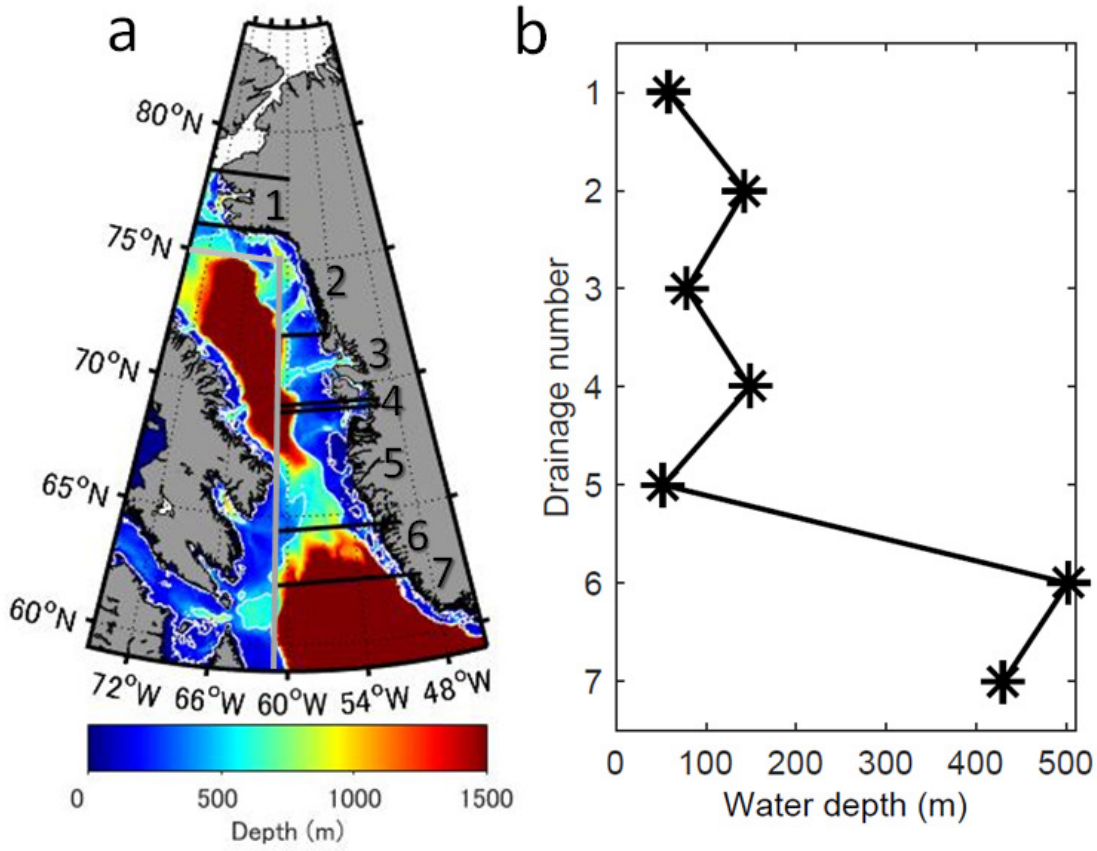


Fig. 2.18. (a) Ocean bathymetry in the study area (ETOPO1 developed by NOAA NGDC); white contours are 100 m and 500 m. Gray line is the boundary of study area. (b) Mean water depth in each region.

## 2.6. Summary

Spatial and temporal variations in high turbidity water off the Thule region in northwestern Greenland were analyzed using Rrs555 data from Aqua/MODIS satellites. The high turbidity area was distributed near the front of outlet glaciers that discharge glacial meltwater from the ice sheet and ice caps. The turbid water area increased in mid-July and its annual maximum extent varied greatly from year to year (1340 ± 600 $km^2$). These year-to-year variations in annual maximum extent of the high turbidity area in

summer were positively correlated with air temperature measured at Thule ($R > 0.6$, $p < 0.05$); on the other hand, their correlation with wind stress was poor ($|R| < 0.4$, $p > 0.3$). These results suggest that the extent of observed turbid water is largely influenced by the discharge of turbid glacial meltwater rather than by re-suspension of sediments driven by wind mixing. Assuming a linear relationship between the annual maximum high turbidity area and summer mean air temperature ($A_{max} = T_{Thule} \times 400 - 580$), we estimated long-term variations in the high turbidity area. Moreover, with a focus on a broader open fjords/ocean off the western Greenland including the Thule region, the relationship between the turbidity area and discharge is likely applicable to the regions that consist of the relatively large shelf area and glaciers located near the open ocean/fjord. Given the prevailing warming trend over the Greenland, this imply a potential glacial impact on the broader shelf environment. However, in the regions that consist of narrow protected fjords such as A5–6, the extent of high turbidity area were not explained with the same relationship, possibly partly due to the limitations in satellite spatial resolutions. The detailed assessment of the extent of high turbidity area by using the remote sensing data with higher spatial resolution are required as the future work.

# Chapter 3

# Subglacial meltwater distribution and its interannual variability in Bowdoin Fjord, northwestern Greenland

## 3.1. Study area

This study focuses on Bowdoin Fjord (BF; 77.6ºN, 66.8ºW; 3–5 km wide and 20 km long), one of the arms of Inglefield Bredning (IB) off the Thule region in northwestern Greenland (Fig. 3.1). During summer melt season, highly turbid ocean surface areas are formed in the vicinity of the ice sheet and glaciers as a result of glacial meltwater discharge (Ohashi et al., 2016). The aerial extent of the high turbidity surface varies from year to year, depending on glacial melt amount controlled by air temperature. The previous study suggested a potential correlation between glacial meltwater discharge and turbid area extent off northwestern Greenland (Ohashi et al., 2016).

Detailed bathymetry of BF is not entirely known, but was surveyed with an echo sounder along the centerline and several profiles across the fjord (Sugiyama et al., 2015). The water depth at the ice front of Bowdoin Glacier (BG) is about 210 m. It is hence assumed that subglacial meltwater discharges from a drainage conduit located at 210 m below sea level. The subglacial discharge occurs at a depth between warm AW (at the deepest part of fjord) and cold PW (at 50–150 m depth), where water properties are expected to change according to the relative influence of AW and PW. BF is thus suitable for assessing the impact of interannual variability in water properties on the distribution of subglacial meltwater.

To help understanding causes of oceanic interannual variability, air temperature data taken at Qaanaaq Airport located ~30 km southwest to the BG are used (77.47ºN, 69.23ºW,

16 m a.s.l.; blue circle in Fig. 3.1a). In 2014, daily mean air temperature rose above 0°C in early June, whereas it happened in late May in 2016. This observation suggests that surface melting and subsequent subglacial meltwater discharge began earlier in 2016. The amount of subglacial meltwater discharge is controlled by the amount of surface melt, which is commonly estimated with PDD. We used the PDD at the Qaanaaq Airport as a proxy of subglacial meltwater discharge from BG. The PDD was approximately 20% greater in 2016 than in 2014, which suggests a greater amount of subglacial meltwater discharge in 2016.

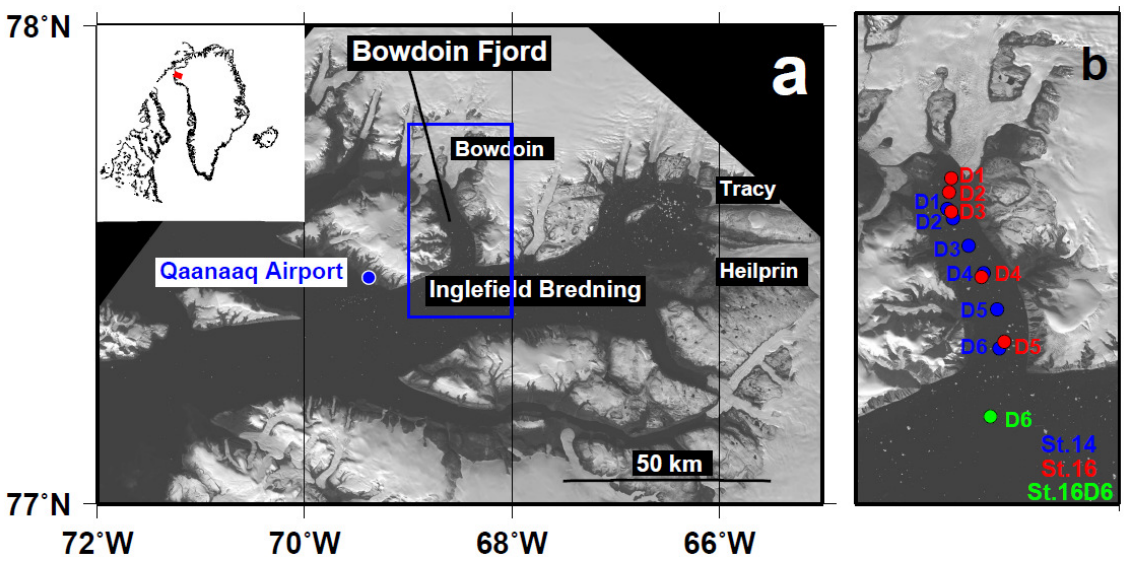


Fig. 3.1. Study region in Bowdoin Fjord. (a) Bowdoin Fjord in the northwestern Greenland depicted on the Landsat image taken on 6 September 2014. The blue box indicates the area shown in b. The inset shows the location of the region in Greenland. (b) The CTD observation sites were indicated by the dots (blue in 2014, red located in Bowdoin Fjord in 2016, and green located outside of Bowdoin Fjord in 2016).

## 3.2. Ocean observations

### 3.2.1. Observational methods

We carried out CTD observations in BF in the summers of 2014 and 2016. The observations were performed along the centerline of the fjord at 6 locations each year; at Sts 14D1–6 on 4th August, 2014 and at Sts 16D1–6 on 29th July, 2016 (Fig. 3.1b). St. 16D6 in 2016 was located in IB, approximately 4 km from the mouth of BF. A CTD profiler (RINKO Profiler ASTD-102, JFE Advantec) was lowered from a boat to measure profiles of temperature, salinity and turbidity from the surface to the bottom of the fjord. The sampling interval was 1s, which is equivalent to a vertical resolution of about 1 m. The precision of the depth, temperature, salinity and turbidity measurements were 1.8 m, 0.01°C, 0.01 and 0.3 Formazin Turbidity Unit (FTU), respectively.

In 2016, 33 water samples were collected at Sts 16D2–6 to calibrate the salinity measurement. The sampling was performed at depths deeper than 10 m to avoid the influence of steep salinity gradient near the surface. Salinities of the sampled water were measured using a Salinometer (Guideline Autosal 8400B) to correct the in-situ measurements with the CTD. The uncertainty of salinity (~0.01) makes it difficult to compare the absolute value of salinity, but the vertical structure of salinity could be valid.

### 3.2.2. Observational results

From the bottom to surface, layers of warm and saline AW (its core represented by potential temperature maximum; $\theta_{max}$), cold PW (its core represented by potential temperature minimum; $\theta_{min}$), and significantly warm and fresh SW were observed both in 2014 and 2016 (Fig. 3.2). In 2016, $\theta$–$S$ property was uniformly distributed over the

study area including St. 16D6 (outside of BF) at the depths deeper than the PW core, while it was different between inside and outside of the fjord at the depth shallower than the PW core. At St. 16D6, temperature monotonically increased towards the surface, suggesting the development of seasonal pycnocline. In the BF, on the other hand, temperature increased from PW core towards upper layer but decreased again. There are some differences in water properties, temperature in particular, between 2014 and 2016. The details of vertical distributions of potential temperature, salinity and turbidity and their year-to-year variability are shown in the subsequent section.

### 3.2.2.1. Potential temperature

Although the temperature structures were basically similar in both years, their details showed notable interannual difference. The AW core was observed at the depths near 290 m (1.3°C) in 2014 and 320 m (1.0°C) in 2016, respectively (Figs 3.3a–d). At the deepest part of the fjord, the thickness of warm layer (> 0°C) was thinner in 2016 (from the bottom to 230 m) than in 2014 (to 190 m). Furthermore, the PW core was observed at the depth of 150 m (−0.8°C) in 2014 and 170 m (−0.8°C) in 2016, respectively. Because of the differences in the core temperature and thickness of warm layer between the two years, temperature near the BG drainage conduit (210 m) was colder in 2016 than in 2014 by up to 0.9°C (Figs 3.3e and f). Below 210 m, temperature was also colder in 2016.

For the depths shallower than 150–170 m (the PW core), the coldest water in 2014 (−1.0°C; hereinafter, referred to as "local $\theta_{min}$") was observed at the depth of 80 m (Figs 3.2 and 3.3); the temperature at local $\theta_{min}$ was even colder than that at PW core. In 2016, the corresponding local $\theta_{min}$ was not observed above the PW core. Instead, a clear

temperature maximum (0.2°C; hereinafter, referred to as "local $\theta_{max}$") was found at the depth of 60 m. Because the increase in temperature from the PW core to local $\theta_{max}$ in BF is roughly the same with that outside of BF, water property in the fjord could have revealed the seasonal pycnocline on the wider area.

At the depth shallower than 20 m, water temperature increased rapidly to the surface in both 2014 and 2016. Temperature was colder in 2016 than in 2014 by up to 2.3°C at 5–20 m depths.

### 3.2.2.2. Salinity, potential density and stratification

Year to year salinity difference varied vertically. At the depth deeper than 210 m including the AW core, salinity was similar between the two years (Figs 3.4a–d), although salinity at the AW core was different (34.1 in 2014 and 34.2 in 2016). At the depth of 5–170 m (shallower than the PW core), salinity was higher in 2016 than in 2014 including the salinity difference at the PW core (33.5 in 2014 and 33.7 in 2016). In particular near the surface (5–20 m), the difference was more significant (0.6–1.6). In contrast, salinity at the surface (0–5 m) was lower in 2016 except the outer portion of BF.

The vertical distribution of potential density was mainly controlled by salinity (Fig. 3.5), and hence difference in potential density between 2014 and 2016 was mostly the same as that in salinity. At the depth of 5–170 m, potential density was higher in 2016 than in 2014, while at 0–5 m it was lower in 2016.

The square of Brunt-Väisälä frequency ($N^2$), a proxy for the strength of density stratification, increased towards the surface in both years. In particular at the depth shallower than 10–15 m, $N^2$ was the highest (> 0.001 $s^{-2}$), representing the strongest stratification at all depths (Figs 3.6a–d). As for the interannual $N^2$ difference, $N^2$ was

higher in 2016 than in 2014 at the depth shallower than 10 m, while $N^2$ in 2016 was lower by up to 0.0007 $s^{-2}$ at the depth of 10–50 m (Figs 3.6e and f). Thus, the stratification in 2016 was stronger near the surface (0–10 m) but weaker at the subsurface (10–50 m).

### 3.2.2.3. Turbidity

Turbidity acts as an effective tracer of subglacial meltwater. The highest turbidity layer (> 4 FTU) was found not exactly at the surface but at the subsurface of 15–50 m in 2014 and 10–40 m in 2016 (Figs 3.7a–d). Turbidity decreased from this layer to about 100 m depth and it was almost zero at the depth deeper than 150 m. In addition, turbidity decreased with the distance from the ice front toward the mouth of the fjord, which is in contrast to the temperature and salinity that changed little horizontally.

Distribution in turbidity changed between the two years. Further offshore around 10 m in 2014, low turbidity layer existed between the above and below higher turbidity layers. In 2016, on the other hand, turbidity was nearly homogeneous for the depth range of 0–40 m, and there was no discontinuity at 10 m depth. Turbidity at the depth of 0–15 m was hence 1–2 FTU higher in 2016 than in 2014 (Figs 3.7e and f). While at the depth of 40–150 m within 5 km from the ice front in 2014, turbidity was relatively high (> 1 FTU; Fig. 3.7b). In 2016, relatively high turbidity layer not existed at the depth deeper than around 60 m. Therefore, turbidity at the depth of 15–200 m within 5 km from the ice front was lower in 2016 than in 2014. Especially at the depth of 20–120 m, the difference was significant (up to 1.5–5 FTU). These differences in turbidity could be attributed to annual variations in the fraction of subglacial meltwater, which will be elaborated in the next section.

### 3.2.3. Freshwater fraction analysis

#### 3.2.3.1. Estimation method

In the proglacial fjord, sea water is influenced by freshwaters from subglacial meltwater discharge (subglacial meltwater) and from submarine ice front melting (submarine meltwater). By using the $\theta$–$S$ diagram, we can separate mixing processes of these waters.

Subglacial meltwater discharge mixes with the ambient ocean water to form upwelling plume and spreads subsequently. The straight line on the $\theta$–$S$ diagram between the subglacial meltwater ($\theta = \theta_{sg} = 0$°C, $S = S_{sg} = 0$) and ambient ocean water at the conduit depth ($\theta = \theta_e$, $S = S_e$; potential temperature and salinity at the 210 m depth that averaged for all observation sites in each year; hereinafter, referred to as "entrained fjord water") is called Runoff-slope (Mortensen et al., 2013; Straneo et al., 2011, 2012).

At ice front, submarine melting of the ice is driven by the heat of ambient sea water. The straight line on the $\theta$–$S$ diagram that indicates the mixing caused by the submarine melting (Gade, 1979) is often called Gade-slope. We defined an effective potential temperature ($\theta_{mw}$ : °C) by calculating the energy required to melt ice when $S = 0$ (Jenkins, 1999; Straneo et al., 2012; Chauché et al., 2014);

$$\theta_{mw} = \theta_f - \frac{L_f}{c_p} - \frac{c_i(\theta_f - \theta_i)}{c_p} \quad (°C)\,, \tag{3.1}$$

where $\theta_f$ is the pressure-corrected melting point of ice (−0.1°C), $L_f$ is the latent heat of fusion (334.5 kJ kg$^{-1}$), $\theta_i$ is ice temperature (−5°C after Seguinot, et al. (2016)), and $c_i$ and $c_p$ are the specific heat capacities of ice and seawater (2.1 and 3.98 kJ kg$^{-1}$ K$^{-1}$). Thus,

Gade-slope is the line connecting submarine meltwater ($\theta = \theta_{mw} = -86.7$°C、$S = S_{mw} = 0$) and the entrained fjord water.

Assuming that the water properties can be described as a mixture of the three different waters (subglacial meltwater, submarine meltwater and entrained fjord water), fraction of each water component in ocean water can be defined (e.g., Mortensen et al., 2013; Mankoff et al., 2016; Fig. 3.8). The volume fractions of subglacial meltwater ($f_{sg}$), submarine meltwater ($f_{mw}$) and entrained fjord water ($f_e$) are described as follows;

$$f_{sg} + f_{mw} + f_e = 1 \ . \tag{3.2}$$

Sampled potential temperature ($\theta_A$: °C) and salinity ($S_A$) represent the following equations;

$$\theta_A = \theta_{sg} f_{sg} + \theta_{mw} f_{mw} + \theta_e f_e \quad (°C) \ , \tag{3.3}$$

$$S_A = S_{sg} f_{sg} + S_{mw} f_{mw} + S_e f_e \ . \tag{3.4}$$

Because $S_{sg} = 0$ and $S_{mw} = 0$, Equation (3.4) is converted to

$$S_A = S_e f_e \ . \tag{3.5}$$

By using Equations (3.2), (3.3) and (3.5), $f_{sg}$ and $f_{mw}$ are given by the following equations;

$$f_{sg} = \frac{1}{\theta_{sg} - \theta_{mw}} \left( \theta_A - \theta_{mw} \left[ 1 - \frac{S_A}{S_e} \right] - \theta_e \frac{S_A}{S_e} \right), \tag{3.6}$$

$$f_{\mathrm{mw}} = 1 - f_{\mathrm{sg}} - \frac{S_{\mathrm{A}}}{S_{\mathrm{e}}} \ . \tag{3.7}$$

By using Equations (3.6) and (3.7), we can describe the straight lines that represent the fractions of subglacial and submarine meltwater parallel to Gade-slope and Runoff-slope on the $\theta$–$S$ diagram, respectively. In the $\theta$–$S$ space which is consisted of the positive fraction of each component (hereinafter, referred to as "meltwater quadrant"), water mass properties can be explained as the mixture of three component. Note that water mass properties outside of meltwater quadrant are the results of some other mixing processes and the above mentioned calculation is not applicable.

### 3.2.3.2. Freshwater fraction in $\theta$–$S$ diagram

As shown in section 3.2.2, there were some differences in the vertical distribution of $\theta$–$S$ properties between 2014 and 2016. To understand the interannual difference in mixing process controlling the water properties, we estimated the freshwater fractions in the $\theta$–$S$ diagram. Here, we compare the common site nearest to the ice front (St. 14D1 and St. 16D3; approximately 4 km from the ice front) where the turbidity difference is significant, and examine the interannual difference in freshwater fractions. For the other stations, the results were similar.

First we examine the characteristics of water properties for the depths from 210 m to the PW core (~150 m). $\theta$–$S$ properties followed the Gade-slope near the 210 m depth in both 2014 and 2016 (Black lines in Fig. 3.9a and b). However, near the PW core, the properties deviated slightly from the Gade-slope and located outside of the meltwater quadrant, which implies the influence of PW.

The situation changed further above the PW core (80–150 m). In 2014, $\theta$–$S$ properties exactly aligned along the Gade-slope from 100 m to 80 m (local $\theta_{min}$) (black dotted lines in Figs 3.9a and c). Submarine meltwater fraction at the local $\theta_{min}$ was 1.6%, which was the largest fraction indicating the greatest influence of submarine melting among all depths. The subglacial meltwater fraction was insignificant. In 2016, on the other hand, $\theta$–$S$ properties revealed those of seasonal pycnocline above the PW core, and the submarine meltwater fraction decreased to less than 0.5% (Figs 3.9b and d). The subglacial meltwater fraction was less than 1.1%.

At the depth of 50–80 m above the local $\theta_{min}$ in 2014, the sea water consisted of 1.3–1.6% of submarine meltwater, 0.1–1.4% of subglacial meltwater, and 97.3–98.3% of entrained fjord water (Figs 3.9a and c). The fraction reflects the substantial influence of submarine meltwater in this year. In 2016, the $\theta$–$S$ data located outside of the meltwater quadrant, which implies that the ocean water properties cannot be explained by the simple mixing of the three water components (Figs 3.9b and d). Near the local $\theta_{max}$ around 60 m, turbidity was significantly lower in 2016 compared to that in 2014, which implies weaker influence of subglacial meltwater.

At the depth of 15–40 m where the highest turbidity was observed, subglacial meltwater fraction was high; its maximum was found around 15 m (Figs 3.9c and d). In 2014, sea water consisted of 2.5–6.0% subglacial meltwater, 0.4–1.1% submarine meltwater and 93.6–96.3% entrained fjord water (Figs 3.9a and c). Although submarine meltwater fraction decreased as the depth was shallower in this layer, the rapid increase in temperature in $\theta$–$S$ diagram can reflect the influence of development of seasonal pycnocline. Thus, this apparent decrease in submarine meltwater fraction can occur under the influence of development of seasonal pycnocline. In 2016, water was the mixture of

approximately 2.4–4.0% subglacial meltwater and 96.0–97.6% entrained fjord water (no submarine meltwater) (Figs 3.9b and d). Subglacial meltwater fraction was greater in 2014 than in 2016 by up to 2.0%. The magnitude of the yearly variations reached to 50% of the absolute fraction.

Near the surface at 5–15 m depth immediately above the most turbid water layer, $\theta$–$S$ properties were found outside of meltwater quadrant for both years. The $\theta$–$S$ properties in 2014 deviated toward significantly high temperature and low salinity above the Runoff-slope (Figs 3.9a and c). The $\theta$–$S$ properties in 2016 showed a similar tendency as that in 2014, but the deviation from the Runoff-slope was smaller (Figs 3.9b and d). Hence, water at the depth of 5–15 m might be influenced by subglacial meltwater more strongly in 2016 than in 2014, although it is difficult to quantify as this layer was outside of meltwater quadrant (Figs 3.2 and 3.9). Turbidity at this depth was also higher in 2016 than in 2014, which supports more significant influence of subglacial meltwater in 2016.

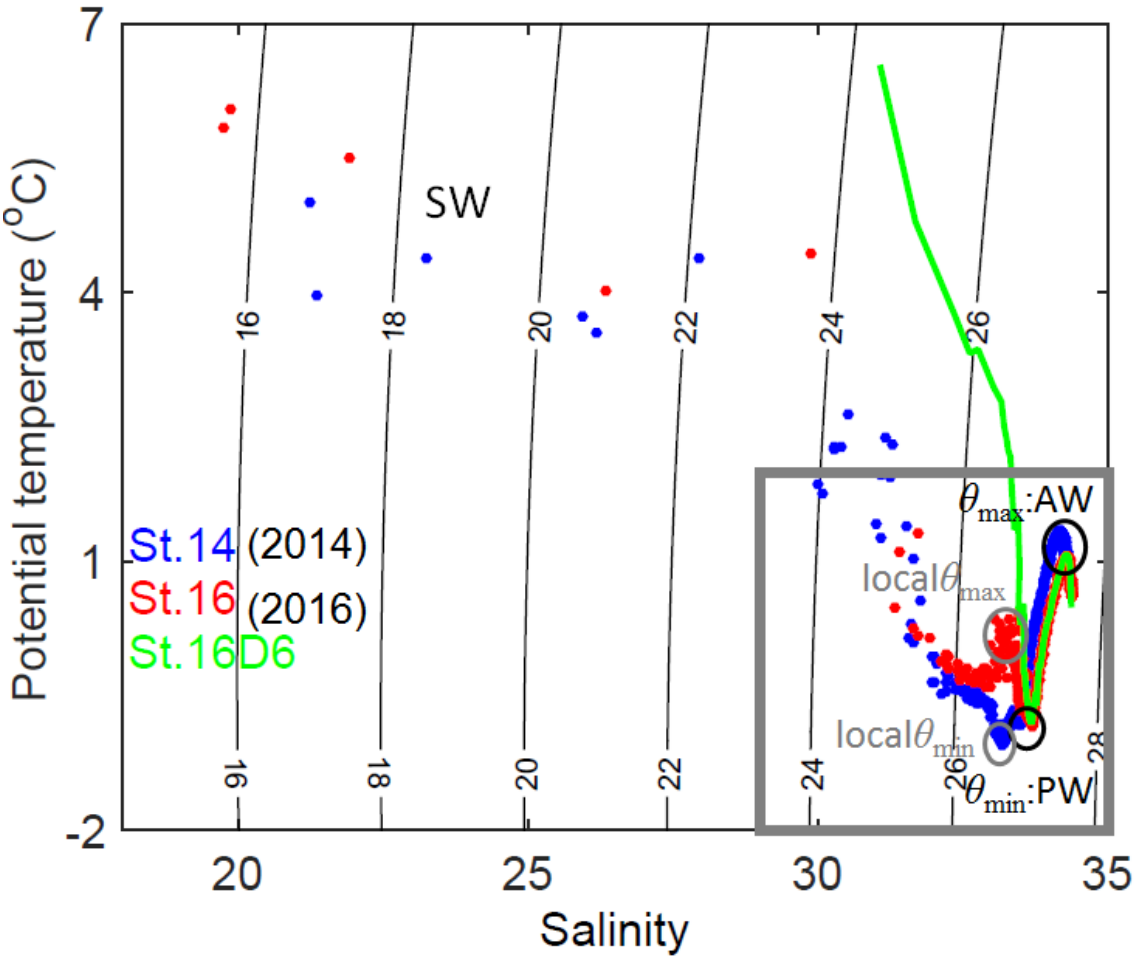


Fig. 3.2. Potential temperature-salinity diagram in 2014 and 2016. Dots are shown in five meter intervals. The color of the markers corresponds to the sampling sites as shown in Fig. 3.1b. Potential densities are shown by the black isopycnal contours. The grey box indicates the domain shown in Figs 3.8 and 3.9.

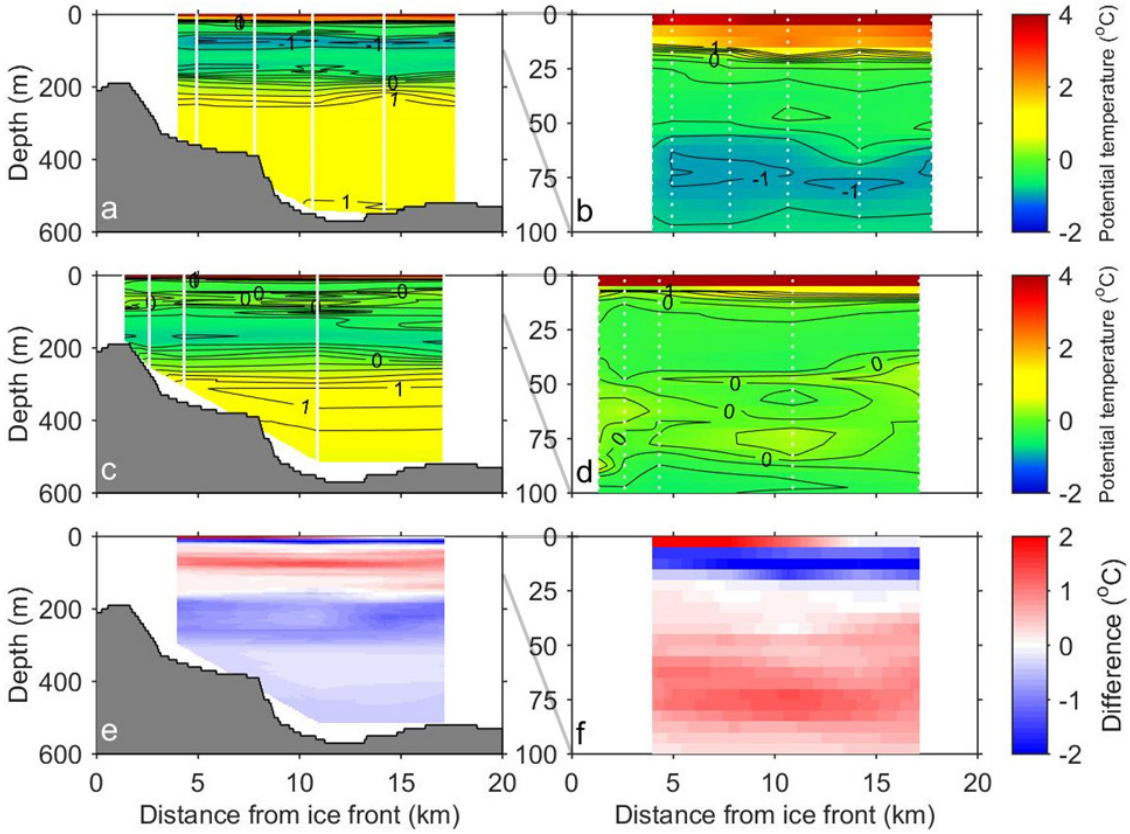


Fig. 3.3. Potential temperature along the centerline of Bowdoin Fjord as observed in (a) 2014, (c) 2016, and (e) temperature difference between the two years (2016–2014). (b), (d), and (f) show the region from the sea surface to 100 m deep.

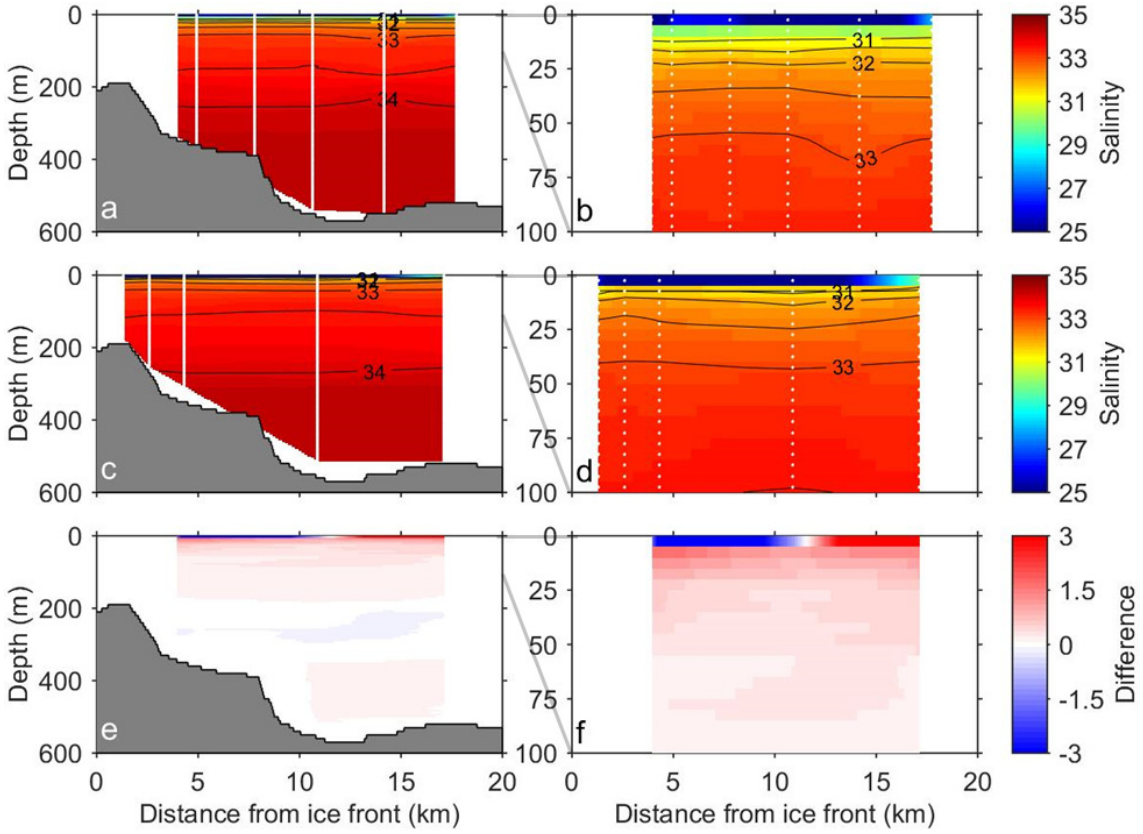


Fig. 3.4. Same as Fig. 3.3, but for salinity.

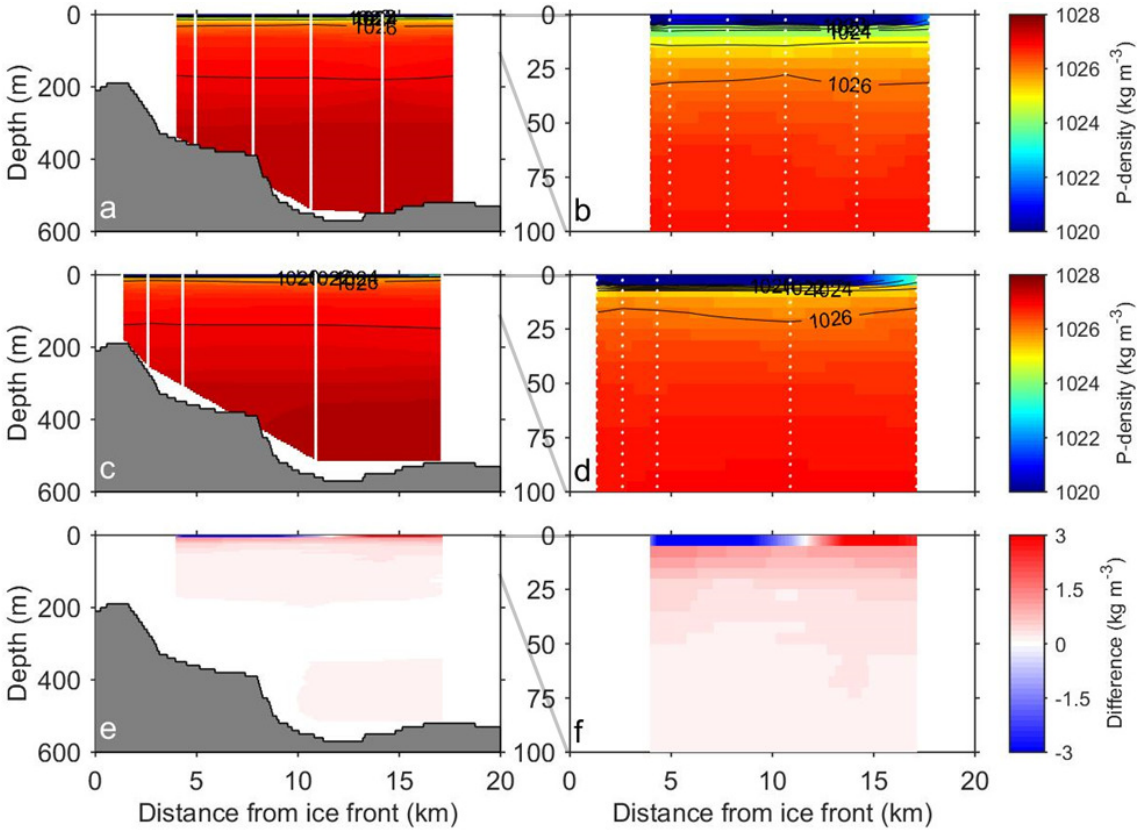


Fig. 3.5. Same as Fig. 3.3, but for potential density.

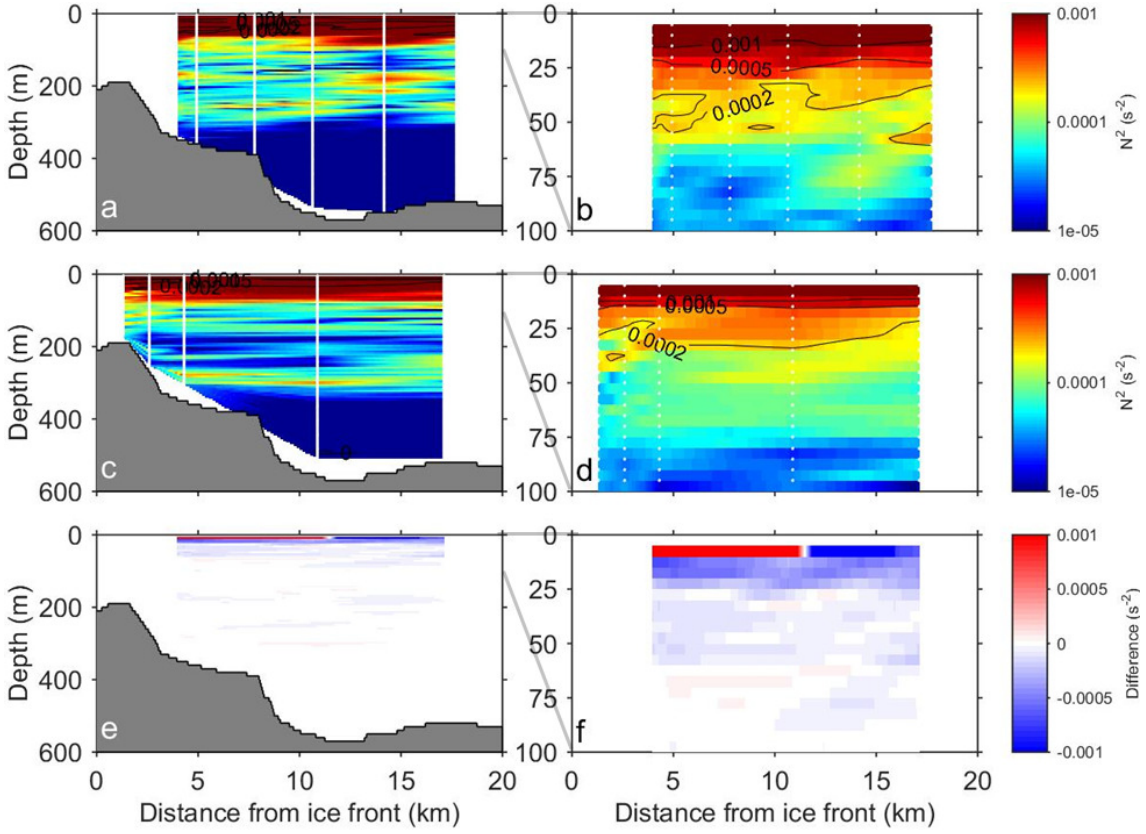


Fig. 3.6. Same as Fig. 3.3, but for square of Brunt-Väisälä frequency ($N^2$).

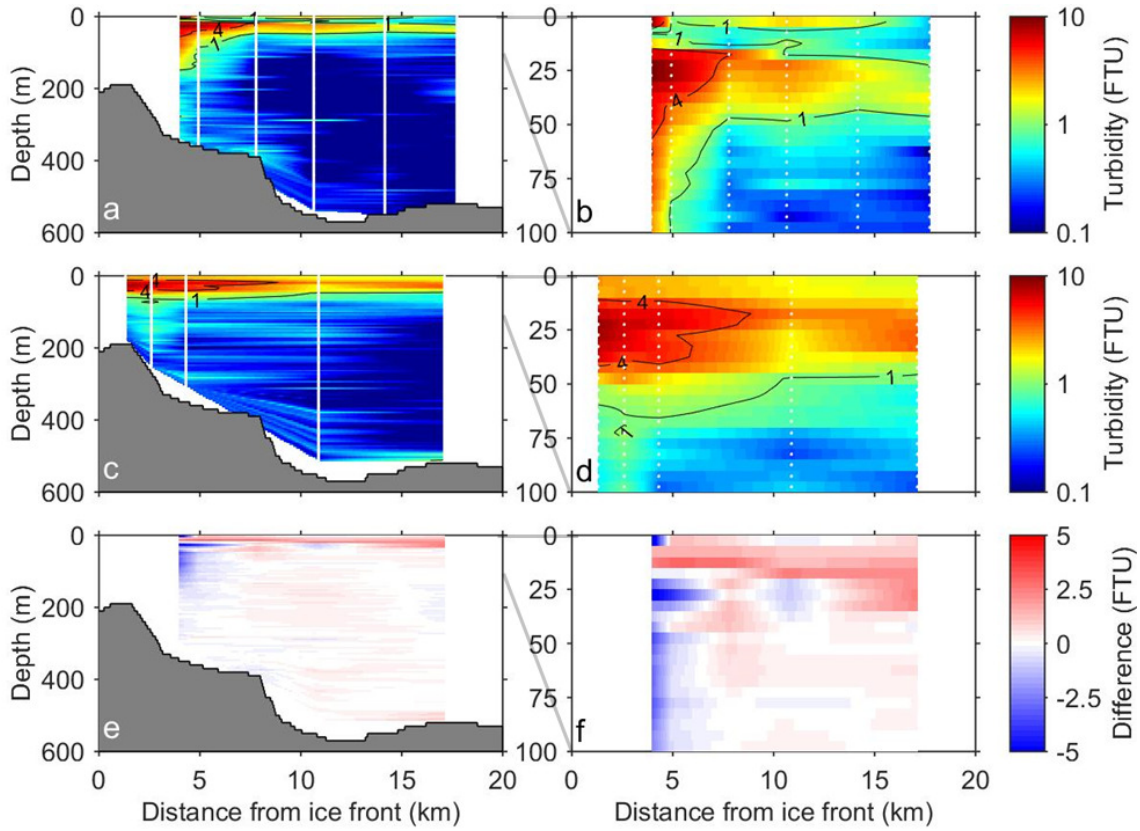


Fig. 3.7. Same as Fig. 3.3, but for turbidity.

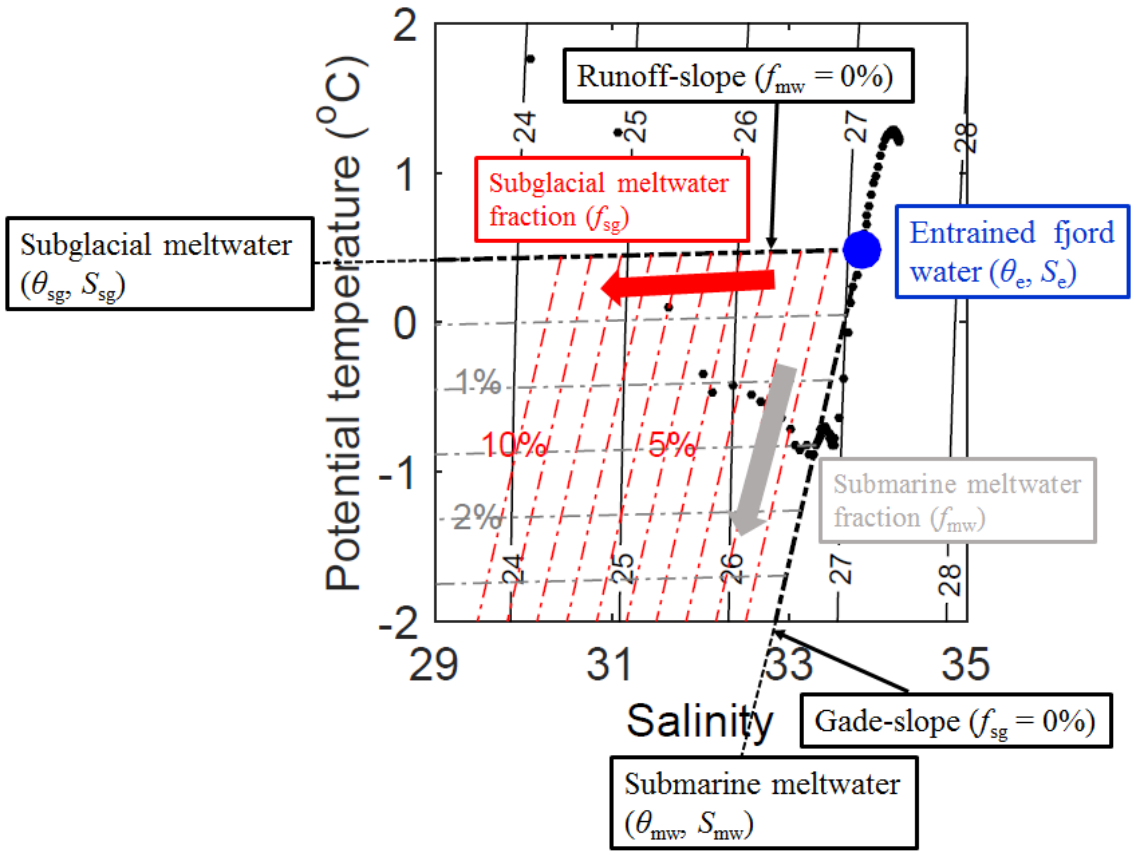


Fig. 3.8. Freshwater endmember analysis in the potential temperature-salinity diagram. Black dots show the data observed at depth ≥ 5 m of St. 14D1.

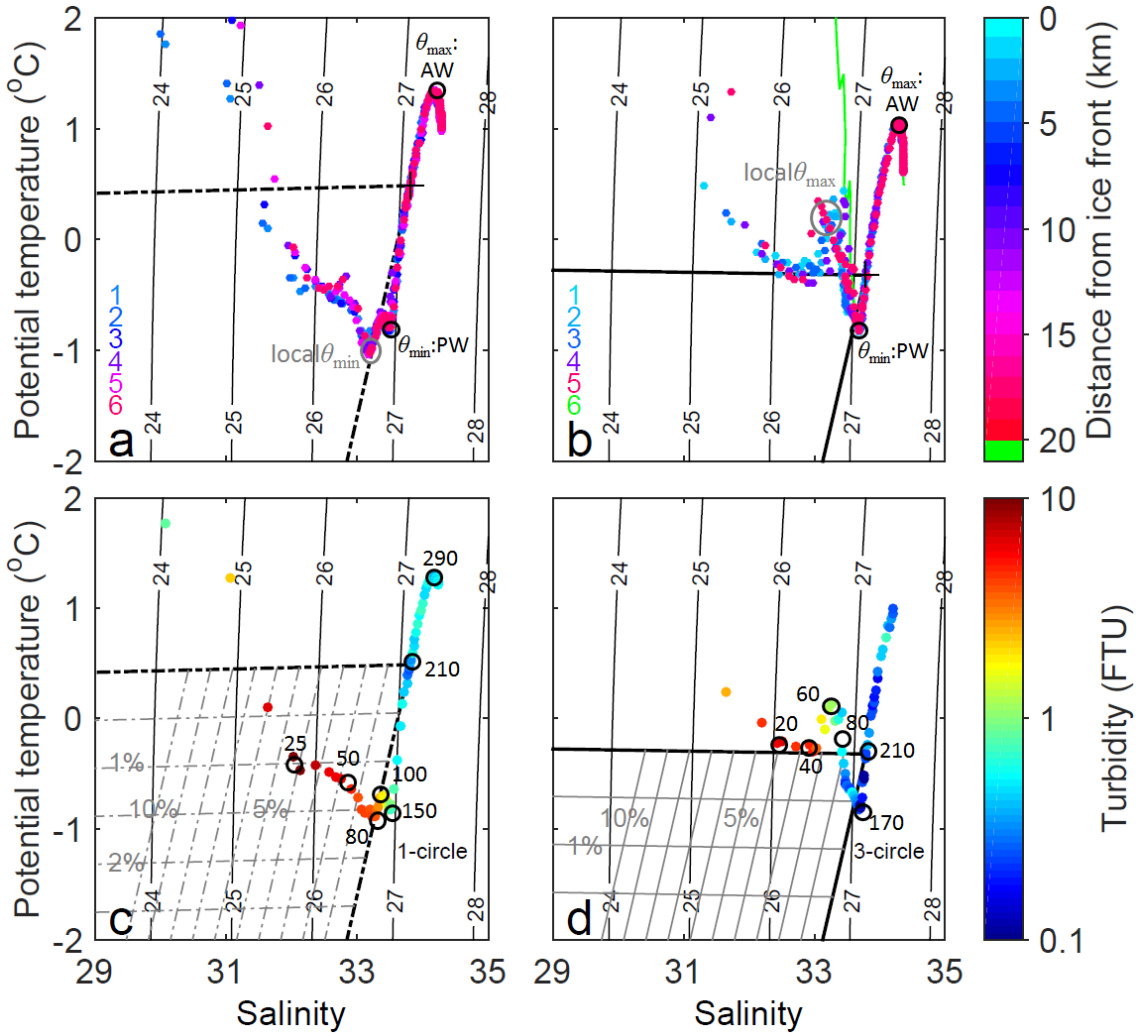


Fig. 3.9. Potential temperature-salinity diagrams with the freshwater endmember fractions. (a, c) in 2014 and (b, d) in 2016 (shown in the grey box in Fig. 3.2). Black lines represent the theoretical Gade-slope and Runoff-slope. In (a) and (b), the data are from the sampling stations 1–6, and the color scale used for the markers indicates the distance from the ice front to the sampling stations. In (c) and (d), the data in (a) and (b) were taken from stations ~4 km distance from the ice front; from St. 14D1 at depth ≥ 5 m and St. 16D3 at depth ≥ 5 m, respectively. In (c) and (d), the color of markers denotes turbidity. Grey lines represent fractions of subglacial meltwater (line intervals are 1% to 10%) and submarine meltwater (line intervals are 0.5% to 2.5%). Black number indicates the depth.

## 3.3. Numerical model experiment

### 3.3.1. Numerical model and modeling settings

We employ a numerical model to quantitatively investigate the distribution of subglacial meltwater under the influence of changing amount of glacier discharge and realistic fjord stratifications. A numerical experiment is performed to simulate subglacial meltwater plume in front of BG based on the observed fjord structure (Fig. 3.10). We use a 3-D incompressible non-hydrostatic ocean model with the Boussinesq approximation, originally developed by Matsumura and Hasumi (2008). The model domain represents BF with 3.2 km in width (from east to west; x-direction), 20.5 km in length (from north to south; y-direction), and 600 m in depth (z-direction) (Figs 3.10a and b). Ice front is located at the northern end of the model domain and the fjord mouth is at the southern end. The model resolution is 50 m for the horizontal direction, and 10 m for the vertical direction. Horizontal subgrid-scale viscosity and diffusivity are represented by strain rate–dependent diffusivity (Smagorinsky, 1963) following Matsumura and Hasumi (2010). Vertical viscosity and diffusivity are $1.0 \times 10^{-5}$ $m^2$ $s^{-1}$ and $1.0 \times 10^{-5}$ $m^2$ $s^{-1}$, respectively. Coriolis parameter is set to $1.4 \times 10^{-4}$ $s^{-1}$.

We use a simplified topography of BF as the model bathymetry. Based on the observation along the centerline of the fjord, water depth of the fjord increases from the ice front (210 m) to the mouth of BF (530 m) along the fjord. Across the fjord, water depth decreases from the center (mean depth of 440 m) to the model boundary (mean depth of 260 m) (parabola-shape). (Sugiyama et al., 2015; Figs 3.10a and b). We set a tunnel-like subglacial drainage conduit as approximated by a rectangular cross-section (200 m wide × 50 m high; 10000 $m^2$) at the 210 m depth at the center of fjord.

Initial potential temperature and salinity are set to be horizontally uniform based on the field observations; the stratification in 2014 is taken as a control case (solid lines in Figs 3.10c and d). Subglacial meltwater ($\theta$ = 0°C, $S$ = 0, virtualized tracer concentration = 1) is injected into the model domain from the subglacial drainage conduit at the northern boundary. Outflow velocity is set to preserve mass in the domain with following the vertical profile of predicted velocity at the grid next to the southern boundary. The virtualized tracer is implemented to track the behavior of subglacial meltwater. Tracer concentration is initially zero over the whole domain and assumed to obey the same advection–diffusion equation as potential temperature and salinity. No heat flux and wind stress are applied at the surface.

As basic experiments for qualitative discussion, we studied the effect of the amount of subglacial meltwater discharge ($Q_{sg}$ : $m^3$ $s^{-1}$) by changing the inflow velocity ($v$ : m $s^{-1}$) given at the northern boundary by a factor of ten ($v$ = 0.01, 0.05 and 0.1 m $s^{-1}$; $Q_{sg}$ =100, 500 and 1000 $m^3$ $s^{-1}$; C2014S, C2014 and C2014H). For subsequent quantitative discussion on change in discharge, additional experiment is performed by increasing the amount of discharge from C2014, which is considered as the most consistent with the observed transitional process of subglacial meltwater in the above three cases ($v$ = 0.06 m $s^{-1}$; $Q_{sg}$ = 600 $m^3$ $s^{-1}$; C2014L; see section 3.4.2). The 20% greater amount of discharge given in C2014L is based on the situation that the PDD at Qaanaaq Airport was approximately 20% greater in 2016 than in 2014 (section 3.1).

To assess the influence of the fjord stratification on the distribution of subglacial meltwater, we carry out an experiment with the initial stratification as observed in 2016 (C2016; dashed lines in Figs 3.10c and d). Because $\theta$, $S$ and the virtualized tracer are restored to the initial profile at the southern boundary, the numerical experiment results

until the tracer reaches the southern boundary are basically used; integration time until the tracer reaches the southern boundary is 56 h in C2014S, 16 h in C2014, 13 h in C2014H, 15 h in C2014L and 15 h in C2016, respectively.

### 3.3.2. Results

#### 3.3.2.1. Subglacial meltwater behavior

In the control case (C2014), subglacial meltwater upwells along the ice front and then reaches the fjord surface 1 hour later (Fig. 3.11a). Within 1 km from the ice front, the highest tracer concentration appears with 1–2 km width at the surface (Figs 3.12 and 3.13a–c). Beyond 1 km from the ice front, subglacial meltwater subducts below the surface and spreads offshore at the depth of 20–30 m (Figs 3.11b and c).

In the case with increased discharge (C2014H), subglacial meltwater upwells along the ice front as observed in C2014 (Fig. 3.11d). The tracer with higher concentration than C2014 reaches the surface 1 hour later and covers entire width of the fjord at 4 hours after the injection (Fig. 3.12e). At the distance more than a few kilometers from the ice front, the distribution of subglacial meltwater is approximately the same as that in C2014. However, within a few kilometers from the ice front, the tracer concentration is the highest at the surface (0–10 m depth) over the full width of the fjord, which is in contrast to the subduction observed in C2014 (Figs 3.11e and f).

In the case with reduced discharge (C2014S), subglacial meltwater upwells along the ice front but not to the surface (Fig. 3.11g). Tracer concentration is higher at the depth of 20–30 m than at the surface, but the vertical contrast is weak (Figs 3.11–13g–i). These results indicate that the subglacial meltwater plume cannot obtain enough buoyancy to

reach the surface, which is significantly different from those in C2014 and C2014H. Tracer concentration at the depth of 20–30 m, where the highest concentration is observed, is lower than those in C2014 and C2014H.

In all the cases (C2014, C2014H and C2014S), subglacial meltwater spreads horizontally within several hours after the injection (Figs 3.12 and 3.13). As time proceeds, the meltwater gradually leans to the right side of the fjord coast due to the influence of Coriolis force. Basically, the time evolution of tracer along the centerline is the same as that on the right side after a little time lag. The depth of maximum concentration of subglacial meltwater tracer is dependent on the magnitude of the discharge, so that the meltwater distributes nearer the surface when the discharge is larger. Note that these results represent the transitional process until reaching the southern boundary of model domain, not a long-term behavior of subglacial meltwater.

#### 3.3.2.2. Impacts of changes in the amount of subglacial discharge and fjord stratification

Based on the control case (C2014), we investigate the effects of the 20% increase in subglacial discharge (C2014L) and the different initial stratification as observed in 2016 (C2016). When we compare the result in C2014 with those in C2014L and in C2016, the results after 15 hours are used to consider the integration time that virtualized tracer reaches the southern boundary in earlier case (section 3.3.1).

In the increased discharge of C2014L, concentration of subglacial meltwater tracer at the depth of 0–40 m increases by 10–40% (Figs 3.14a and c). Only in the vicinity of glacier, the tracer concentration at the depth of 50–100 m decreases by 20–40%. This

result shows that subglacial meltwater shift to the shallower layer as the amount of subglacial discharge increases, which is consistent with the result shown in section 3.3.2.1.

For the stratification in 2016 (C2016), concentration of subglacial meltwater tracer at the depth of 0–10 m increases by up to 40% (Figs 3.14b and d), whereas the tracer concentration decreases at the depth deeper than 20 m. In particular at the depth of 50–100 m in the vicinity of glacier, decreasing rate of tracer concentration is high (uniformly 40%). The stratification in C2014 at the subsurface and below is stronger than that in C2016, whereas that near the surface is weaker. After reaching the surface, the plume in C2016 is less likely to submerge and advect near the surface with higher concentrations than that in C2014.

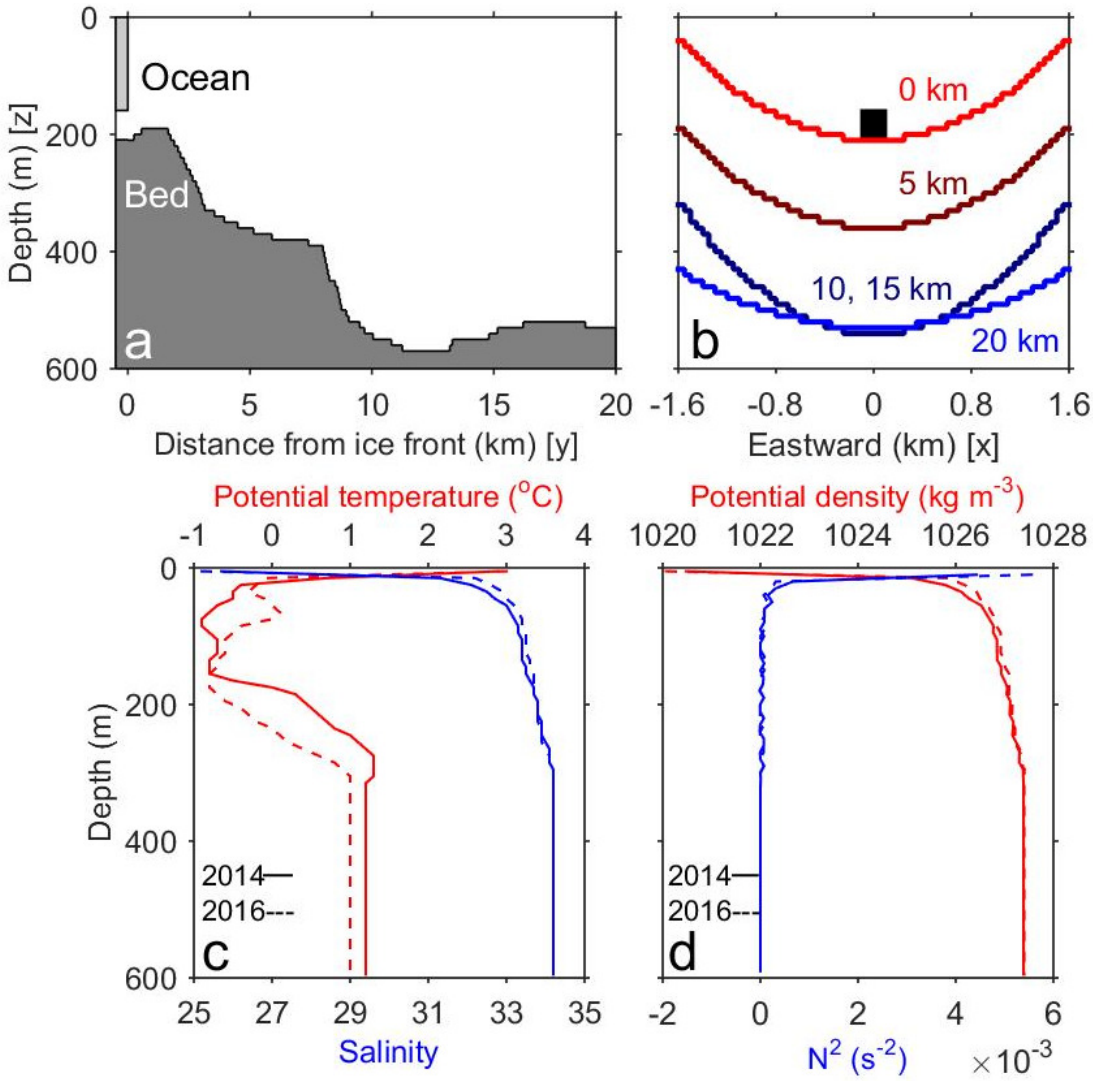


Fig. 3.10. Numerical model settings. (a) Ocean depth along the centerline of Bowdoin Fjord (from north to south). The space between the glacier and the bed indicates a 50 m high subglacial drainage conduit. (b) Depth across the fjord (from west to east) at 0, 5, 10, 15 and 20 km from the ice front. The box indicates the subglacial drainage conduit at the center of fjord (200 m wide × 50 m high; 10000 $m^2$). Initial vertical profiles of (c) potential temperature, and salinity, and (d) potential density, and square of Brunt-Väisälä frequency ($N^2$) computed from (c).

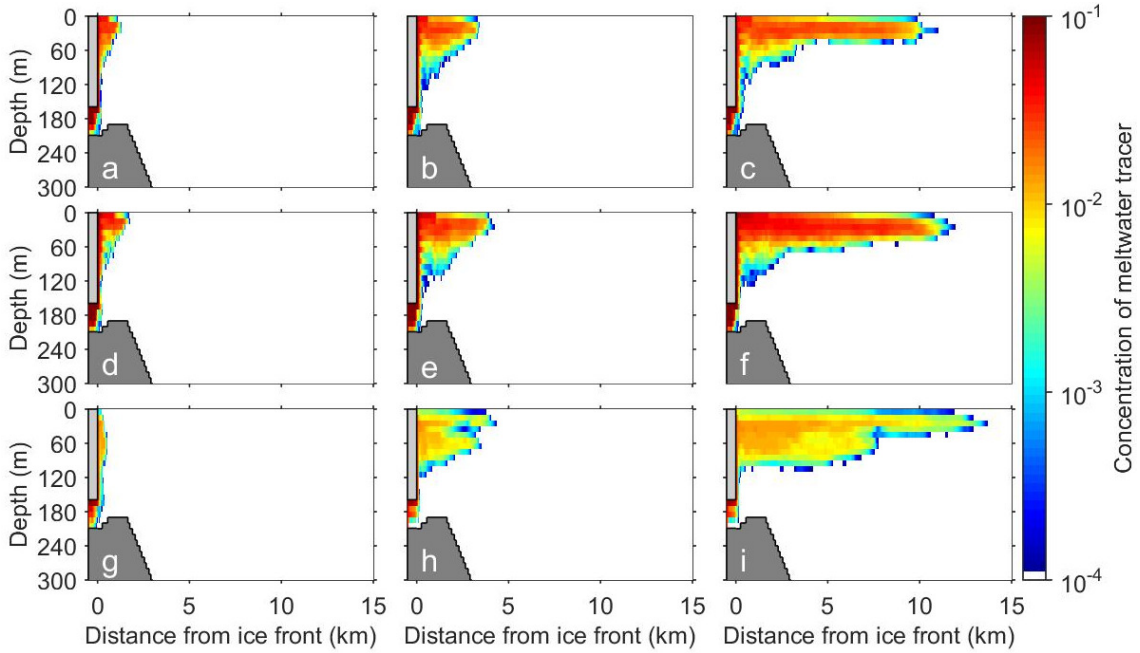


Fig. 3.11. Time series of subglacial meltwater tracer concentration within the vertical cross section along the centerline of fjord. (a), (b) and (c) are the results computed with control discharge (C2014; $Q_{sg}$ = 500 $m^3$ $s^{-1}$) after the integration of 1, 5 and 15 hours, respectively. (d), (e) and (f) are with increased discharge (C2014H; $Q_{sg}$ = 1000 $m^3$ $s^{-1}$) after the integration of 1, 4 and 13 hours, respectively. (g), (h) and (i) are with reduced discharge (C2014S; $Q_{sg}$ = 100 $m^3$ $s^{-1}$) after the integration of 1, 15 and 56 hours, respectively.

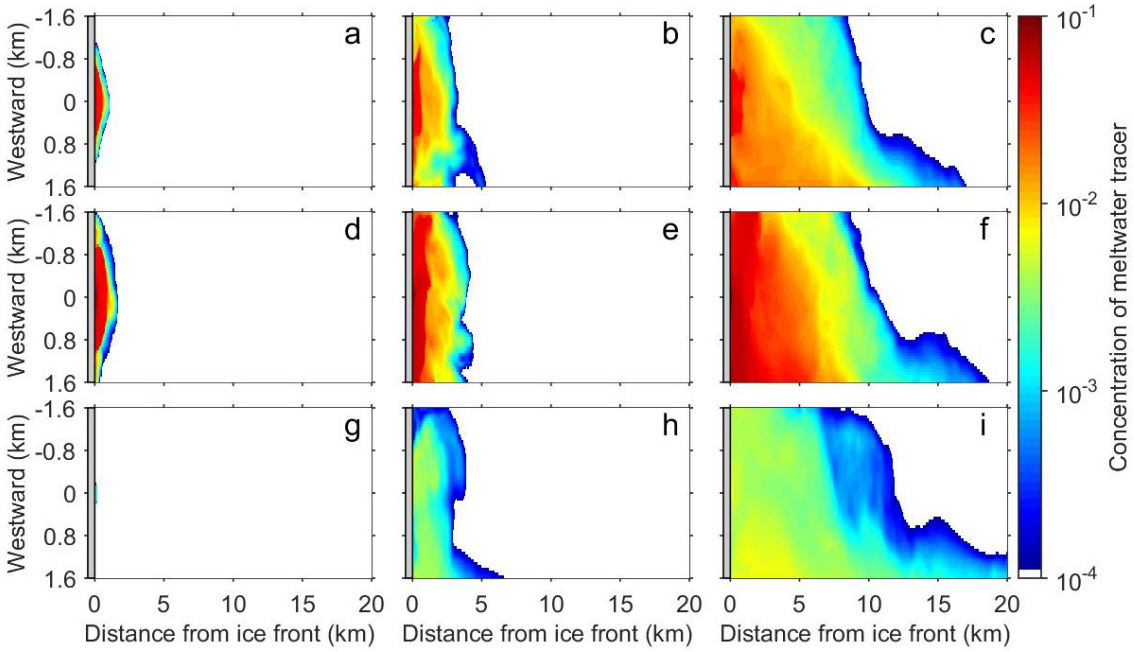


Fig. 3.12. Time series of horizontal distribution of subglacial meltwater tracer concentration at the fjord surface (0–10 m depth). The numerical settings and integral time are the same as Fig. 3.11.

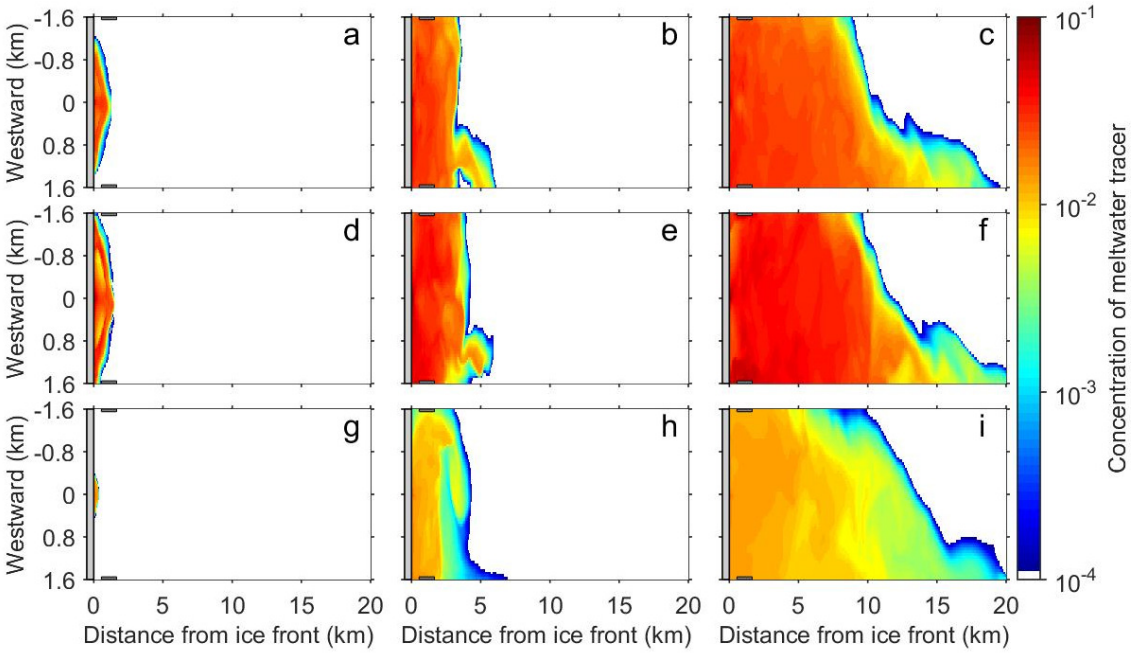


Fig. 3.13. Time series of horizontal distribution of subglacial meltwater tracer concentration at the 20–30 m depth. The numerical settings and integral time are the same as Fig. 3.11.

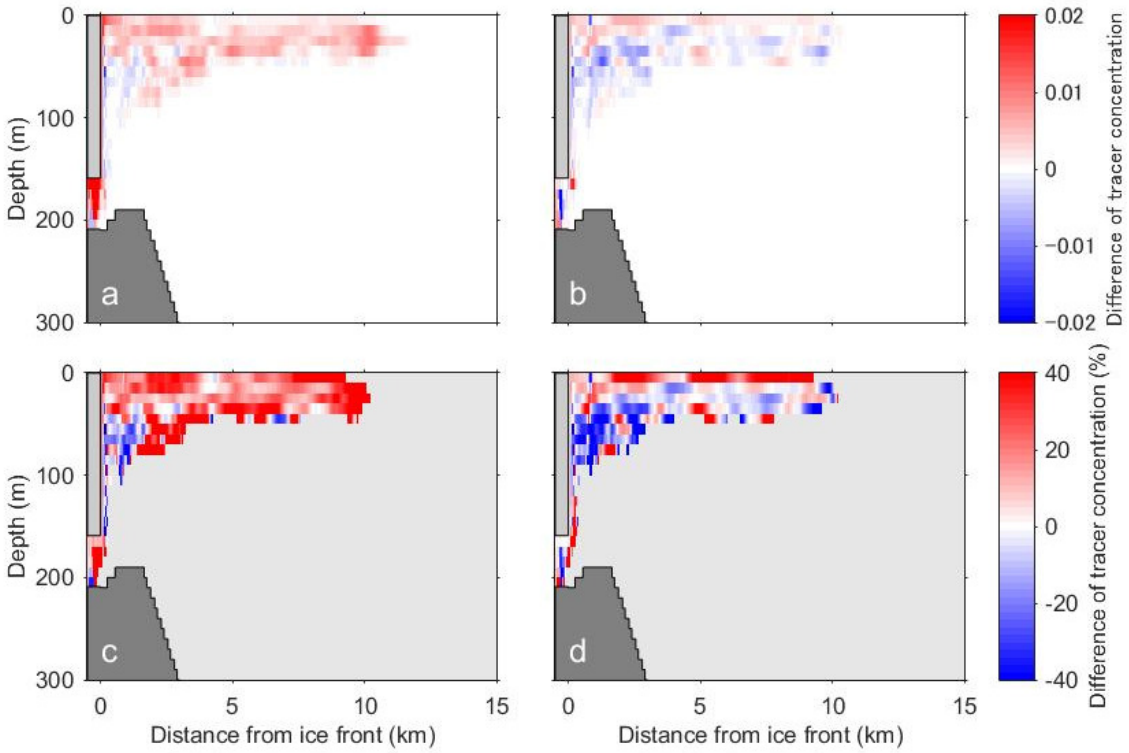


Fig. 3.14. (a) Difference between subglacial meltwater tracer concentrations computed with C2014L ($Q_{sg}$ = 600 $m^3$ $s^{-1}$) and C2014 ($Q_{sg}$ = 500 $m^3$ $s^{-1}$) using the same initial stratification condition. The difference (C2014L−C2014) after integration of 15 hour is shown within the cross section along the centerline of the fjord. (b) Difference between the results computed with the same amount of discharge, but using initial stratifications as observed in 2016 and 2014 (C2016−C2014 is shown). (c) and (d) show the same data in %.

## 3.4. Discussion

### 3.4.1. Quantitative relationship between subglacial meltwater fraction and turbidity

In section 3.2.3.2, qualitative agreement is shown between the turbidity and subglacial meltwater fraction near the ice front. Here, we assess the quantitative relationship between the turbidity and subglacial meltwater fraction in each year. In 2014, the relationship between subglacial meltwater fraction ($R_{sg}$: %) and the turbidity (T: FTU) in the meltwater quadrant is expressed as $R_{sg} = T \times 0.7 - 2.0$ ($R^2 = 0.67$; Fig. 3.15a). In 2016, the data in meltwater quadrant and that including the data points close to the Runoff-slope (the depth of 15–40 m) showed a linear relationship of $R_{sg} = T \times 0.6 + 0.3$ ($R^2 = 0.94$), whose inclination is similar to that in 2014 (Fig. 3.15b). Moreover, the result of low turbidity at local $\theta_{max}$ (the depth of 60 m) in 2016 is consistent with the calculation that the fraction of subglacial meltwater is small in this layer (Fig. 3.9d). These results indicate that the vertical distribution of turbidity can reflect that of the fraction of subglacial meltwater near the ice front (Fig. 3.7). Recent observations in other regions in Greenland qualitatively showed that highly turbid subsurface layer corresponds to the distribution of subglacial meltwater (Chauché et al., 2014; Stevens et al., 2016). The quantitative relationship between turbidity and subglacial meltwater fraction in this study reveals that the turbidity measurement is an effective tool to investigate the distribution of subglacial discharge into fjords as well as the analysis based on the heat and freshwater as shown in Fig. 3.9.

However, the intercept of the linear regressions differed between 2014 and 2016. The turbidity value of entrained fjord water (at the 210 m depth), that is not likely influenced

by turbid subglacial meltwater, was different in two years (0.6 FTU at St. 14D1, 0.3 FTU at St. 16D3) (Figs 3.7 and 3.9). Therefore, there is a possibility that suspended sediment concentrations of subglacial meltwater and entrained fjord water differ from year to year. For a more universal agreement, continuous measurements on interannual variation in the turbidity distribution are required to establish more general formulation of the relationship between turbidity and subglacial discharge.

### 3.4.2. Validity of subglacial meltwater behavior in the numerical experiment

In our basic numerical experiments, the regime of time evolution of subglacial meltwater is dependent on the amount of subglacial discharge. Although it is difficult to precisely estimate its amount, we discuss the validity of the regime of subglacial meltwater behavior obtained from the numerical experiment by comparing with the observational data and condition.

Before and after our observation dates in 2014 and 2016, turbid surface plumes with a diameter of a few hundred meters were visible just in front of BG. Additionally, at more than about 1 km from the ice front, our data in both years show that the highest subglacial meltwater fractions were observed not at the fjord surface but at the subsurface (Figs 3.7 and 3.9). Judging from the situations, it is reasonable to assume that subglacial meltwater reaches the surface near the ice front and then submerge to the subsurface layer before it spreads offshore. The results of the numerical experiments C2014 and C2014H agree with the observations that plume can reach the fjord surface in the vicinity of the glacier (Figs 3.11–13). This is consistent with the previous studies, which show that subglacial meltwater extends at relatively shallower depth during a large amount of discharge

(Chauché et al., 2014; Jenkins, 2011; Straneo and Cenedese, 2015; Stevens et al., 2016). In the two experiments, the surface plume area at the surface in C2014H is significantly broader than the turbid area observed in the field. Therefore, the result in C2014 ($Q_{sg}$ = 500 $m^3$ $s^{-1}$) is selected as the most appropriate as the realistic subglacial meltwater regime in BF.

### 3.4.3. Factors controlling observed subglacial meltwater distribution

In section 3.3.2.2, our experiments demonstrated that the spread of subglacial meltwater into the fjord can be influenced by change in the amount of subglacial meltwater discharge and difference in fjord stratification. To test whether the two factors explain the difference in the observed subglacial meltwater distribution in 2014 and 2016, we compare the numerical model results with the observational data.

Near the fjord surface (5–15 m depth), turbidity was higher in 2016 than in 2014. In the numerical experiment with 20% larger discharge, concentration of subglacial meltwater near the surface (0–20 m depth) increases by 10–40%. This result is consistent with the turbidity difference observed between the two years (Figs 3.14a and c). These results suggest that turbid subglacial meltwater further extends near the fjord surface in 2016 because the smaller dilution effect of ambient fjord water on subglacial meltwater is exerted by the 20% larger discharge. Chauché et al. (2014) proposed a relationship between $\theta$–$S$ properties of fjord water and the amount of subglacial discharge based on glacier surface melt estimation using a positive degree-day/melt-rate model (Box, 2013). They studied the water properties in the fjord by changing the 50–100% amount of subglacial meltwater discharge. Our study shows that 20% change in the subglacial meltwater discharge causes about 10–40% change in the subglacial meltwater fraction

near the surface. In the numerical experiment with the initial stratification in 2016, tracer concentration increased at the 0–10 m depth and decreased at the 10–20 m depth from that in 2014 (Figs 3.14b and d). Although the near-surface increase is in favour of observed change, the mean increased amount of tracer concentration is smaller than that of discharge increase. Therefore, the distribution of subglacial meltwater near the surface can be affected by change in the amount of subglacial discharge.

As mentioned above, the distribution of subglacial meltwater near the surface is influenced by the amount of subglacial discharge. Highly turbid glacial meltwater is expected to spread over a larger surface area when the amount of subglacial discharge is large, which is consistent with remote sensing data analyses performed off the coast of northwestern Greenland where a number of glaciers terminate in the ocean (Ohashi et al., 2016). Furthermore, a 20% increase in the meltwater discharge results in greater concentration of meltwater not only at the surface but also at the subsurface (20–40 m depth). The magnitude of the change is similar between the surface and the subsurface layers (a few tens %) (Figs 3.14a and c). This result implies the need for considering the vertical distribution of subglacial meltwater at the subsurface in addition to the satellite surface measurements to quantitatively assess the overall impact of subglacial discharge.

In contrast to the observation near the surface, the fraction of turbid subglacial meltwater at subsurface (15–40 m) is greater in 2014 than in 2016 (Figs 3.7 and 3.9). This field observation is inconsistent with the numerical experiments of discharge difference, showing a smaller meltwater concentration at 20–40 m depth under a smaller amount of discharge (Figs 3.14a and c). From the stratification change experiment, tracer concentration at the subsurface is larger by about 10–20% in 2014 stratification (C2014) than in 2016 stratification (C2016) (Figs 3.14b and d). This model result is consistent

with the observed difference at subsurface, and the change rate is quantitatively consistent (a few tens %) (Figs 3.7 and 3.9). Thus, different stratification is a likely reason of the observed difference in subglacial meltwater fraction at the subsurface.

Previous studies showed that strong subsurface stratification in the fjord prohibits upwelling of subglacial meltwater plume and results in spreading of the meltwater into a subsurface layer (Carroll et al., 2015). In addition, plumes extend further over the fjord surface under weaker stratification (Carroll et al., 2015). In the regime that plume reaches the fjord surface, our model study suggests that strong surface stratification prohibits the subduction of the outcropped plume and it is hence likely that plume extends at the fjord surface.

### 3.4.4. Interannual difference in the formation process of stratified structure

The fjord stratification in 2014 and in 2016 were different at the depth deeper than 60–80 m, which can be attributed to the influence of submarine melting and seasonal pycnocline. In this section, we discuss the formation process of the stratified structure for each year.

In 2014, a warm layer attributed to AW was in contact with the ice front, which could enhance the fraction of submarine meltwater at the depth of 80 m (Figs 3.2, 3.9a and c). Because submarine meltwater fraction was detected regardless of the distance from ice front of BG, submarine meltwater from other glaciers in IB might have influenced the water in BF. A warm layer above 210 m extended further up to the shallower layer in 2014 than in 2016. Available excess heat by up to 0.9$^{o}$C is 1.6 times greater in 2014 than in 2016 when calculated by the difference from the freezing temperature (Fig. 3.9). Previous model studies indicate that the rate of submarine melting increased as the water

temperature increased (Xu et al., 2012; 2013). Porter et al. (2014) reveals that the rates of ice mass loss of Tracy and Heilprin Glaciers, neighboring tidewater glaciers in IB, were largely different 1.63 and 0.53 Gt $a^{-1}$, respectively. Since the water depth at the ice front of Tracy Glacier is deeper than that of Heilprin Glacier, the ice front has wider contact with warm AW, suggesting the larger glacier mass loss associated with the larger submarine melting (Porter et al., 2014). Our study suggests that the interannual difference in structure of deep heat storage can change the development of submarine melting layer and hence affect the ice mass loss from Greenland glaciers.

In 2016, a simple seasonal pycnocline detected outside of BF can have large spatial scale (Figs 3.2, 3.9b and d). In our study area (Qaanaaq Airport; blue circle in Fig. 3.1a), mean temperature during the previous winter (December–February) was lower in 2016 than in 2014 by 1.1°C. Thus, the winter vertical mixing was more intense and the mixed layer depth could deepen during the winter in 2016. By contrast, the PDD in summer was higher in 2016 than in 2014. Thus, during the summer in 2016, seasonal pycnocline can develop above the remnant of winter mixed layer. In addition, PW core in BF is deeper in 2016, supporting the possibility of development of seasonal pycnocline influenced by the enhancement of the winter vertical mixing. We thus conjectured that the development of seasonal pycnocline over the large area in 2016 is due to the enhancement of the winter vertical mixing. The deep cold layer prevent the submarine melting and preserve the seasonal pycnocline.

At the depth shallower than 60–80 m where subglacial meltwater spreads, the fjord stratification is modified by the subglacial discharge. In general, the fjord stratification is expected to be stronger after subglacial meltwater discharges into fjord than before, because the density difference is generated between the layers with largely affected and

less affected by subglacial meltwater.

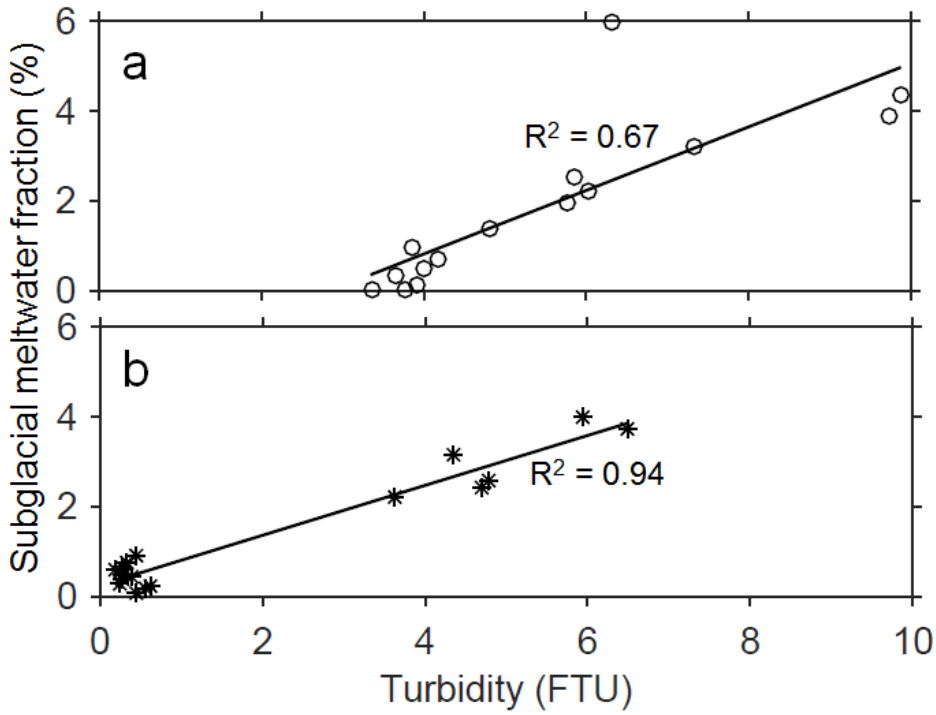


Fig. 3.15. Scatter plots of turbidity and subglacial meltwater fraction at (a) St. 14D1 (Fig. 3.9c) and (b) St. 16D3 (Fig. 3.9d). Solid lines show linear regression of the data.

## 3.5. Summary

With a focus on the interannual variabilities in the subglacial meltwater distribution and ambient water properties, water mass structures in BF in northwestern Greenland were investigated by the ocean observations in two years and the numerical model experiment based on the observation data.

Differences in the distribution of subglacial meltwater and water mass structure between 2014 and 2016 are summarized in Fig. 3.16. The locations of temperature minimum and maximum were different in two years. Local $\theta_{min}$ were observed around 80

m in 2014 and local $\theta_{max}$ around 60 m in 2016, respectively. From analysis of the $\theta$-$S$ properties, these local $\theta_{min}$ and local $\theta_{max}$ can be influenced by the development of submarine melting layer and seasonal pycnocline, respectively.

Subglacial meltwater spread at the depth shallower than local $\theta_{min}$ and local $\theta_{max}$. In both 2014 and 2016, fractions of turbid subglacial meltwater were the highest at the subsurface (15–40 m). The maximum fraction near the ice front was ~6.0% in 2014 and ~4.0% in 2016, respectively, and the fraction was greater in 2014 by up to 50%. Near the surface (5–15 m), turbidity was higher in 2016 than in 2014, suggesting the stronger influence of turbid subglacial meltwater in 2016.

To assess the factor controlling the interannual difference in the observed subglacial meltwater distribution, a numerical model experiment is performed to simulate subglacial meltwater plume. The numerical model experiments using the initial stratifications observed in two years suggest that the fractional difference in subglacial meltwater at the subsurface is attributed to the difference in fjord stratification. The numerical model result with 20% larger discharge suggests that the difference near the surface is primarily affected by the increase in discharge.

From surface to subsurface where subglacial meltwater spreads, the fjord stratification varies from year to year depending on the amount of subglacial discharge. At the depth deeper than 60–80 m, the fjord stratification can be determined by the influence of submarine melting and seasonal pycnocline. Because of the thicker warm layer attributed to AW, submarine melting layer can develop in 2014.

Our study suggests that the fjord stratification including AW and PW, together with the amount of subglacial meltwater discharge, can affect the distribution of subglacial meltwater and water structure reflecting its distribution. Given current increase in

meltwater discharge from Greenlandic glaciers, the buoyancy forcing of subglacial meltwater plume and the ambient fjord stratification is expected to change. To fully capture the subglacial meltwater distribution, further continuous observations and numerical modeling are required over the wider area encompassing the northwestern Greenland.

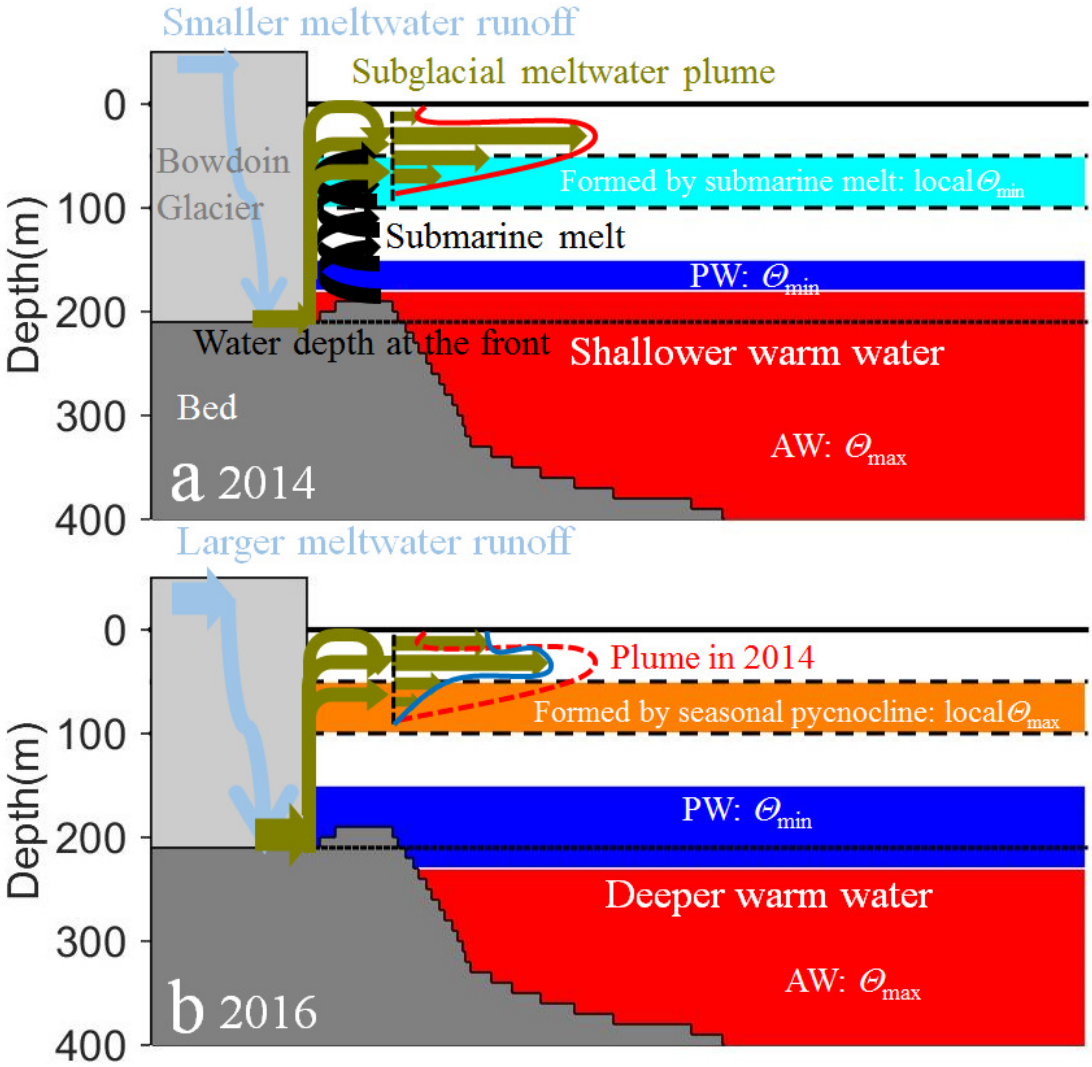


Fig. 3.16. Schematic diagram showing the possible glacial discharge scenario and water mass structure of Bowdoin Fjord in (a) 2014 and (b) 2016.

# Chapter 4

# Behavior of turbid glacial meltwater in Inglefield Bredning fjord system, northwestern Greenland: a case study in 2016

## 4.1. Study area

In Chapter 3, we analyzed the behavior of subglacial meltwater in Bowdoin Fjord (BF). In this chapter, to understand the broader behavior of turbid glacial meltwater and link between the BF and a broader fjord system, we examine the temporal evolution of turbid area from the satellite observation in 2016. The numerical model experiment was used to interpret the dynamics of meltwater after the discharge from glaciers.

As the first step to examine a larger-scale behavior of subglacial meltwater, this study focuses on Inglefield Bredning (IB) fjord system (Fig. 4.1; 77.1–77.8$^{o}$N, 65.5–70$^{o}$W except 77.6–77.8$^{o}$N, 69–70$^{o}$W), including BF, Academy Bugt (AB) and Olrik Fjord (OF), in northwestern Greenland. 11 marine-terminating glaciers flow into IB (No.1–6 glaciers from the northern flank, No.7–8 glaciers from the eastern flank, No.9–11 glaciers from the southern flank), with six of them concentrating on the northeastern corner. The detailed information of glaciers in this study area were shown in sections 2.1 and 3.1.

Detailed bathymetry was not well surveyed in this region. In BF where Bowdoin Glacier (BG) flows into, water depth was measured by echo sounder (Sugiyama et al., 2015). Near the ice fronts of Tracy and Heilprin Glaciers, water depth was estimated by gravity measurements (Porter et al., 2014). These previous measurements revealed that the depths of ice front of Bowdoin, Tracy and Heilprin Glaciers are about 210 m, 610 m and 350 m, respectively. Although bathymetry hasn't been measured elsewhere in a large part of IB, we can use the IBCAO dataset (Jakobsson et al., 2012). The dataset has some

obvious deficiencies; i.e., lack of a small island slightly off the southern coast. Based on this information, the maximum depth of IB is > 900 m.

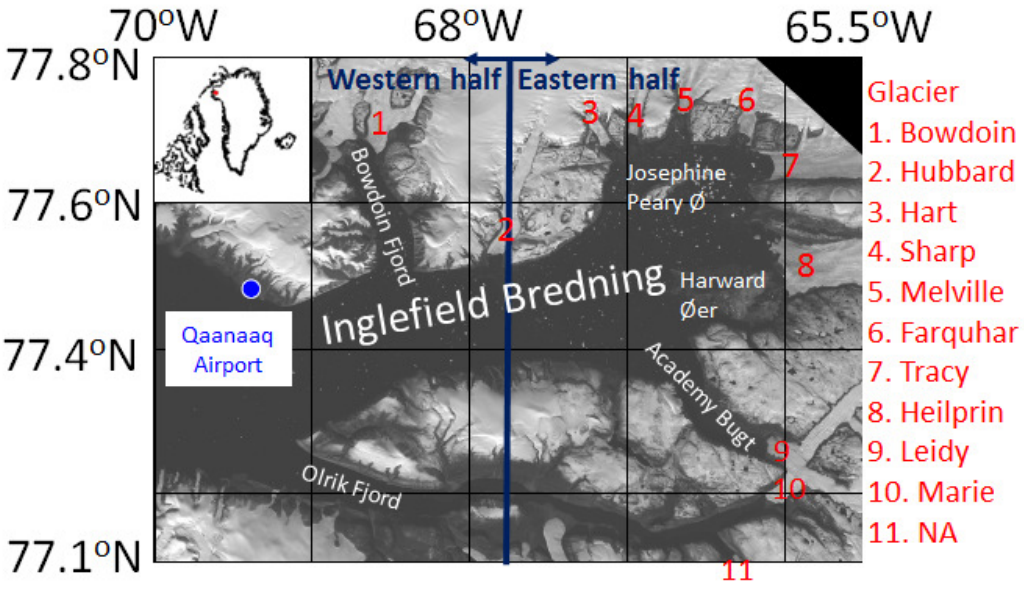


Fig. 4.1. Study region in Inglefield Bredning fjord system in the northwestern Greenland depicted on the Landsat image taken on 6 September 2014. The location of 11 marine-terminating glaciers is indicated by red number. Two relatively large islands are located at the northeastern corner (Josephine Peary Ø; JP) and southeastern corner (Harward Øer; HØ) of the fjord. The inset shows the location of the region in Greenland.

## 4.2. Data and methods

### 4.2.1. Satellite data analyses

To understand the temporal development of the distribution of turbid water in IB system, we used the daily MODIS true color images from June to August in 2016 (downloaded from NASA Earthdata; https://worldview.earthdata.nasa.gov/). To monitor

the temporal change in sea ice condition and the extent of turbid water on open water, we used almost cloud-free 20 MODIS true color images and cloud-cover 1 image on 7 July (to investigate the drift of sea ice floe). Moreover, to quantify the extents of high turbidity water and ice (sea ice and icebergs), Rrs555 datasets were analyzed for the 20 days that almost cloud-free image was obtained. Rrs555 data were obtained from the NASA MODIS on the Aqua multispectral platform. We used the level two data with a spatial resolution of 1 km and temporal resolution of about a few hours, and calculated daily composites. These data products were downloaded from NASA Ocean Color Web (http://oceancolor.gsfc.nasa.gov). Using the same method described in section 2.2, the extent of the high turbidity area was calculated from the number and area of image pixels (1 $km^2$). Because no data are available on the ice, we assumed that the regions of no data correspond to the ice covered area and ice area was calculated from the number and area of image pixels (1 $km^2$).

### 4.2.2. Numerical model experiment

To understand the temporal evolution of behavior of subglacial meltwater, the numerical model experiment is performed. The model used and the settings of viscosity, diffusion and parameter are the same as that in section 3.3. The model domain represents IB fjord system covering 96.5 km from east to west (x-direction), 70 km from north to south (y-direction), and 1000 m in depth (z-direction) (Fig. 4.2). The model resolution is 50 m for the horizontal direction, and 2 m (0–10 m depth), 5 m (10–50 m depth), 10 m (50–700 m depth) and 30 m (700–1000 m depth) for the vertical direction.

Bathymetry in model domain is set based on the observations in BF (No. 1 in Fig. 4.2; Sugiyama et al., 2015) and adjacent to Tracy and Heilprin Glaciers (No. 7 and No. 8 in

Fig. 4.2; Porter et al., 2014). In the other regions, we set the model topography based on the IBCAO dataset.

Initial potential temperature and salinity are set to be horizontally uniform based on the stratification of IB observed in July 2016 (St. 16D6; Fig. 4.3). We use the same method of the subglacial discharge as that in section 3.3. There are 11 glaciers in the IB fjord system, and the depth of subglacial drainage conduit is shown in Table 4.1. Eight glacier do not have direct observation and hence the estimates were set as the same values with BG.

The realistic amount of discharge is not well understood. As a first guess, it is set to be $Q_{sg} = 500\ m^3\ s^{-1}$ for each of 11 glaciers based on the experience on BF, and estimation of the realistic amount of discharge from these glacier is one of the important goals of the fjord system study. To investigate the difference in behavior of subglacial meltwater due to the location of glacier, we categorize 11 glaciers into 6 groups based on the location of glacier and release the virtualize tracer of subglacial meltwater for each group (TRC1–6; Table 4.1). Water outflows from the western boundary of model domain. The integration time is 10 days. The other model settings are the same as those in previous model experiments (section 3.3).

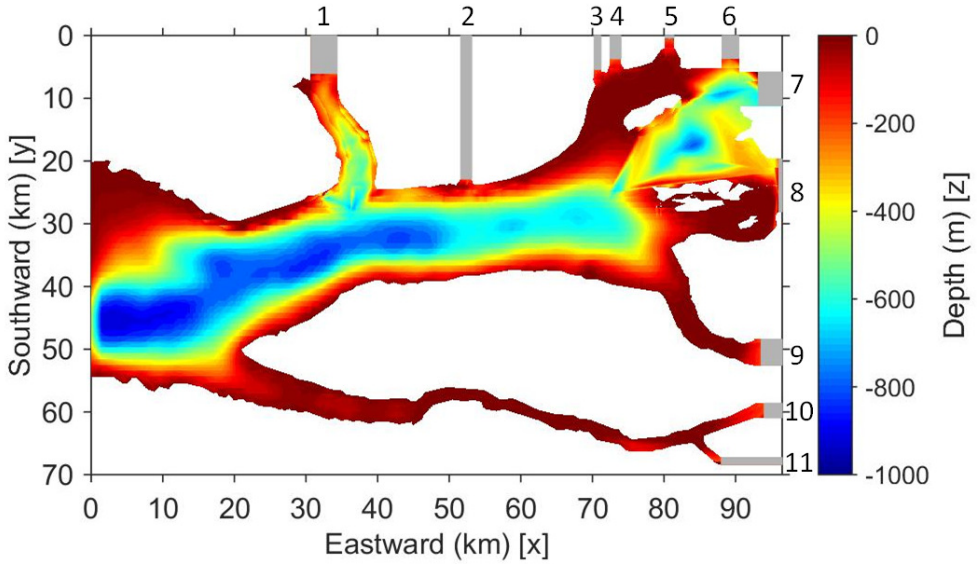


Fig. 4.2. Depth distribution in model domain. Land and 11 glacier (ice mask) areas are indicated in white and grey, respectively.

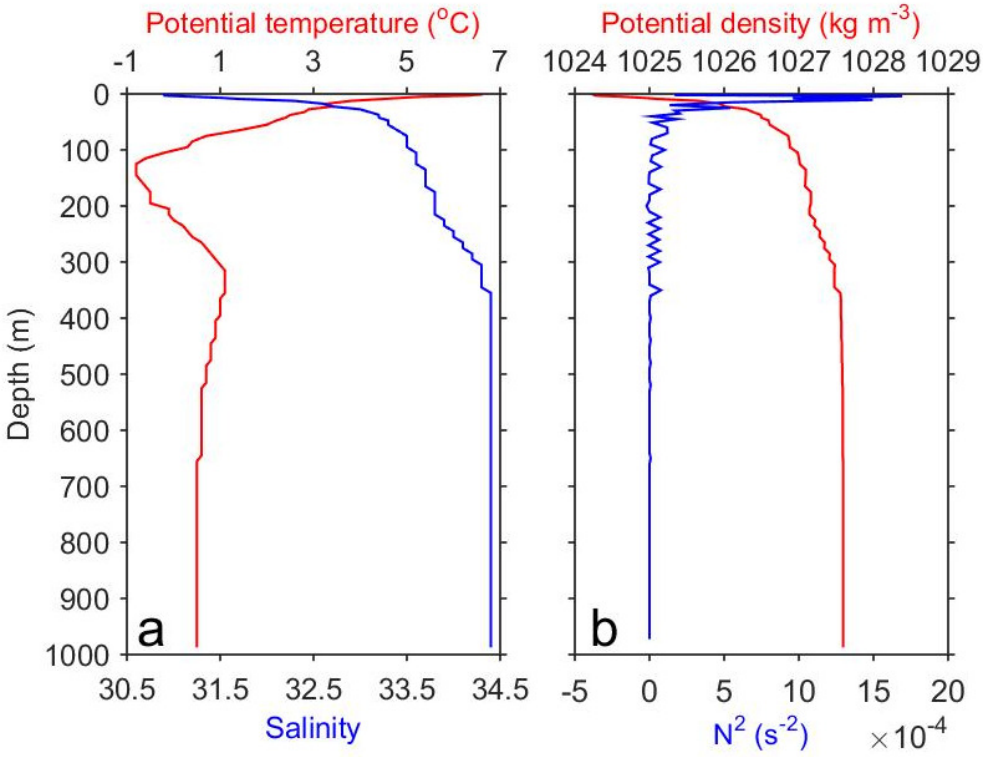


Fig. 4.3. Initial vertical profiles of (a) potential temperature, and salinity, and (b) potential density, and square of Brunt-Väisälä frequency ($N^2$) computed from (a).

Table 4.1. The details of numerical model experiment setting. The superscript of DSC (depth of subglacial drainage conduit) indicates the reference (1. Sugiyama et al., 2015; 2. Porter et al., 2014; *. No reference: the DSCs are set to the same as that of Bowdoin Glacier).

| Number | Glacier | Inflow direction | DSC (m) | Conduit length (km) | TRC | $Q_{sg}$ ($m^3$ $s^{-1}$) |
|---|---|---|---|---|---|---|
| 1 | Bowdoin | From north to south | 210[1] | 6.10 | 1 | 500 |
| 2 | Hubbard | From north to south | 210* | 22.90 | 2 | 500 |
| 3 | Hart | From north to south | 210* | 5.45 | 3 | 500 |
| 4 | Sharp | From north to south | 210* | 3.75 | 3 | 500 |
| 5 | Melville | From north to south | 210* | 0.50 | 3 | 500 |
| 6 | Farquhar | From north to south | 210* | 3.70 | 3 | 500 |
| 7 | Tracy | From east to west | 610[2] | 3.35 | 4 | 500 |
| 8 | Heilprin | From east to west | 350[2] | 0.50 | 5 | 500 |
| 9 | Leidy | From east to west | 210* | 3.00 | 6 | 500 |
| 10 | Marie | From east to west | 210* | 2.55 | 6 | 500 |
| 11 | NA | From east to west | 210* | 8.55 | 6 | 500 |

## 4.3. Results

### 4.3.1. Temporal evolutions of high turbidity water extent and sea ice cover

Temporal evolutions of turbidity water extent and sea ice cover are revealed by using the clear-sky satellite images (Fig. 4.4). Total area of high turbidity and ice cover were calculated from June to August in the study area, and were plotted with air temperature (Fig. 4.5). In June, the study area was mostly covered with ice (Fig. 4.4). On 18 June, sea ice began to break up around the mouth of IB and, on 4 July, sea ice began to break up at the eastern end of IB and area of high turbidity water began to expand rapidly (90 $km^2$).

Turbid water area emerged with increase in temperature and retreat of ice in early July. On 8 July, near the mouth of BF, ice floes F1 and F2 of sea ice drifted southward at about 6 km $d^{-1}$ and southeastward at about 3 km $d^{-1}$, respectively (red arrows in Figs 4.4 and

4.7). Turbidity water area extended from the ice front of Hubbard (No. 2) Glacier to the west (white arrows in Figs 4.6a–b and black arrow in Fig. 4.7). Later on around 12 July, sea ice melt proceeded and sea ice area became smaller (840 $km^2$ of ice area in Fig. 4.5). High turbidity water, originated from the ice front of Hubbard Glacier, advected further westward along the coastline of the northern side of IB and then proceeded offshore near the mouth of IB (white arrows in Figs 4.6c–d and green arrows in Fig. 4.7). Moreover, sea ice disintegrated and melted in AB. From 12 to 13 July, sea ice floes drifted eastward near the center of IB (F3 red arrows in Figs 4.4 and 4.7 at about 4 km $d^{-1}$) and northward near the eastern end of IB (F4 red arrows in Figs 4.4 and 4.7 at about 7 km $d^{-1}$). Near the eastern end of IB, high turbidity water was observed from the ice front of Leidy (No. 9) Glacier to the northward and eastward (white arrows in Figs 4.6c–d and green arrows in Fig. 4.7), roughly consistent with the drift direction of F4 ice floe.

Turbid water area rapidly extended in the latter half of July when air temperature was at its maximum. After 16 July, area of high turbidity water continued to expand (1320 $km^2$ on 16 July) and then reached the maximum of 2140 $km^2$ on 30 July (Fig. 4.5).

Advective patterns of high turbidity water were visible during 16–30 July. After 16 July, high turbidity waters, originated from the ice fronts of both Bowdoin (No.1) and Hubbard Glaciers, advected westward, roughly similar to the advection from Hubbard Glacier observed by 16 July (Figs 4.6g–h, and blue arrow in Fig. 4.7). After 23 July, high turbidity water advected eastward from the ice fronts of Marie (No. 10) along the coastline of southern side of IB (white arrows in Figs 4.6i–j and yellow arrow in Fig. 4.7). After 29 July, high turbidity water originated from Hubbard Glacier advected southward to the center of IB with deep water depth (white arrows in Figs 4.6k–l and orange arrow in Fig. 4.7), whose direction was slightly different from that on 23 July. After 29–30 July, from

the ice front of Heilprin (No. 8) Glacier, high turbidity water advected westward through around HØ that located at the southeastern corner of IB (white arrows in Figs 4.6k–n and orange arrows in Fig. 4.7). Advection of high turbidity waters, originated from the ice fronts of Hart (No. 3), Sharp (No. 4), Melville (No. 5), Farquhar (No. 6) and Tracy (No. 7) Glaciers, was unclear because ice covered in front of these glaciers until the end of July.

At the end of July that high turbidity area was the maximum, turbidity water area were revealed at almost all ice fronts of Bowdoin, Hubbard, Heilprin, Leidy, and Marie Glaciers (Figs 4.4 and 4.6m–n). Moreover, high turbidity water (high Rrs555) was observed along the coastline of southern side of IB from AB to the center of IB (white arrows in Figs 4.6k–l, and orange arrows in Fig. 4.7) although its origin was unclear. On the other hand, relatively low Rrs555 area was observed at the northern side of this high turbidity water from AB to the center of IB (red circles in Figs 4.6 k–n) and this is almost only region which was not covered by turbid water.

After the end of July, the high turbidity area decreased. It reached to 260 $km^2$ for the whole IB (about 12% of maximum extent) in mid-August (Fig. 4.5). On 15 August, high turbidity water was confined in BF, AB and OF (Figs 4.4 and 4.6o–p).

To summarize, high turbidity area rapidly increased from early July to mid-July with decrease in ice area. Towards the end of July, high turbidity area continued to increase, reaching its maximum. The area decreased to mid-August. Satellite image analysis indicates roughly anti-clockwise drift patterns of high turbidity water and four floes of sea ice (Fig. 4.7). Specifically, the westward advections of high turbidity water originated from Bowdoin and Hubbard Glaciers through the northern part of IB (from 8 to 16 July) and Heilprin Glacier through the southern part of IB (after 29–30 July), and the

northeastward advection of high turbidity water originated from Leidy Glacier (after 12 July) and the eastward advection from Marie Glacier (after 23 July).

### 4.3.2. Subglacial meltwater behavior in the numerical model experiment

To understand the temporal and spatial development of distribution of subglacial meltwater in the IB system, the time series of horizontal distribution of subglacial meltwater tracer from each glacier (TRC1–6) was examined using the numerical model (Figs 4.8–4.13a–c). The behavior of meltwater from each accompanying fjord/glacier is described in a clockwise manner.

In the western half of IB, subglacial meltwater spreads westward along the coast; the meltwater from BG spreads westward after passing through the BF (TRC1; Figs 4.8a and b) and meltwater from Hubbard Glacier spreads westward immediately after reaching the surface (TRC2; Figs 4.9a and b). Then, both of subglacial meltwaters proceed directly westward along the topography near the mouth of IB in around 5 days from injection (Figs 4.8c and 4.9c).

In the eastern half of IB, the subglacial meltwaters from Hart, Sharp, Melville and Farquhar Glaciers, spread gradually along the northern part of IB (TRC3; Figs 4.10a–c). These waters don't flow into the BF. From the eastern end, subglacial meltwater from Tracy Glacier spreads westward through near the ice front of Hart, Sharp, Melville and Farquhar Glaciers with avoiding the pathways of subglacial meltwaters from BG and Hubbard Glacier (TRC4; Figs 4.11a–c). From Heilprin Glacier, subglacial meltwater follows two divergent paths blocked by the islands (HØ). Then the waters proceed westward through the southern part of IB with avoiding the pathways of subglacial

meltwater originated from the other glaciers from northern and eastern flank (TRC5; Figs 4.12a–c).

From the southern flank of IB, subglacial meltwater from Leidy Glacier spread northward and eastward (TRC6; Figs 4.13a–c). Subglacial meltwater from Marie and No.11 Glaciers begin to spread eastward along the coastline of southern side of IB. It took more than a week for these waters to come out of OF.

To understand the difference in behavior of subglacial meltwater between at the fjord surface and subsurface, we also investigated the time series of cumulative subglacial meltwater tracer (Figs 4.8–4.13d–f). Behaviors of subglacial meltwater in the whole water column from 10 glaciers show similar tendencies as those at the fjord surface except Tracy Glacier (Figs 4.8, 4.9, 4.10, 4.12, and 4.13d–f). The surface water from Tracy Glacier spread and bend southward in front of Hubbard Glacier to reach almost southern flank (Fig. 4.11), while column cumulative tracer show accumulation along the northern flank. However, subglacial meltwater at all depths spread westward without flowing into the BF.

Overall, in the glaciers from the northern and eastern flank of IB (TRC1–5), subglacial meltwaters advect westward, with avoiding the pathway of subglacial meltwater from the other glaciers that located nearer the mouth of IB. It looked like that subglacial meltwaters from glaciers that located nearer the mouth of IB blocked the northward spread of subglacial meltwater from the other glaciers. On the other hand, from the southern flank of IB (TRC6), subglacial meltwater spreads eastward toward the end of IB along the coastline of southern side of IB, with some notable delay caused by the longer residence time in OF compared to the other sub-fjords (BF and AB).

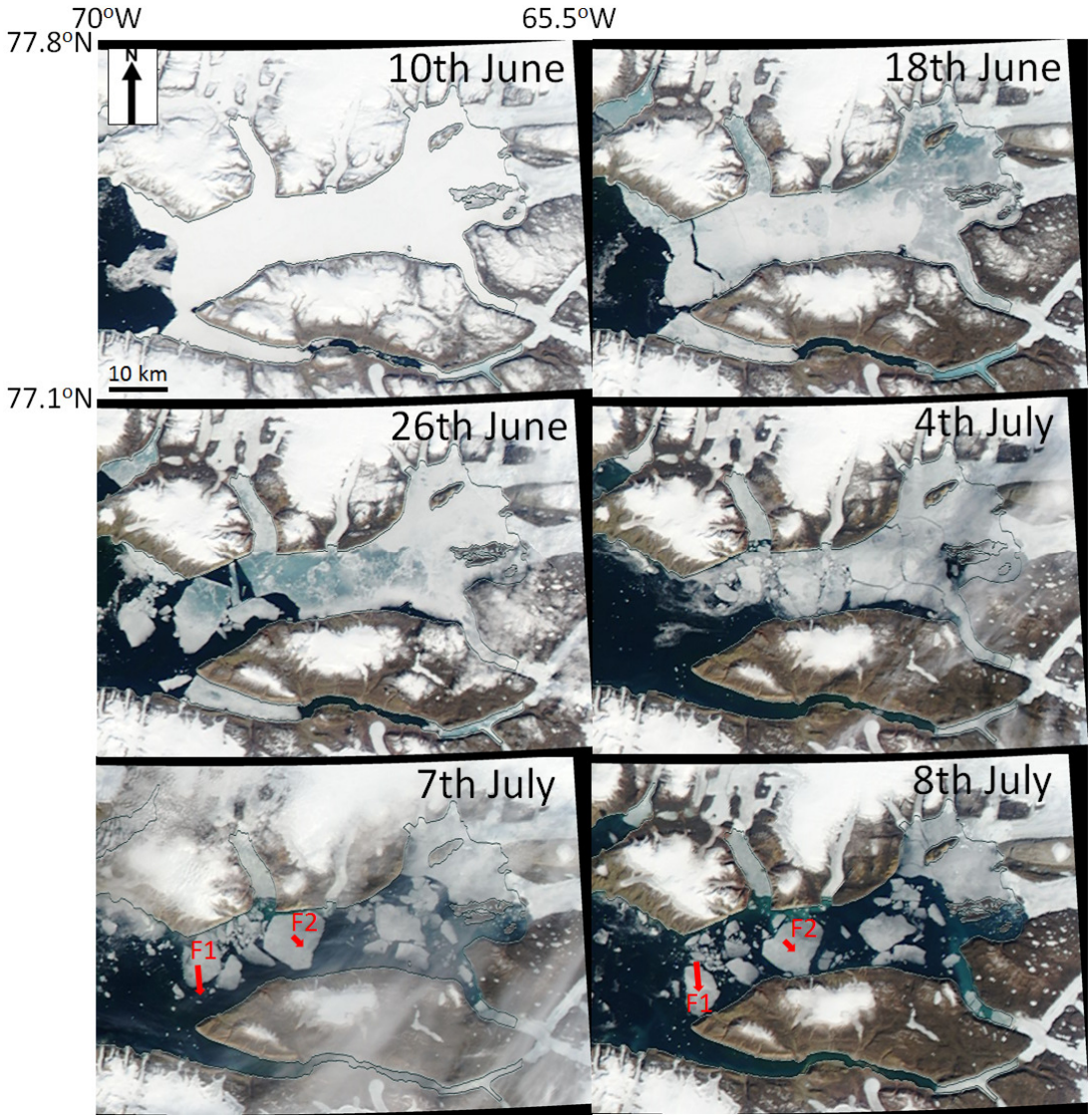


Fig. 4.4. Time series of MODIS true color image around Inglefield Bredning in 2016. The 17 images are selected and the images taken on 11, 12, 15 and 28 June were not shown. The image with cloud cover on 7 July was shown to investigate the sea ice drift. Red arrows show drift pattern of sea ice floe.

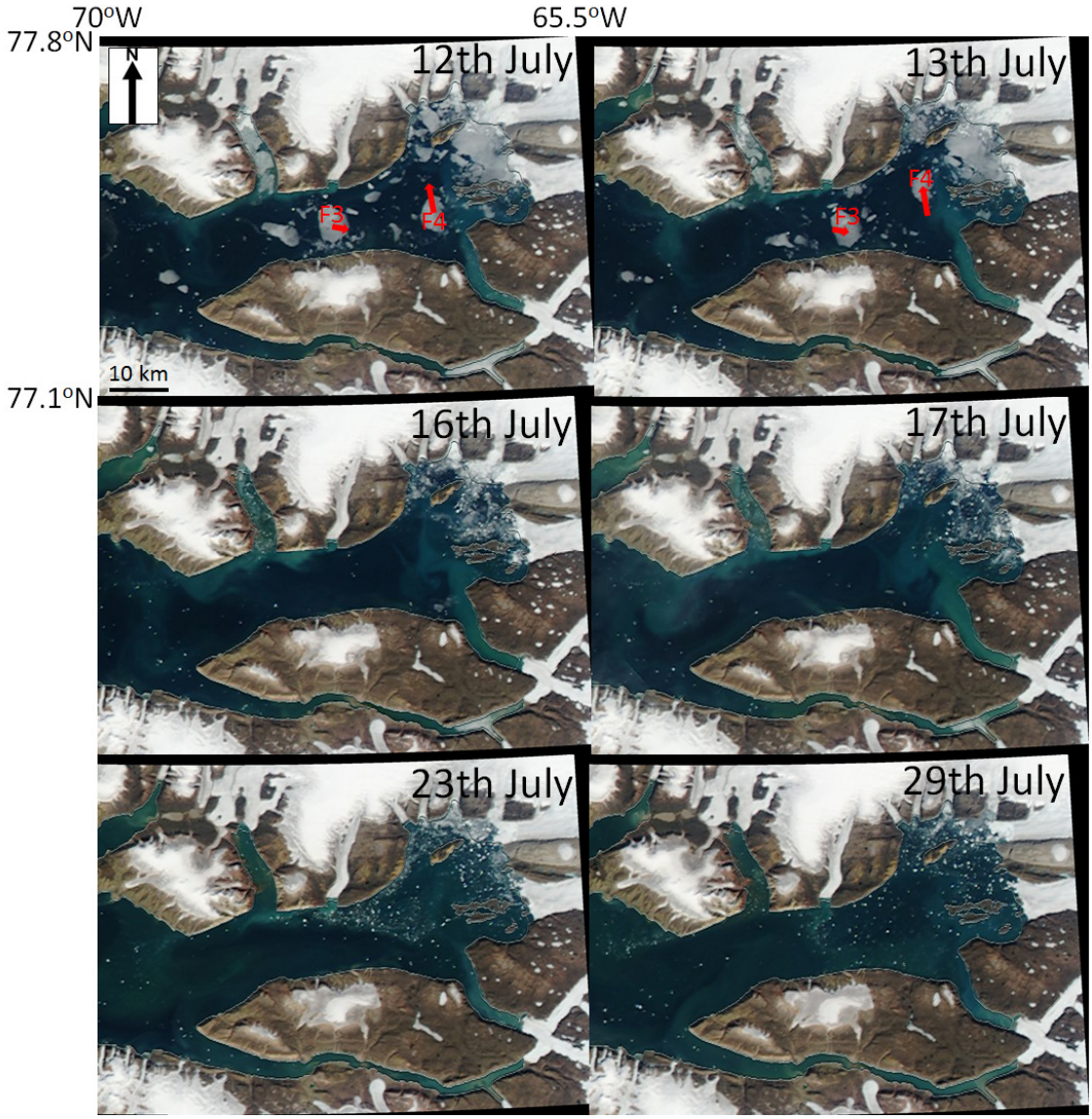


Fig. 4.4. (Continued.)

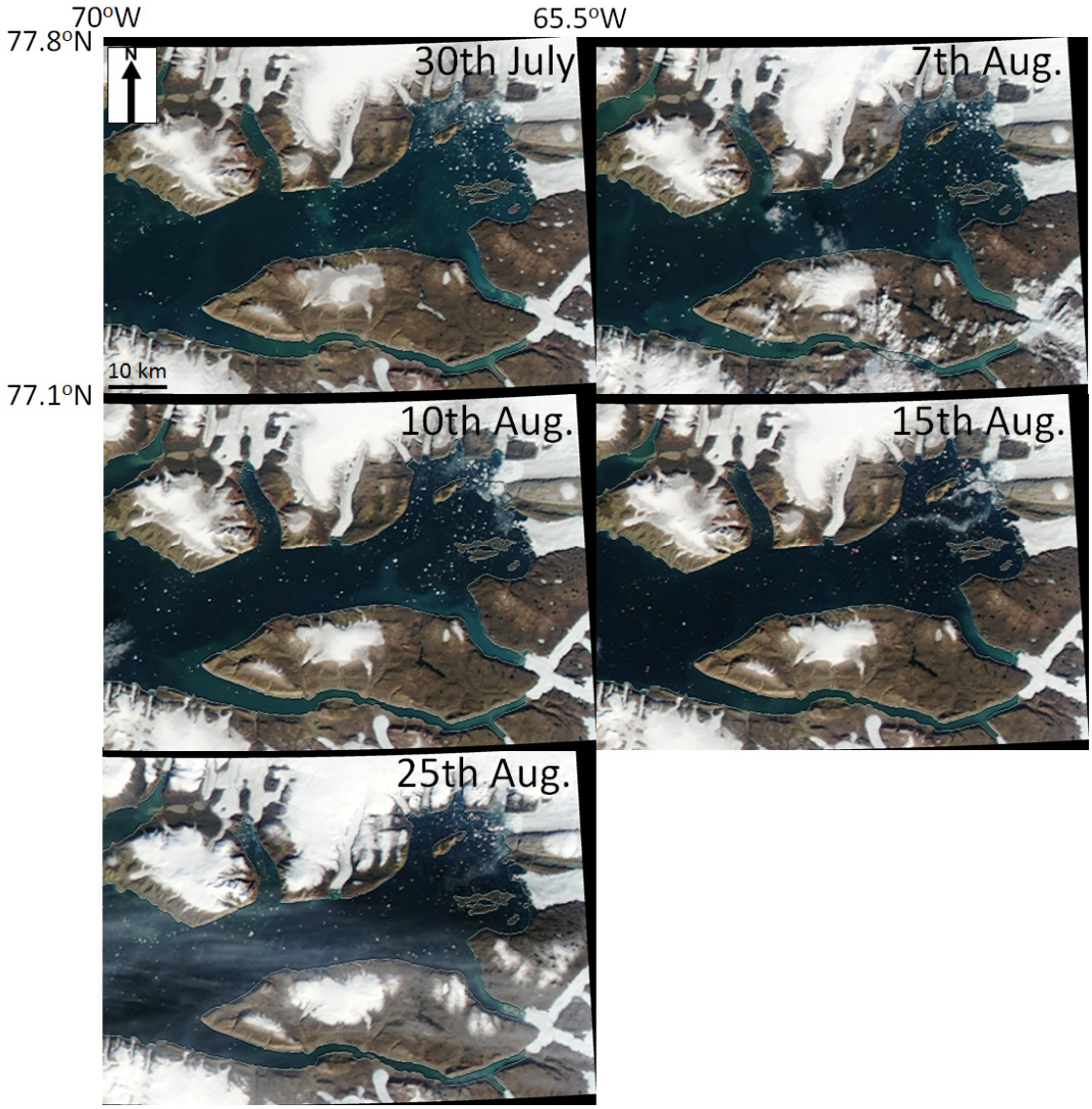


Fig. 4.4. (Continued.)

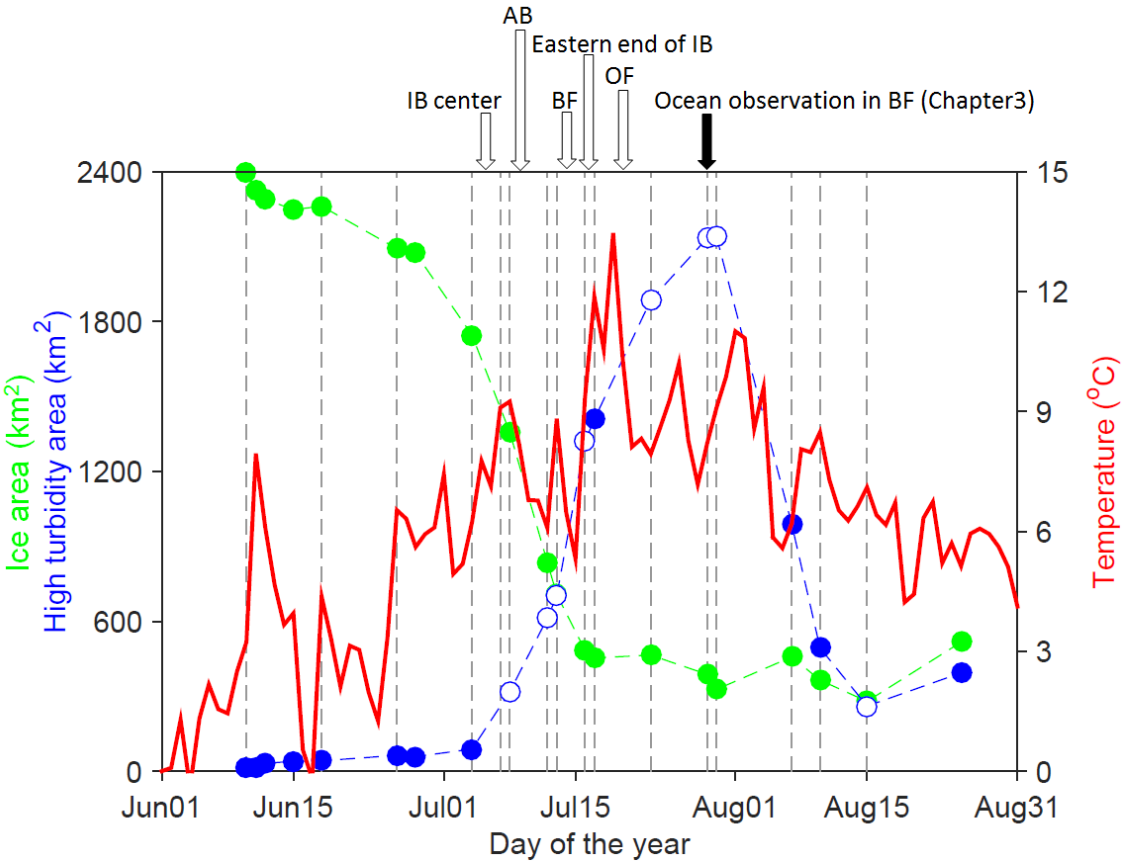


Fig. 4.5. Temporal development of high turbidity area (blue) and ice area (green), and daily mean air temperature at Qaanaaq Airport (red) from June to August in 2016. Black open arrows indicate the days that ice disintegration in each fjord. Dashed grey lines indicate the days shown in Fig. 4.4. Blue open circles indicate the extents of high turbidity area in the days shown in Fig. 4.6.

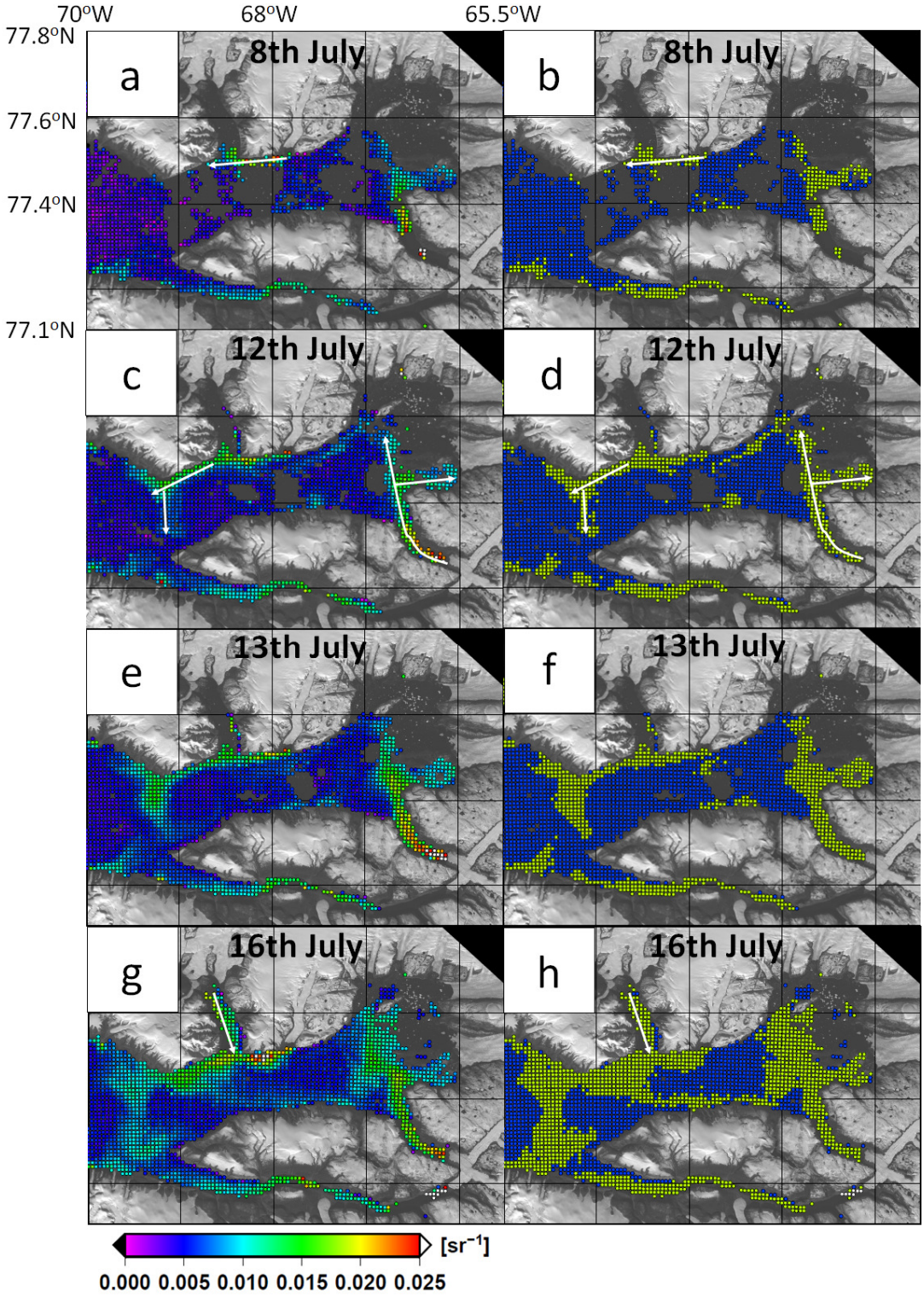


Fig. 4.6. Daily composite of Rrs555 values and high turbidity area (Rrs555 ≥ 0.0070 $sr^{-1}$) indicated by greenish yellow pixels in this study area on (a, b) 8, (c, d) 12, (e, f) 13 and (g, h) 16 July in 2016. White arrows indicate drift pattern of high turbidity water.

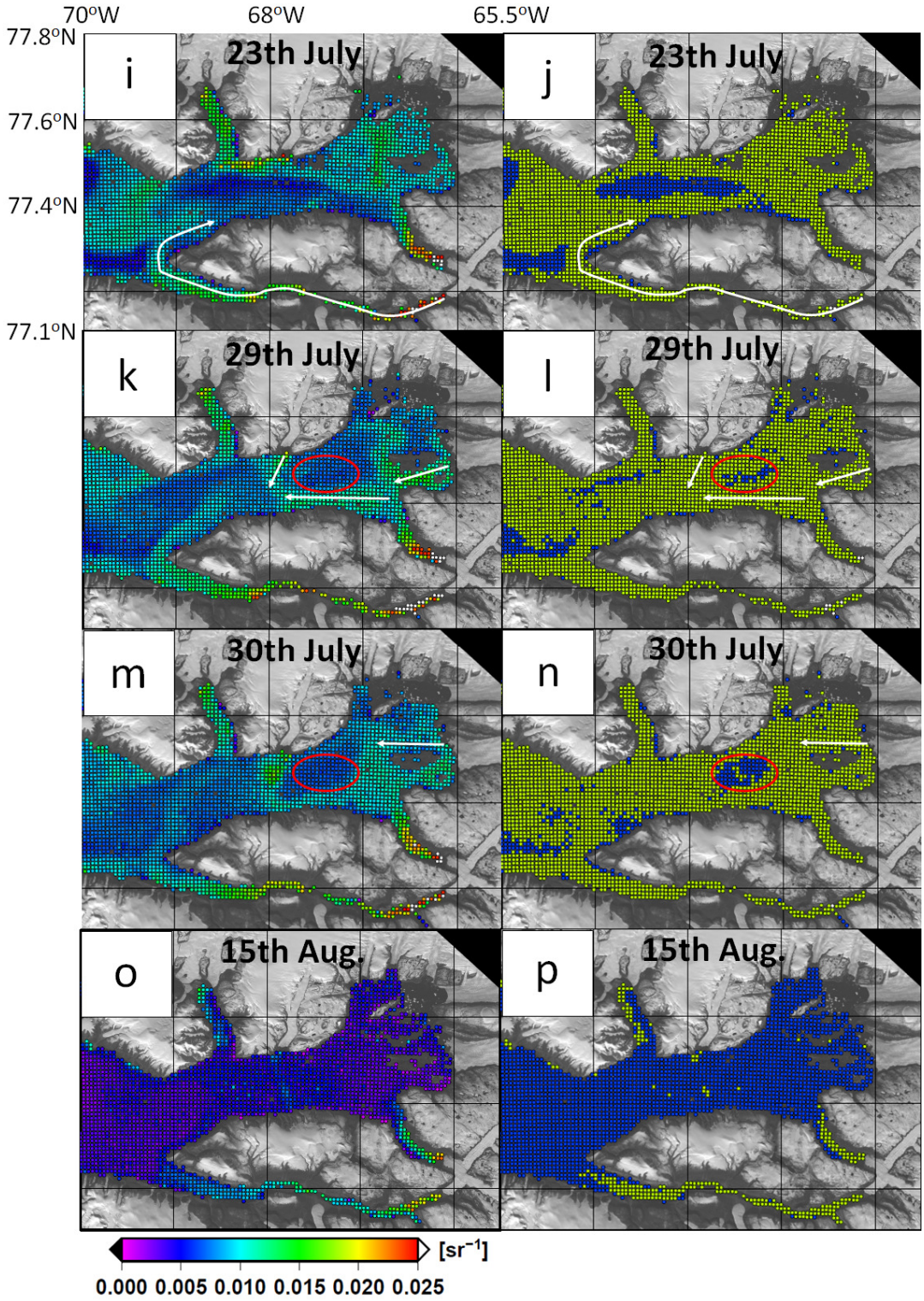


Fig. 4.6. (Continued.) Daily composite of Rrs555 values and high turbidity area (Rrs555 ≥ 0.0070 $sr^{-1}$) indicated by greenish yellow pixels in this study area on (i, j) 23, (k, l) 29 and (m, n) 30 July, and (o, p) 15 August in 2016.

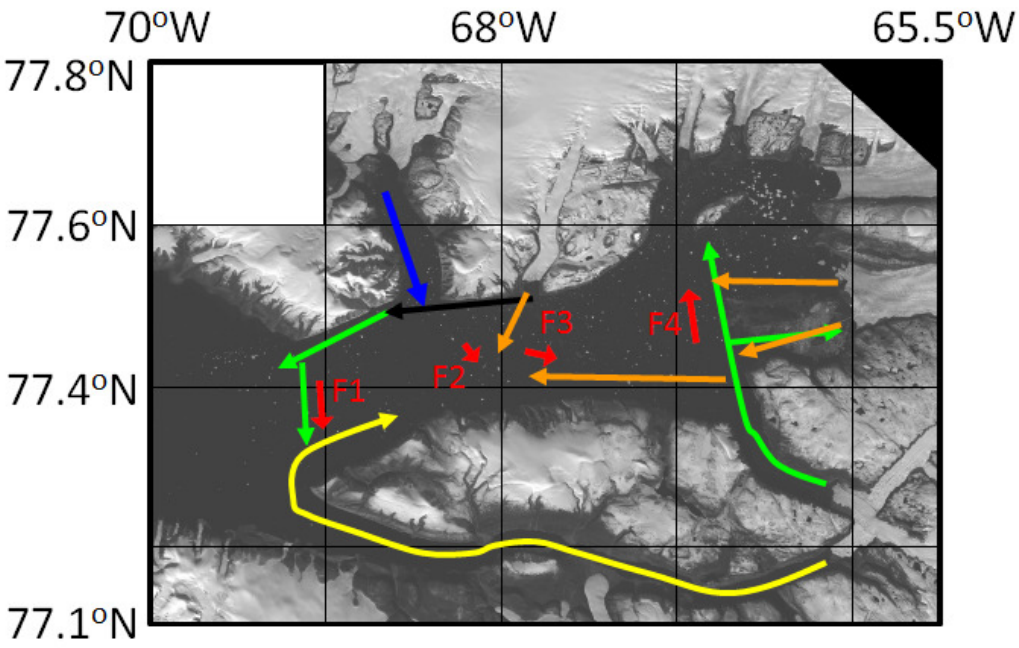


Fig. 4.7. Schematic diagram showing the observed drift patterns of turbid glacial meltwater (black arrow; after 7–8 July, green arrows; after 12 July, blue arrow; after 16 July, yellow arrow; after 23 July, orange arrows; after 29–30 July) and sea ice floes (red arrows).

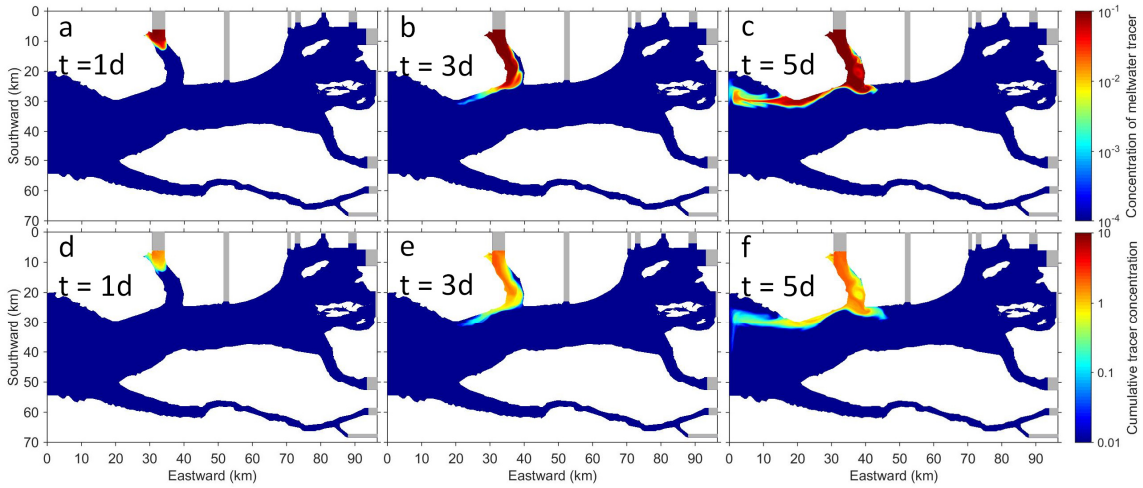


Fig. 4.8. Time series of horizontal distribution of subglacial meltwater tracer concentration at the fjord surface (0–2 m depth) (a–c) and vertically integrated tracer concentration every 10 m (d–f) from Bowdoin Glacier (TRC1) after the integration of 1, 3 and 5 days, respectively.

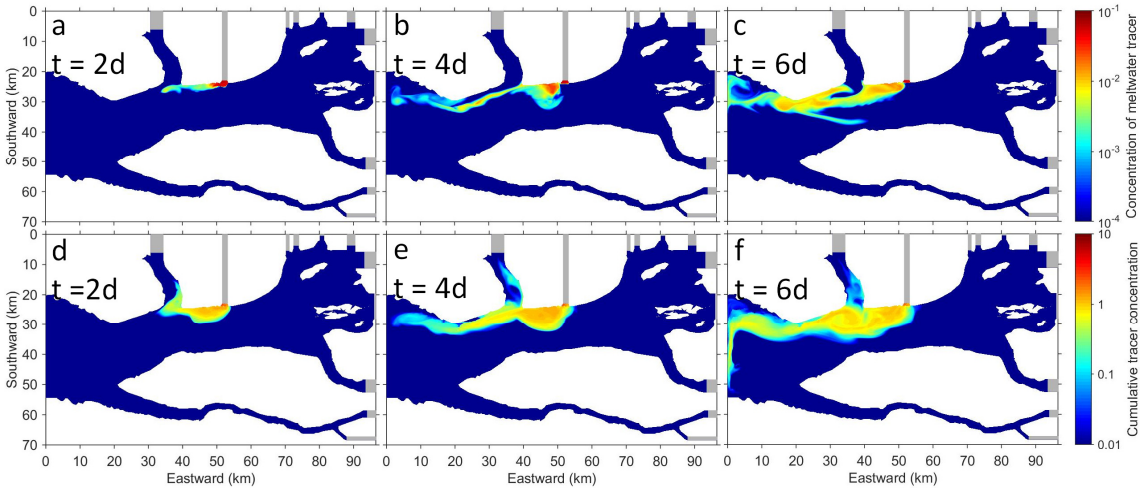


Fig. 4.9. Same as Fig. 4.8, but for from Hubbard Glacier (TRC2). (a, d), (b, e) and (c, f) are the results after the integration of 2, 4 and 6 days, respectively.

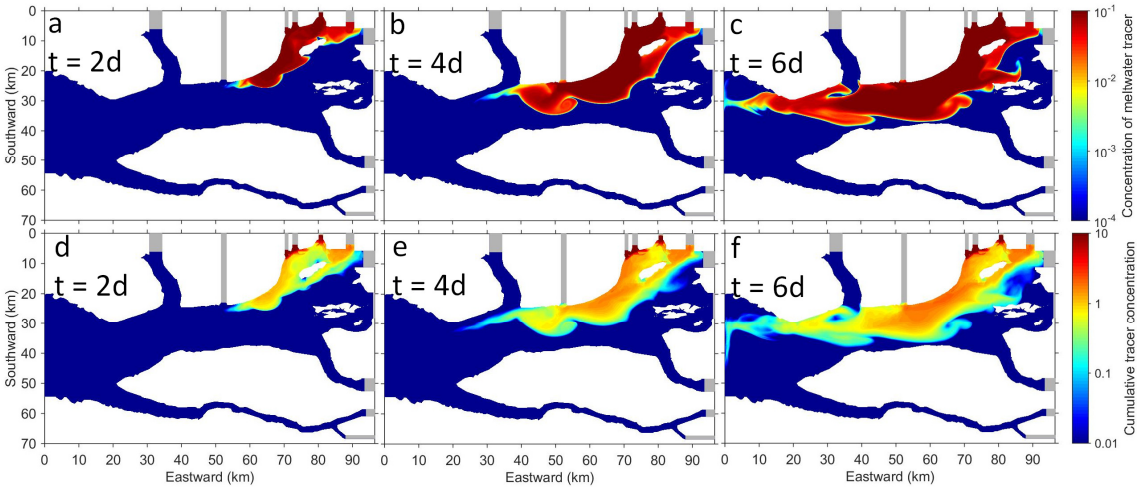


Fig. 4.10. Same as Fig. 4.8, but for from Hart, Sharp, Melville and Farquhar Glaciers (TRC3). (a, d), (b, e) and (c, f) are the results after the integration of 2, 4 and 6 days, respectively.

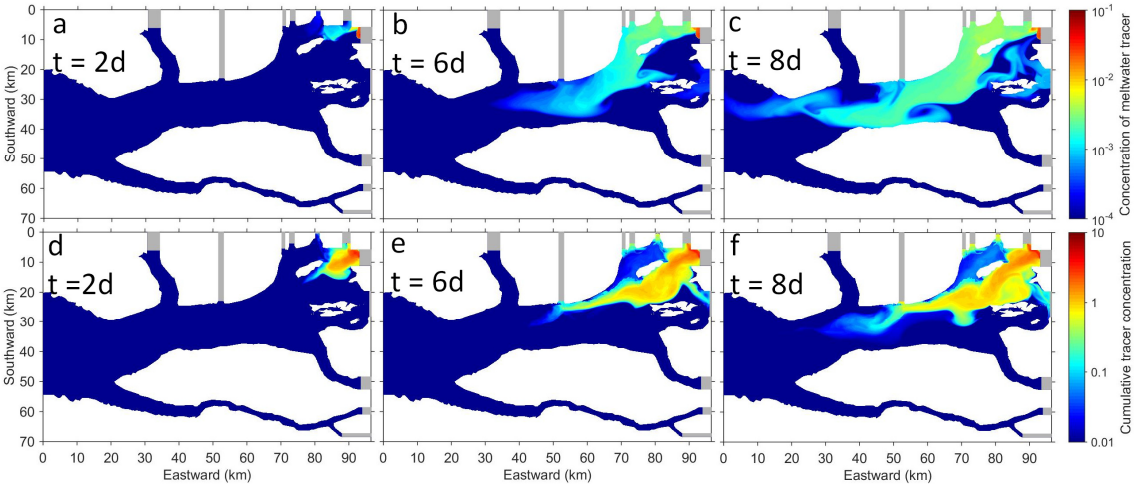


Fig. 4.11. Same as Fig. 4.8, but for from Tracy Glacier (TRC4). (a, d), (b, e) and (c, f) are the results after the integration of 2, 6 and 8 days, respectively.

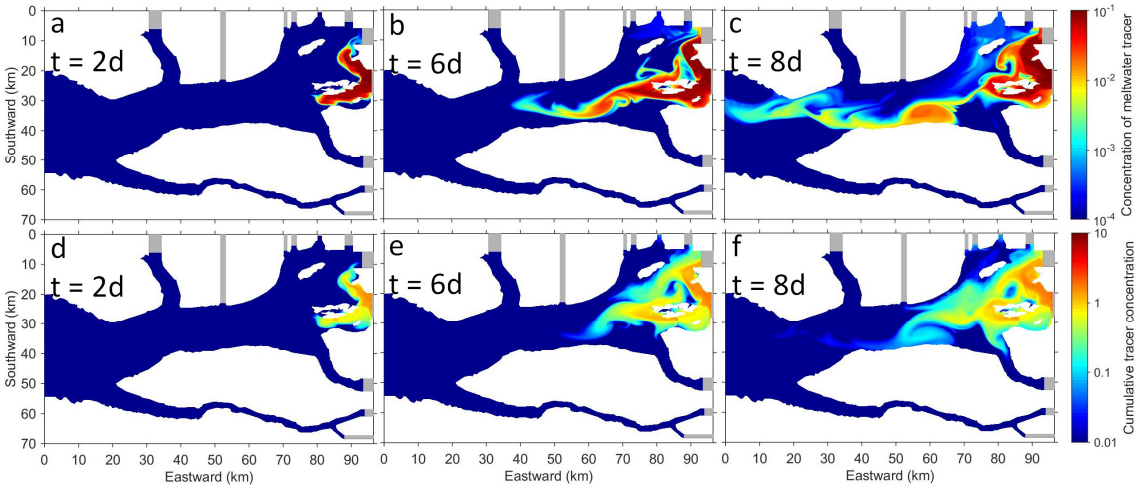


Fig. 4.12. Same as Fig. 4.8, but for from Heilprin Glacier (TRC5). (a, d), (b, e) and (c, f) are the results after the integration of 2, 6 and 8 days, respectively.

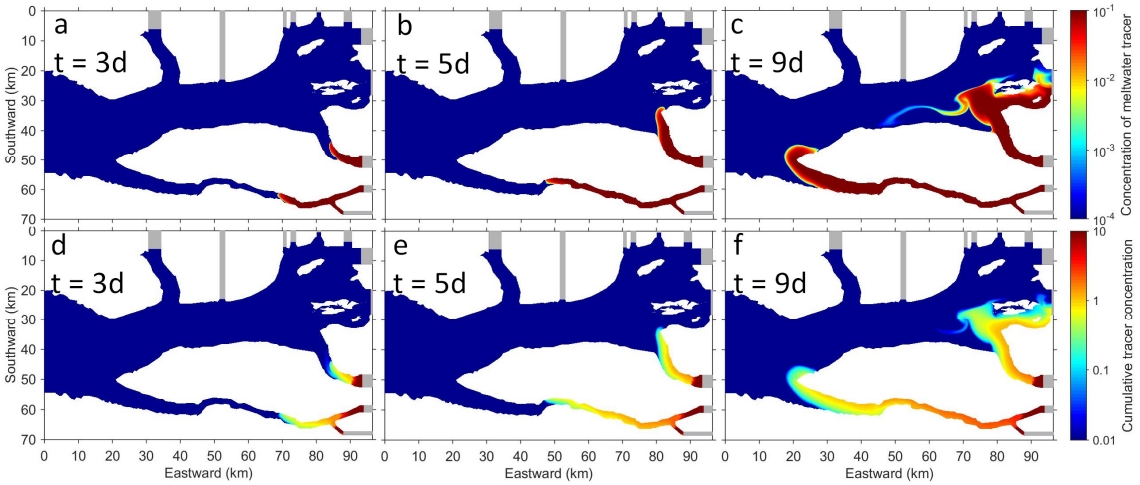


Fig. 4.13. Same as Fig. 4.8, but for from Leidy, Marie and No.11 glaciers (TRC6). (a, d), (b, e) and (c, f) are the results after the integration of 3, 5 and 9 days, respectively.

## 4.4. Discussion

### 4.4.1. Relationship between temporal development of the extent of high turbidity area and air temperature

Air temperature affects melt on glacial surfaces and the discharge amount of turbid subglacial meltwater is often represent by positive degree day. Thus, the temporal change in air temperature can control the temporal development of the extent of high turbidity area in the proglacial fjord. We investigate the relationship between the temporal development of the extent of high turbidity area and temporal change in air temperature.

Daily mean air temperature at Qaanaaq Airport (blue circle in Fig. 4.1) increased from between mid-June and late June to mid-July, reaching the maximum of 13.5$^{o}$C on 19 July (red line in Fig. 4.5). After mid-July, temperature decreased, with fluctuations on a few day scales, to 4–7$^{o}$C in mid-August.

The maximum extent of high turbidity area occurred on 30 July, which was about 10 days after the highest air temperature (Fig. 4.5). Numerical model results show that the subglacial meltwater from each glacier reaches the western mouth and eastern end of IB at least from 5 days to 10 days later after the injection of subglacial meltwater discharge (Figs 4.8–4.13). Considering the time required for glacier surface meltwater to reach the subglacial drainage system, this time scales from the start of subglacial discharge to spreading of meltwater over the fjord surface is roughly consistent between satellite observation and numerical model.

In mid-August after the continuous decrease in air temperature, high turbidity area reached the minimum (Fig. 4.5). High turbidity water was observed only in BF, AB and OF (Fig. 4.6o–p). This result suggests that turbid subglacial meltwater discharges,

associated with a small amount, could reach surface only in relatively shallow BF, AB and OF and not in the deeper parts. This might be a limitation of using satellite image as a proxy of meltwater discharge. In addition to the effect of small amount of discharge, change in the strength of near-surface stratification can lead to low turbidity at the surface. Meltwater discharge enhance the fjord stratification and the resultant strong fjord stratification prohibits further upwelling of turbid subglacial meltwater. The strong stratification in mid-August can prohibit reaching of turbid subglacial meltwater at the fjord surface.

### 4.4.2. Drift patterns of turbid glacial meltwater and sea ice floes

From satellite images, surface drift patterns in IB fjord system were obtained as in Fig. 4.7. Here we compare and interpret the patterns with the results of numerical model.

In the western half region, overall anti-clockwise rotation of the turbid waters is clear in the satellite observation. The westward drifts along the northern coast were consistent with the meltwater discharges from the BG and Hubbard Glacier. The eastward motion was consistent with the behavior of the discharge from Marie and No.11 Glaciers. The southward motion of F1 ice floe around 69$^{o}$W, however, was not reproduced in our numerical model. Ice floe drift can be affected by the wind field, and hence the drift pattern is not a direct evidence of oceanic current, but a southward tongue of highly turbid water was also visible at almost the same location. The IBCAO bathymetry shows a hint of sill-like structure around this area.

In the eastern half region where the several glaciers feed meltwaters, the drift pattern was more complex. The northward and eastward spread from Leidy Glacier in early summer was easily explained by the model result. However, accumulation process and

origins of turbid waters in front of the eastern end of ice fronts were difficult to be distinguished, from the incomplete time series under the presence of patchy ice. Nevertheless, westward motion along the southern coast in late July can be consistent with the modeled discharges from the Heilprin Glacier, which flowed south of the meltwaters from other north-bound glaciers. However, the void spot around 67.5°W from the satellite images were not quite clear in the numerical model (red circles in Figs. 4.6 k–n). The modeled pathways of meltwater can be affected by the amount of discharge from the other glaciers. Hence we should be careful in the interpretation of these patterns, given the limited representation of bathymetry and validity of the amount of meltwater discharge.

## 4.5. Summary

Behavior of turbid glacial meltwater in IB fjord system, northwestern Greenland, in 2016 were analyzed by satellite images. The meltwater pathway was interpreted with numerical model experiments.

In the IB fjord system, high turbidity area increased from mid-July to the end of July (2140 $km^2$) and then decreased until mid-August (260 $km^2$). This maximum extent of high turbidity area occurred about 10 days later after the timing of the highest air temperature. This result suggests that the whole sequence of processes, from ice surface melt and subglacial meltwater discharge to spreading of turbid subglacial meltwater over the fjord surface, takes about 10 days. Given the meltwater runoff reach the conduit mouth within a few days, the time scale was roughly consistent with the time scale from the start of subglacial discharge to spreading of meltwater at the fjord surface in the numerical model experiment. In mid-August that after the continuous decrease in air temperature,

high turbidity area reached the minimum. High turbidity water was observed only in BF, AB and OF.

Drift patterns of turbid glacial meltwater from Bowdoin, Hubbard, Heilprin, Leidy, Marie Glaciers and sea ice floes were observed in the IB fjord system. Overall, anticlockwise patterns were obtained, possibly overlaid by the pattern that meltwater discharges from the glacier that located nearer the mouth of IB blocks the northward spread of subglacial meltwater from the other glaciers and leads to the westward advection from the other glaciers through the more southern part of IB.

The satellite imagery is proved to be powerful in reproducing the temporal development of turbid waters in the IB fjord system, there are intrinsic limitations in spatial samplings due to the cloud and ice masks and restriction to the surface. The numerical model is useful to investigate the behaviors of the meltwaters, even with the uncertainty of the amount of discharge. More case studies with different discharge and stratification can lead to a better assessment on realistic meltwater discharge and behavior. However, the present information on bathymetry in this region is probably not sufficient to fully implement the effectiveness of the numerical model. It is needless to say that more realistic estimates on discharge amount is one of the goals of the fjord system study, future surveys on detailed bathymetry will certainly merit the better understanding of the behavior of the meltwaters discharge and response of whole fjord system.

# Chapter 5

# Conclusions

## 5.1. Glacial meltwater distribution in the northwestern Greenlandic fjord

Targeting at the northwestern Greenlandic fjord, we performed remote sensing data analyses, in-situ observations and numerical model experiments to investigate the horizontal and vertical distributions of turbid glacial meltwater, and the factors controlling their variability.

First, remote sensing data analyses were carried out to quantify the spatial and temporal variations in high turbidity surface water off the Thule region. The high turbidity area was distributed near the front of outlet glaciers that discharge glacial meltwater from the ice sheet and ice caps. The extent of the high turbidity area exhibited substantial seasonal and interannual variability, and its annual maximum extent was significantly correlated with summer air temperature. Thus, the high turbidity surface water can originate from the discharge of turbid glacial meltwater. This relationship between the turbidity area and discharge is likely applicable to not only off the Thule region but also the regions that consist of the relatively large shelf area and glaciers located near the open ocean/fjord off the western Greenland coast. Assuming a linear relationship between the high turbidity area and summer temperature, annual maximum extent increases under the influence of increasing glacial meltwater discharge.

Second, in-situ observations and numerical model experiments were performed in the Bowdoin Fjord to quantify the vertical distribution of subglacial meltwater and reveal its controlling factor. The maximum subglacial meltwater fraction was observed at the subsurface layer (15–40 m) near the ice front (~6.0% in 2014, ~4.0% in 2016). The

difference in the subglacial meltwater fraction at the subsurface can be due to the interannual difference in ambient fjord stratification depending on the layer developed (submarine melt layer in 2014, seasonal pycnocline in 2016) and the amount of subglacial discharge. Near the surface (5–15 m), turbidity was higher in 2016 than in 2014, consistent with the stronger influence of turbid subglacial meltwater. The numerical model result with 20% larger discharge suggests that the difference near the surface is primarily affected by the increase in discharge. As the amount of meltwater discharge increases, the outcrop area of turbid subglacial meltwater at the fjord surface can be expected to spread broader with higher subglacial meltwater fraction.

Third, satellite data analyses and numerical model experiments were performed in the whole Inglefield Bredning in 2016 to understand the broader behavior of turbid glacial meltwater and link between the Bowdoin Fjord and a broader fjord system. In the Inglefield Bredning fjord system, the maximum extent of high turbidity area occurred on 30 July (2140 $km^2$), which was about 10 days after the timing of the highest air temperature. This result suggests that the whole sequence of processes, from ice surface melt and subglacial meltwater discharge to spreading of turbid subglacial meltwater over the fjord surface, takes about 10 days. The observed high turbidity water can reflect the anticlockwise drift patterns of turbid glacial meltwater, possibly overlaid by the pattern that meltwater discharges from the glacier that located nearer the mouth of Inglefield Bredning blocked the northward spread of subglacial meltwater from the other glaciers and leads to the westward advection from the other glaciers through the more southern part.

From the above, this study indicated that the amount of glacial meltwater discharge and fjord stratification can control the horizontal and vertical distributions of turbid

glacial meltwater in the northwestern Greenlandic fjord. Based on the relationship the distribution of turbid glacial meltwater and the amount of glacial meltwater discharge, turbid glacial meltwater at the surface can spread broader with higher concentration under the influence of increasing glacial meltwater discharge, as can be inferred from present and predicted future trends. The results in this study contribute to a better understanding of the impact of glacial meltwater discharge on the fjord environment that is the current important issue.

Moreover, results in this study can lead to the assessment on nutrient transport and its impact on marine biological productivity. For example, with a focus on the subsurface in Bowdoin Fjord, subglacial meltwater fraction was higher in 2014 than in 2016, while entrained fjord water fraction was lower in 2014 (Chapter 3). Previous studies suggest that subglacial plume formation can have a potential impact on marine biological productivity due to the delivery of ambient ocean water containing macro and micro nutrients by the plume (Arendt et al., 2011; Lydersen et al., 2014; Meire et al., 2017). Assuming that the entrained fjord water contains the same amount of nutrients, in 2016 when fraction of entrained fjord water was higher, transport amounts of nutrient to the subsurface was larger. Thus, in 2016, larger transport amounts of nutrient might become more active in marine biological production. From the above, the quantification of glacial meltwater distribution can assess the nutrient transport and its impact on marine biological production in fjord.

## 5.2. Future prospects of the study

We investigated the three dimensional distribution of turbid glacial meltwater and its

variability in the northwestern Greenlandic fjord. This study in Chapter 3 revealed that the relationship between fraction of subglacial meltwater and turbidity. To better understand the transport process of suspended sediment by glacial meltwater discharge, more accurate quantitative assessment on turbidity is needed. Thus, as a next step of this study, it is necessary to quantify the horizontal and vertical distributions of suspended sediment concentration. By revealing distribution of suspended sediment concentration and its quantitative relationship with glacial meltwater fraction, we can lead to the better understanding of the transport process of suspended sediment by glacial meltwater discharge taking into account the sediment settlings and its impact on marine productivity.

Moreover, this study suggests that the fjord stratification including AW and PW, together with the amount of subglacial meltwater discharge, can affect the distribution of turbid glacial meltwater. However, because ocean observations had been limited during summer, the detailed long-term formation process of stratified structure including AW and PW was incompletely understood. To better understand the impact of change in fjord stratification on the distribution of glacial meltwater, it is hence essential to investigate the long-term (seasonal and interannual) variability in the physical properties of AW and PW. A mooring has been deployed in Bowdoin Fjord since August 2016 to reveal long-term variability of ocean current, temperature and salinity in the deep layer of the fjord, including AW and PW layers (Fukamachi et al., 2017). Combining this mooring data and summer CTD data, and performing the numerical experiment based on these observational data are required to assess the long-term formation process of stratified structure and the future changes in glacial meltwater distribution affected by fjord stratification.

## References

Andersen, M. L., L. Stenseng, H. Skourup, W. Colgan, S.A. Khan, S.S. Kristensen, S.B. Andersen, J.E. Box, A.P. Ahlstrøm, X. Fettweis, and R. Forsberg (2015), Basin-scale partitioning of Greenland ice sheet mass balance components (2007–2011), *Earth Planet. Sci. Lett.*, **409**, 89–95.

Arendt, K. E., J. Dutz, S. H. Jónasdóttir, S. Jung-Mads, J. Mortensen, E. F. Møller, and T. G. Nielsen (2011), Effects of suspended sediments on copepods feeding in a glacial influenced sub-Arctic fjord, *J. Plankt. Res.*, **33**, 1526–1537.

Atlas, R., R. N. Hoffman, J. Ardizzone, S. M. Leidner, J. C. Jusem, D. K. Smith, and D. Gombos (2011), A cross-calibrated, multiplatform ocean surface wind velocity product for meteorological and oceanographic applications. *Bulletin of the American Meteorological Society*, **92**, 157–174.

Bamber, J., M. van den Broeke, J. Ettema, J. Lenaerts, and E. Rignot (2012), Recent large increases in freshwater fluxes from Greenland into the North Atlantic, *Geophys. Res. Lett.*, **39**, L19501. http://dx.doi.org/10.1029/2012GL052552.

Bendtsen, J., J. Mortensen, K. Lennert, and S. Rysgaard (2015), Heat sources for glacial ice melt in a West Greenland tidewater outlet glacier fjord: The role of subglacial freshwater discharge, *Geophys. Res. Lett.*, **42**, 4089–4095.

Box, J. E. (2013), Greenland Ice Sheet Mass Balance Reconstruction. Part II: Surface Mass Balance (1840–2010), *J. Climate*, **26**, 6974–6989.

Caballero, I., E.P. Morris, L. Prieto, and G. Navarro (2014), The influence of Guadalquivir River on the spatio-temporal variability of suspended solids and chlorophyll in the Eastern Gulf of Cadiz, *Mediterranean Marine Science*, **15** (4), 721–738.

Caballero, I., J. Ruiz, and G. Navarro (2011), Dynamics of the turbidity plume in the

Guadalquivir estuary (SW Spain): a remote sensing approach. *IEEE Oceans*.

Carroll, D., D. A. Sutherland, E. L. Shroyer, J. D. Nash, G. A. Catania, and L. A. Stearns (2015), Modeling turbulent subglacial meltwater plumes: Implications for fjord-scale buoyancy-driven circulation, *J. Phys. Oceanogr.*, **45**(8), 2169–2185.

Carroll, D., D. A. Sutherland, E. L. Shroyer, J. D. Nash, G. A. Catania, and L. A. Stearns (2017), Subglacial discharge-driven renewal of tidewater glacier fjords, *J. Geophys. Res. Oceans*, **122**, 6611–6629.

Chauché, N., A. Hubbard, J. C. Gascard, J. E. Box, R. Bates, M. Koppes, A. Sole, P. Christoffersen, and H. Patton (2014), Ice-ocean interaction and calving front morphology at two west Greenland tidewater outlet glaciers, *The Cryosphere*, **8**, 1457–1468.

Chu, V.W. (2014), Greenland ice sheet hydrology: a review, *Prog. Phys. Geogr.*, **38**(1), 19–54.

Chu, V.W., L.C. Smith, A.K. Rennermalm, R.R. Forster, and J.E. Box (2012), Hydrologic controls on coastal suspended sediment plumes around the Greenland Ice Sheet, *The Cryosphere*, **6**(1), 1–19.

Chu, V.W., L.C. Smith, A.K. Rennermalm, R.R. Forster, J.E. Box, and N. Reeh (2009), Sediment plume response to surface melting and supraglacial lake drainages on the Greenland ice sheet, *Journal of Glaciology*, **55**(194), 1072–1082.

Cuffey, K. M., and W. S. B. Paterson (2010), *The Physics of Glaciers*, 4th ed., Elsevier, Amsterdam.

Dawes, P.R. and D. van As (2010), An advancing glacier in a recessive ice regime: Berlingske Bræ, North-West Greenland, *Geol. Surv. Den. Greenl. Bull.*, **20**, 79–82.

Enderlin, E., I. Howat, S. Jeong, M. Noh, J. van Angelen, and M. van den Broeke (2014),

An improved mass budget for the Greenland Ice Sheet, *Geophys. Res. Lett.*, **41**, 866–872.

Fettweis, X., B. Franco, M. Tedesco, J. H. Van Angelen, J. T. M. Lenaerts, M. R. Van Den Broeke, and H. Gallee (2013a), Estimating the Greenland Ice Sheet surface mass balance contribution to future sea level rise using the regional atmospheric climate model MAR, *The Cryosphere*, **7**, 469–489.

Fettweis, X., E. Hanna, C. Lang, A. Belleflamme, M. Erpicum, and H. Gall (2013b), Brief communication "Important role of the mid-tropospheric atmospheric circulation in the recent surface melt increase over the Greenland Ice Sheet", *The Cryosphere*, **7**, 241–248.

Fukamachi, Y., N. Kanna, S. Sugiyama, Y. Ohashi, D. Sakakibara, and D. Nomura (2017), Mooring measurement in Bowdoin Fjord in northwestern Greenland, Abstract of The Eighth Symposium on Polar Science, OMp3

Gade, H. G. (1979), Melting of ice in sea water: A primitive model with application to the Antarctic ice shelf and icebergs, *Journal of Physical Oceanography*, **9**, 189–198.

Hall, D. K., R. S. Williams Jr., S. B. Luthcke, and N. E. Digirolamo (2008), Greenland ice sheet surface temperature, melt and mass loss: 2000–06, *Journal of Glaciology*, **54** (184), 81–93.

Hamilton, J., and Y. Wu (2013), Synopsis and trends in the physical environment of Baffin Bay and Davis Strait, *Canadian Technical Report of Hydrography and Ocean Sciences*, **282**, vi-39.

Hanna, E., P. Huybrechts, K. Steffen, J. Cappelen, R. Huff, C. Shuman, T. Irvine-Fynn, S. Wise, and M. Griffiths (2008), Increased runoff from melt from the Greenland Ice Sheet: a response to global warming, *J. Climate*., **21**(2), 331–341.

Hetland, R.D. (2005), Relating river plume structure to vertical mixing, *Journal of Physical Oceanography*, **35**(9), 1667–1688.

Hopwood, M. J., S. Bacon, K. Arendt, D. P. Connelly, and P. J. Statham (2015), Glacial meltwater from Greenland is not likely to be an important source of Fe to the North Atlantic, *Biogeochemistry*, **124**(1), 1–11.

Hudson, B., I. Overeem, D. McGrath, J.P.M. Syvitski, A. Mikkelsen, and B. Hasholt (2014), MODIS observed increase in duration and spatial extent of sediment plumes in Greenland fjords, *The Cryosphere*, **8** (4), 1161–1176.

Hurrell, J.W. (1995), Decadal trends in the North Atlantic Oscillation: Regional temperatures and precipitation, *Science*, **269** (5224), 676–679.

Jakobsson, M., et al. (2012), The International Bathymetric Chart of the Arctic Ocean (IBCAO) Version 3.0, *Geophysical Research Letters*, **39**, L12609, doi: 10.1029/2012GL052219.

Jenkins, A. (1999), The impact of melting ice on ocean waters, *J. Phys. Oceanogr.*, **29**(9), 2370–2391.

Jenkins, A. (2011), Convection-driven melting near the grounding lines of ice shelves and tidewater glaciers, *J. Phys. Oceanogr.*, **41**(12), 2279–2294.

Khan, S. A., A. Aschwanden, A.A. Bjørk, J. Wahr, K.K. Kjeldsen, and K.H. Kjær (2015), Greenland ice sheet mass balance: a review, *Reports on Progress in Physics*, **78** (4), 046801.

Khan, S. A., J. Wahr, M. Bevis, I. Velicogna and E. Kendrick (2010), Spread of ice mass loss into northwest Greenland observed by GRACE and GPS, *Geophysical Research Letters*, **37**, L06501.

Kjær, K. H., et al. (2012), Aerial photographs reveal late–20th-century dynamic ice loss

in northwestern Greenland, *Science*, **337**, 596–573.

Lahet, F. and D. Stramski (2010), MODIS imagery of turbid plumes in San Diego coastal waters during rainstorm events, *Remote Sens. Environ.*, **114** (2), 332–344.

Lydersen, C., P. Assmy, S. Falk-Petersen, J. Kohler, K. M. Kovacs, M. Reigstad, H. Steen, H. Strøm, A. Sundfjord, Ø. Varpe, W. Walczowski, J. M. Weslawski, and M. Zajaczkowski (2014), The importance of tidewater glaciers for marine mammals and seabirds in Svalbard, Norway, *J. Mar. Syst*., **129**, 452–471.

Mankoff, K. D., F. Straneo, C. Cenedese, S. B. Das, C. G. Richards, and H. Singh (2016), Structure and dynamics of a subglacial discharge plume in a Greenlandic fjord, *J. Geophys. Res. Oceans*, **121**(12), 8670–8688.

Matsumura, Y., and H. Hasumi (2008), A non-hydrostatic ocean model with a scalable multigrid Poisson solver, *Ocean Model.*, **24**, 15–28.

Matsumura, Y., and H. Hasumi (2010), Modeling ice shelf water overflow and bottom water formation in the southern Weddell Sea, *Journal of Geophysical Research*, **115**, C10033, doi:10.1029/2009JC005841.

McGrath, D., K. Steffen, I. Overeem, S. H. Mernild, B. Hasholt, and M. van den Broeke, (2010), Sediment plumes as a proxy for local ice-sheet runoff in Kangerlussuaq Fjord, West Greenland, *Journal of Glaciology*, **56** (199), 813–821.

Meire, L., J. Mortensen, P. Meire, T. Juul-Pedersen, M. K. Sejr, S. Rysgaard, R. Nygaard, P. Huybrechts, and F. J. R. Meysman (2017), Marine-terminating glaciers sustain high productivity in Greenland fjords, *Glob. Change Biol.*, **00**, 1–14, doi:org/10.1111/gcb.13801.

Mortensen, J., J. Bendtsen, R. J. Motyka, K. Lennert, M. Truffer, M. Fahnestock, and S. Rysgaard (2013), On the seasonal freshwater stratification in the proximity of fast-

flowing tidewater outlet glaciers in a sub-Arctic sill fjord, *Journal of Geophysical Research-Oceans*, **118**, 1382–1395.

Mortensen J, K. Lennert, J. Bendtsen, and S. Rysgaard (2011), Heat sources for glacial melt in a sub-Arctic fjord (Godthåbsfjord) in contact with the Greenland Ice Sheet., *Journal of Geophysical Research*, **116**, C01013.

Münchow, A., K. Falkner, and H. Melling (2015), Baffin Island and West Greenland Current systems in northern Baffin Bay, *Progress in Oceanography*, **132**, 305–317.

Myers P. G., N. Kulan, and M. H. Ribergaard (2007), Irminger Water variability in the West Greenland Current, *Geophys. Res. Lett.*, **34**, L17601.

Neckel, H., and D. Labs (1984), The solar radiation between 3300 and 12500 Å, *Solar Physics*, **90** (2), 205–258.

Nezlin, N. P., and P. M. DiGiacomo (2005), Satellite ocean color observations of stormwater runoff plumes along the San Pedro Shelf (southern California) during 1997–2003, *Continental Shelf Research*, **25**, 1692–1711.

Nezlin, N.P., P.M. DiGiacomo, D.W. Diehl, B.H. Jones, S.C. Johnson,M.J. Mengel, K.M. Reifel, J.A. Warrick, and M. Wang (2008), Stormwater plume detection by MODIS imagery in the southern California coastal ocean, *Estuarine, Coast. Shelf Sci.*, **80**, 141–152.

Nezlin, N. P., P. M. DiGiacomo, E. D. Stein, and D. Ackerman (2005), Stormwater runoff plumes observed by SeaWiFS radiometer in the Southern California Bight, *Remote Sensing of Environment*, **98**, 494–510.

Ohashi, Y., T. Iida, S. Sugiyama, and S. Aoki (2016), Spatial and temporal variations in high turbidity surface water off the Thule region, northwestern Greenland, *Polar Science*, **10**(3), 270–277.

Otero, M. P., and D. A. Siegel (2004), Spatial and temporal characteristics of sediment plumes and phytoplankton blooms in the Santa Barbara Channel, *Deep-Sea Research II*, **51**, 1129–1149.

Patt, F.S., et al. (2003), Algorithm Updates for the Fourth SeaWiFS Data Reprocessing, NASA Technical Memorandum, 2003–206892, 22, Hooker, S.B., Firestone, E.R., Eds., NASA Goddard Space Flight Center, Greenbelt, Maryland, 74 pp.

Porter, D. F., K. J. Tinto, A. Boghosian, J. R. Cochran, R. E. Bell, S. S. Manizade, and J. G. Sonntag (2014), Bathymetric control of tidewater glacier mass loss in northwest Greenland, *Earth Planet. Sci. Lett.*, **401**, 40–46.

Pritchard, H. D., R. J. Arthern, D. G. Vaughan, and L. A. Edwards (2009), Extensive dynamic thinning on the margins of the Greenland and Antarctic ice sheets, *Nature*, **461**, 971–975.

Retamal, L., S. Bonilla, and W.F., Vincent (2008), Optical gradients and phytoplankton production in the Mackenzie River and the coastal Beaufort Sea, *Polar Biol.*, **31**(3), 363–379.

Ribergaard, M. H. (2007), Oceanographic Investigations off West Greenland, Danish Metrological Institute Centre for Ocean and Ice (DMI), Copenhagen

Saldías, G.S., M. Sobarzo, J. Largier, C. Moffat, and R. Letelier (2012), Seasonal variability of turbid river plumes off central Chile based on high-resolution MODIS imagery, *Remote Sensing of Environment*, **123**, 220–233.

Sasgen, I., M. van den Broeke, J. L. Bamber, E. Rignot, L. S. Sørensen, B. Wouters, Z. Martinec, I. Velicogna, and S. B. Simonsen (2012), Timing and origin of recent regional ice-mass loss in Greenland, *Earth Planet. Sci. Lett.*, **333–334**, 293–303.

Sathyendranath, S. (2000), Remote sensing of ocean color in coastal and other optically

complex waters. IOCCG Report. 3, Dartmouth, Nova Scotia, IOCCG Project Office.

Schrama, E. J. O., B. Wouters, and R. Rietbroek (2014), A mascon approach to assess ice sheet and glacier mass balances and their uncertainties from GRACE data, *J. Geophys. Res. Solid Earth*, **119**, 6048–6066.

Sciascia, R., F. Straneo, C. Cenedese, and P. Heimbach (2013), Seasonal variability of submarine melt rate and circulation in an East Greenland fjord, *J. Geophys. Res. Oceans*, **118**(5), 2492–2506.

Seguinot J., M. Funk, C. Ryser, G. Jouvet, A. Bauder, and S. Sugiyama (2016), Ice dynamics of Bowdoin tidewater glacier, Northwest Greenland, from borehole measurements and numerical modelling, Geophys. Res. Abstract, 18, EGU2016-11604-1.

Shepherd, A., et al (2012), A reconciled estimate of ice-sheet mass balance, *Science*, **338**(6111), 1183–1189.

Smagorinsky, J. (1963), General circulation experiments with the primitive equations: I. The basic experiment, *Mon. Wea. Rev.*, **91**, 99–164.

Smith, L. C., et al. (2017), Direct measurements of meltwater runoff on the Greenland Ice Sheet surface. *Proc. Natl Acad. Sci. USA*, **114**(50), 10622–10631.

Spreen, G., L. Kaleschke, and G. Heygster (2008), Sea ice remote sensing using AMSR-E 89-GHz channels, *Journal of Geophysical Research*, **113**, C02S03.

Stevens, L. A., F. Straneo, S. B. Das, A. J. Plueddemann, A. L. Kukulya, and M. Morlighem (2016), Linking glacially modified waters to catchment-scale subglacial discharge using autonomous underwater vehicle observations, *The Cryosphere*, **10**, 417–432.

Stocker, T.F., D. Qin, G.-K. Plattner, M. Tignor, S.K. Allen, J. Boschung, A. Nauels, Y.

Xia, V. Bex, and P.M. Midgley (2013), Climate Change 2013: The Physical Science Basis. Contribution of Working Group I to the Fifth Assessment Report of the Intergovernmental Panel on Climate Change. Cambridge University Press, Cambridge, United Kingdom and New York, NY, USA.

Straneo, F., and C. Cenedese (2015), The dynamics of Greenland's glacial fjords and their role in climate, *Annu. Rev. Mar. Sci.*, **7**, 89–112.

Straneo, F., D. A. Sutherland, D. Holland, C. Gladish, G. S. Hamilton, H. L. Johnson, E. Rignot, Y. Xu, and M. Koppes (2012), Characteristics of ocean waters reaching Greenland's glaciers, *Ann. Glaciol.*, **53**(60), 202–210.

Straneo, F., and P. Heimbach (2013), North Atlantic warming and the retreat of Greenland's outlet glaciers, *Nature*, **504**(7478), 36–43, doi:10.1038/nature12854.

Straneo, F., R. G. Curry, D. A. Sutherland, G. S. Hamilton, C. Cenedese, K. Våge, and L. A. Stearns (2011), Impact of fjord dynamics and glacial runoff on the circulation near Helheim Glacier, *Nature Geoscience*, **3**, 182–186.

Sugiyama, S., D. Sakakibara, S. Tsutaki, M. Maruyama, and T. Sawagaki (2015), Glacier dynamics near the calving front of Bowdoin Glacier, northwestern Greenland, *J. Glaciol.*, **61**(226), 223–232.

Sutherland D. A., and R. S. Pickart (2008), The East Greenland Coastal Current: structure, variability, and forcing, *Prog. Oceanogr.*, **78**, 58–77.

Thomas, A. C., and R. A. Weatherbee (2006), Satellite-measured temporal variability of the Columbia River plume, *Remote Sensing of Environment*, **100** (2), 167–178.

Valente, A.S., and J.C.B. da Silva (2009), On the observability of the fortnightly cycle of the Tagus estuary turbid plume using MODIS ocean colour images, *Journal of Marine Systems*, **75** (1–2), 131–137.

Walker, N.D., W.J. Wiseman Jr., L.R. Rouse Jr., and A. Babin (2005), Effects of river discharge, wind stress and slope eddies on circulation and the satellite-observed structure of the Mississippi River plume, *Journal of Coastal Research*, **21** (6), 1228–1244.

Wang, M., and W. Shi (2009), Detection of ice and mixed ice-water pixels for MODIS ocean color data processing, *IEEE Transactions on Geoscience and Remote Sensin*g, **47** (8), 2510–2518.

Xu, Y., E. Rignot, D. Menemenlis, and M. Koppes (2012), Numerical experiments on subaqueous melting of Greenland tidewater glaciers in response to ocean warming and enhanced subglacial discharge, *Ann. Glaciol.*, **53**, 229–234.

Xu, Y., E. Rignot, I. Fenty, and D. Menemenlis (2013), Subaqueous melting of Store Glacier, West Greenland from three-dimensional, high resolution numerical modeling and ocean observations, *Geophys. Res. Lett.*, **40**, 4648–4653.

Zwally, H. J., M. B. Giovinetto, M. A. Beckley, and J. L. Saba (2012), Antarctic and Greenland Drainage Systems, GSFC Cryospheric Sciences Laboratory, at http://icesat4.gsfc.nasa.gov/cryo_data/ant_grn_drainage_systems.php.

## Acknowledgements

I would like to express my gratitude to Dr. Shigeru Aoki, chair of the doctoral degree supervisory committee, and who supervised this study for the last 3 years since the beginning of the doctor program. He provided many opportunities, and supported this research with frequent discussions. Prof. Shin Sugiyama, member of the doctoral degree supervisory committee, supervised me through the master program, supported this study and provided the opportunity for in-situ observation in Greenland. Prof. Naoto Ebuchi, Prof. Keiichiro Ohshima, and Prof. Hiroyasu Hasumi, members of the doctoral degree supervisory committee, made insightful comments on the thesis.

I would also like to express my deep appreciation to Dr. Yoshimasa Matsumura. He supported the numerical model experiments and made the valuable comments on this study. I acknowledge Dr. Yasushi Fukamachi, Dr. Naoya Kanna, Dr. Daiki Sakakibara, and Ms. Izumi Asaji, who helped me in the Greenland to collect the observational data in the thesis. I also thank all the members of the field campaigns in northwestern Greenland in 2014 and 2016. I wish to thank all the members of the Atmosphere-Ocean Interaction Research Group and, Ocean and Sea Ice Dynamics Group in the Institute of Low Temperature Science, Hokkaido University for supporting my study and daily life.

This research was supported by MEXT (Japanese Ministry of Education, Culture, Sports, Science and Technology) through the Green Network of Excellence (GRENE) Arctic Climate Change Research Project and the Arctic Challenge for Sustainability (ArCS) Project.

Finally, I would like to express my appreciation to my family and friends for enthusiastic support.